Master Thesis in Geographical Information Science nr 183

Flood Risk Assessment for the Kävlinge River for Present and Future Climate Scenarios using HEC-RAS Rain-on-Grid

Josephine Roosli

2024

Department of
Physical Geography and Ecosystem Science
Centre for Geographical Information Systems
Lund University
Sölvegatan 12
S-223 62 Lund

Sweden

Josephine Roosli (2024). Risk Assessment for the Kävlinge River for Present and Future Climate Scenarios using HEC-RAS Rain-on-Grid

Master degree thesis, 30 credits in Master in Geographical Information Science

Department of Physical Geography and Ecosystem Science, Lund University

Supervisor: Zheng Duan, Lund University

Committee Members: David Tenenbaum, Harry Lankreijer

Abstract

Extreme climate events, such as significant flooding, pose a natural disaster risk. Due to climate change effects, the southern region of Sweden is anticipated to receive more significant rainstorms that could cause flooding increasingly with the quantity of emissions. This study examines the present-day and future climate's flooding risk in a small area in this region, within the Kävlinge Watershed. The future climate scenario uses the Intergovernmental Panel on Climate Change's (IPCC) Representative Concentration Pathway (RCP) 8.5 scenario in the year 2100.

The flooding risk is determined using the intersection of flooding hazard and vulnerability. Present-day and future hazard levels are based on flooding depth as calculated by a calibrated and validated hydraulic-hydrodynamic model called HEC-RAS rain-on-grid. The performance metrics used in the calibration and validation process were the Nash-Sutcliffe Efficiency (NSE), Coefficient of Determination (R^2), and Percent Bias (PBIAS). Vulnerability is found using an analytic hierarchy process weighting and combination of land cover, transportation infrastructure, schools, age and fragility of the population, municipal buildings, and cultural sites.

The area is shown to have mostly relatively low vulnerability, with a few moderately vulnerable areas close to towns. The HEC-RAS rain-on-grid model's NSE, R^2, and PBIAS were within satisfactory ranges and reflected good performance of the model, which signifies an accurate representation of the flooding simulations. The hazard of the flooding in this area is moderate along the river, and very low or low levels of hazard in spots throughout the area. The intersection of the vulnerability and the hazard show moderate and major risks along the river and particularly close to the towns. Other areas, mostly agricultural, show a low or moderate level of risk. The difference between the present-day and climate scenario flooding is small but important, given the close proximity of the towns to the climate scenario's increased flooding and therefore increased risk.

The limitations, mostly due to time-constraints, are discussed, along with potential additional considerations or improvements to the risk assessment. However, the current results may be useful for planning for present and future flooding in this region.

Sammanfattning

Extrema klimathändelser, såsom betydande översvämningar, utgör en risk för naturkatastrofer. På grund av klimatförändringarnas effekter förväntas södra Sverige få fler betydande regnväder som kan orsaka översvämningar i allt högre grad med mängden utsläpp. I denna studie undersöks dagens och framtidens översvämningsrisk i ett litet område i denna region, inom Kävlinges avrinningsområde. I det framtida klimatscenariot används den Intergovernmental Panel on Climate Change (IPCC) RCP (Representative Concentration Pathway) 8,5-scenario för år 2100.

Översvämningsrisken bestäms med hjälp av skärningspunkten mellan översvämningsrisk och sårbarhet. Nuvarande och framtida risknivåer baseras på översvämningsdjup som beräknas med en kalibrerad och validerad hydraulisk-hydrodynamisk modell som kallas HEC-RAS rain-on-grid. De prestationsmått som användes i kalibrerings- och valideringsprocessen var Nash-Sutcliffe Efficiency (NSE), Coefficient of Determination (R2) och Percent Bias (PBIAS). Sårbarheten fastställs med hjälp av en analytisk hierarkiprocess som viktar och kombinerar marktäcke, transportinfrastruktur, skolor, befolkningens ålder och skörhet, kommunala byggnader och kulturmiljöer.

Området visar sig mestadels ha relativt låg sårbarhet, med några måttligt sårbara områden nära städerna. HEC-RAS rain-on-grid-modellens NSE, R2 och PBIAS låg inom tillfredsställande intervall och återspeglade goda prestanda för modellen, vilket innebär en korrekt representation av översvämningssimuleringarna. Översvämningsrisken i det här området är måttlig längs floden och mycket låg eller låg risknivå på vissa ställen i hela området. Skärningspunkten mellan sårbarhet och risk visar på måttliga och stora risker längs floden och särskilt nära städerna. Andra områden, främst jordbruksområden, uppvisar en låg eller måttlig risknivå. Skillnaden mellan dagens översvämningar och översvämningarna i klimatscenariot är liten men viktig, med tanke på städernas närhet till klimatscenariots ökade översvämningar och därmed ökade risker.

Begränsningarna, som främst beror på tidsbegränsningar, diskuteras tillsammans med potentiella ytterligare överväganden eller förbättringar av riskbedömningen. De aktuella resultaten kan dock vara användbara för att planera för nuvarande och framtida översvämningar i denna region.

Table of Contents

List of Tables

List of Figures

1. Introduction

Extreme climate events, such as significant rainstorms that cause flooding, have large effects on society. These effects include economic costs, physical damage to both human-made structures and the ecological environment, and also psychological impacts on humans. Unfortunately, these extreme climate events have also been increasing in frequency and intensity, and will continue to do so (Easterling et al., 2000a; Easterling et al., 2000b; Intergovernmental Panel on Climate Change [IPCC], n.d.; Peterson et al., 2013; Roudier et al., 2015). This is also made worse by more urban development and agricultural practices (Pinter et al., 2005). Because of the worsening extreme climate events, modelling these events, such as predicting events, mapping of potentially affected areas in certain scenarios, is becoming more important to city and government planning processes than before, and can be useful in warning people of possible future calamity (Ryu et al., 2017; Tran et al., 2008).

To model scenarios of a changing climate, many studies use the Intergovernmental Panel on Climate Change's (IPCC) Representative Concentration Pathway (RCP) scenarios. There are four RCPs modelled by the IPCC, which each represents potential scenarios varying in the quantity of future greenhouse gas concentrations in the atmosphere. These are the RCP2.6, RCP4.5, RCP6, and RCP8.5 scenarios. For example, RCP2.6 models emissions decreasing progressively from 2020 until hitting zero emissions by 2100. The RCP8.5 is the worst-case scenario, where emissions continue to increase (Pörtner et al., 2019). Because it is the worst-case scenario, it is a standard in climate change predictive modeling studies (Alfieri et al., 2015a; Bronselaer et al., 2018; Guerreiro et al., 2018; Prein et al., 2017; Riahi et al., 2011).

According to the RCP8.5 model, Sweden and specifically southern Sweden, will be one of these areas with worsening climates (Alfieri et al., 2015b; Rojas et al., 2013). Rain is expected to worsen, and the Scania region already receives the second-highest quantity of extreme rain in Sweden due to conditions that carry moisture over Europe and the Baltic Sea (Gustafsson et al., 2010; Nyberg et al., 2019). Because of the expected increased quantities of rain, resulting flooding will likewise worsen (Buffin-Bélanger et al., 2015; Chang et al., 2010; Shrestha and Lohpaisankrit, 2017). Given the climate research indications for this area, having accurate expectations about the hazards, vulnerabilities, and disaster risk in this area will be beneficial to understanding how to best allocate funds towards building and housing efforts, as well as inform zoning changes.

In scientific literature, there are a number of tools that have been developed to standardize the analysis of hazards, vulnerabilities, and disaster risk. The most commonly used for flood studies is the comprehensive risk assessment created by Maskrey (1989), which incorporates the multiple facets of what makes a natural disaster "disastrous" (the intersection and scale of hazards and vulnerabilities). This is possible with the use of GIS software. However, to model the hazard portion, a hydrology and hydraulic specific software is needed. There are also numerous options for the mapping of hazards past, present, and future, but one of the newest and simplest is the HEC-RAS rain-on-grid model (Costabile et al., 2021; Godara et al., 2024; Zeiger and Hubbart, 2021).

HEC-RAS is a modelling software released by the US Army Corps of Engineers Hydrologic Engineering Center (HEC). It is a River Analysis System (RAS) that can be used for 1D, 2D, and combined 1D/2D models. 1D is typically used for dominant flow paths, cases with limited data, and high-gravity rivers (steeper terrain), and 2D is used for cases with potential multiple flow paths, wide and flat floodplains, estuaries, and braided river systems. A versatile program, it can run steady (a continuous input of river flow or rain into the system) and unsteady flows (varying input quantity of river flow or rain during the model's run-time) (Horritt and Bates, 2002). The relatively new HEC-RAS rain-on-grid model is a 2D model that performs unsteady flow analysis over a terrain and works by using precipitation as an input (Costabile et al., 2021; Zeiger and Hubbart, 2021). It models the river flow over a watershed or a sub-set of a watershed and provides a timeline of results for the entire time period modeled. These results can be used to show the hazard area through water depth or river velocity and can be useful as the hazard portion of a risk assessment (Ennouini et al., 2024).

A risk assessment study of Southern Sweden's Kävlinge River, particularly where there is a higher population and more infrastructure close to the river, can be interesting for decision-makers of this region. Because of the changing climate in Southern Sweden (Gustafsson et al., 2010; Nyberg et al., 2019), a localized comparison of current flooding with potential future flooding considering climate change should be considered when making infrastructure or zoning decisions, as these are decisions made with long-term effects (Gain et al., 2015; Masood and Takeuchi, 2006). While some studies have already modeled the area with climate change into account, no studies have performed a comprehensive risk analysis that considers vulnerabilities (Hu, 2022; Myndigheten för samhällsskydd och beredskap [MSB], 2020; Wicher, 2016). Performing a quantitative risk analysis study with visual results can be used to help inform leadership and communities in this area.

1.1 Objectives

The objective of this study is to establish a new model in the Kävlinge watershed using the HEC-RAS rain-on-grid software and use it to perform present and future risk assessments in the most populated section of the Kävlinge River, which is the last 23.6 kilometers. Specifically, the objectives are to:

- Evaluate how well the HEC-RAS rain-on-grid effectively models the Kävlinge River.
- Determine which areas in the last 23.6 kilometers of the Kävlinge River are flooded in the wettest year of flow records presently.

- Determine which areas in the last 23.6 kilometers of the Kävlinge River are flooded during a wet year in the year 2100 using the climate model RCP8.5.
- Establish vulnerabilities throughout the Kävlinge watershed by using a created flood vulnerability map and identify the most vulnerable locations in the last 23.6 kilometers of the river.
- Combine the flood hazard and flood vulnerability map into a flood risk map, and analyze and compare the most at-risk locations in present-day conditions and future climate conditions.

1.2 Background

1.2.1 Risk = Hazard x Vulnerability

Being able to anticipate and plan for natural disasters is economically, socially, and environmentally beneficial locally and on a large scale (Maskrey 1989, Wisner et al., 1994). Risk assessments can contribute to the anticipation of the size of the natural disaster and timing, and in the planning process by identifying areas' and infrastructures' risk. The need for natural disaster risk assessments is only increasing due to worsening climate change, and the usefulness of these assessments for local governments is becoming more important (Danumah et al., 2016; Orencio and Fujii, 2013).

One of the most common ways to perform a comprehensive overview of risk is by using an equation initially created by Maskrey (1989), which is:

$$R = H \times V \tag{1}$$

where R is risk, H is hazard, and V is vulnerability. This equation stems from Maskrey's observation that a natural event, the "hazard" (such as flooding or hurricane) only becomes a natural disaster when there is a "vulnerability" (such as infrastructure unable to withstand the strength of the hazard or people who have difficulties evacuating) that are in the path of the event.

To expand on these definitions, the United Nations International Strategy for Disaster Reduction (2009) defines hazard in their "Terminology on disaster risk reduction" as "a dangerous phenomenon, substance, human activity or condition that may cause loss of life, injury or other health impacts, property damage, loss of livelihoods and services, social and economic disruption, or environmental damage". Previous studies of risk assessment have included hazards such as droughts, landslides, and coastal flooding (Clark et al., 1998; Shahid and Behrawan, 2008; van Westen et al., 2006).

Likewise, the United Nations International Strategy for Disaster Reduction (2009) defines vulnerability as "The characteristics and circumstances of a community, system or asset that make it susceptible to the damaging effects of a hazard". It is a crucial part of the risk equation, because without vulnerability there is no disaster

(Wisner et al., 1994). Understanding the type, severity, and locations of vulnerability aides in the planning process, thereby decreasing the amount of vulnerability (Smit and Wandel, 2006).

There is some discussion on other aspects of risk that should be included into the equation, such as exposure, mitigation capacity, and resilience (Cutter et al., 2008; Turner et al., 2003). However, most models accept that a simplified hazard, vulnerability, and risk equation is sufficient (Apel et al., 2008; Blaikie et al., 1994; Cardona et al., 2012; Dang et al., 2010; Hoque et al., 2017; Mishra and Singa, 2020; Tingsanchali and Karim, 2005; Turner et al., 2003; Weichselgartner, 2001).

Identifying the amount of risk over an area as a function of magnitude of hazard and the quantity of vulnerability can mitigate natural disasters when acted upon and planned for in advance (Hoque et al., 2017). This is increasingly important not only due to increasing intensity of hazards due to climate change, but also due to societal aspects such as increased (and aging) population and continuous infrastructure development (Masood and Takeuchi, 2006). Using spatial analysis is particularly helpful in the analysis of risk, and a variety of new techniques, models, and technology are continuously improving the accuracy of calculated hazards and helpfulness of risk assessments (de Brito and Evers, 2016; Jena and Pradhan, 2020; Zou et al., 2012). In addition, risk assessments that use an analytic hierarchy process (a method to weight multiple factors) in the process of calculating vulnerability also improves the risk assessment (Chakraborty and Mukhopadhyay, 2019; Dang et al., 2010; Danumah et al., 2016; Rincón et al., 2018; Wu et al., 2015). Risk assessments can also be useful in mapping multiple disasters within one area, including rainfall flooding and coastal tidal impacts (Aksha et al., 2020; Mani Murali et al., 2013).

Numerous studies of risk assessment using this general method have been conducted, as seen in Table 1, which focuses on flood risk assessments. The table provides a collection of studies that are highly cited with a variety of methods. The overall method to determine risk is the same, which multiplies hazard and vulnerability, except for Gain et al. (2015) which calculates the total economic cost of the hazard and vulnerability, and the papers by Suriya and Mudgal (2012) and Vojtek and Vojteková (2016), which perform qualitative overlay analysis. However, the methods of the multiplication of hazard and vulnerability vary and may be calculated on different regional extents, may be weighted or unweighted, and are quantified differently. Similarly, the methods of quantifying hazard vary as well. Typically, a modelling program is used to find the hazard factor (Table 1 focuses mostly on HEC-RAS), but in areas of less data availability where complex modelling or analyses cannot be performed, basic risk assessments (using analytic hierarchy process for hazard) can still be very useful (Aksha et al., 2020; Ghosh and Kar., 2018; Mishra and Singa, 2020; Rincón et al., 2018; Wu et al., 2022). The papers in Table 1 use factors such as flood depth, flood duration, water velocity, flood probability, drainage factors (such as soil and slope), and some papers include a mix of these factors. The factor used the most often is flood depth. Vulnerability also has differing methodologies, where factors are sometimes weighted or unweighted, the categorization and quantification differ, and there is a much larger variation of factors included for the studies. They include various factors within geographical, socioeconomic, population demographics, and land use subjects.

Table 1: Literature Review of Risk Assessments using Flood Hazards

Reference	**Risk (R)**	**Hazard (H)**	**Vulnerability (V)**	**Additional Notes**
Dang et al., 2010	R = H x V Calculations performed on grid cells. Vulnerability weighted twice as much as hazard, due to unquantifiable factors that exaggerate the quantifiable vulnerability factors (i.e. populations' ignorance to flood danger)	Analytical hierarchy process (AHP) weighted calculation using flood depth, duration, velocity.	11 factors in three categories, economic, social, and environmental. Calculated using a weighted sum using AHP.	Exposure noted as one of three variables in risk but is not considered separately. Concentration of the overlap of hazard and vulnerability (and therefore exposure).
Danumah et al., 2016	R = H x V R defined categorically into 5 levels of risk.	AHP weighted sum based on drainage density, type of soil, slope, and isohyet. Analysis performed in ArcGIS.	AHP weighted sum based on building structure, population density, and drainage system	
Darabi et al., 2019	R = H x V Then classified into 5 levels of risk.	Scale of flood probability (0-1). Modelled to test two machine learning algorithms.	Uses urban density, building age/quality, population density, and socio-economic conditions. Vulnerability between 0-1. Performed using Fuzzy Analytical Network Process.	

Edamo et al., 2023	FRI (flood risk index) = FHI x FVI	FHI = % Area x FHS FHS = W x R (W = weight corresponding to flood severity (1 for low, 5 extremely high; R = rating corresponding to probability of each flood severity, also 1-5); Severity determined by HEC-RAS calculated flood depth.	FVI = (Agricultural area + Built area + Total household + Maximum daily rainfall) / 4 Based on socioeconomic indices.	
Gain et al., 2015	Risk viewed as cost (separated as direct tangible, indirect tangible, direct intangible, and indirect tangible costs) Hazard, vulnerability, and exposure examined as variables in complex cost analyses.	Based on HEC-RAS modelled flood variables (depth, flow).	Aggregate vulnerability found using equal weighting system, all factors weighted equally; score between 0 and 1 (low to high); includes literacy, income, early warning system functionality, building age/type/materials, etc. Assigned one of 5 normalized scores (0, .25, .5, .75, 1)	Risk included a third dimension, exposure (includes number of people/cars, industry, agricultural land, land use, etc.)
Masood and Takeuchi, 2011	R = H x V Range from 0 to 50. Resulting map classified values into low, medium, and high risk areas.	Using HEC-RAS, normalized values 1-5 for flood depth.	Weighted percentage of area covered with living area and agricultural land (Ranged vulnerability from 0-10).	
Nkeki et al., 2022	R = H x V All factors weighted together in risk equation (vulnerability was not calculated separately as a first step)	HEC-RAS calculated flood depth. Included with vulnerability factors in the pairwise hierarchical comparison matrix.	Vulnerability (and exposure) factors considered and weights determined AHP, including hazard. Overall vulnerability not determined, and each factor was input into the risk equation.	

Suriya and Mudgal, 2012	Results examined both maps concurrently to examine overall risk. No overarching mathematical calculation of total risk.	Based on HEC-RAS modelled flood depth with HEC-HMS as initial step.	Considered as "probability of occurrence" by overlaying maps of rainfall, size/slope of watershed, gradient of river, drainage density, soil types, land use, infrastructure. Factors ranked and weighted depending on flood influence. Vulnerability of each cell = sum of all weighted factors.	
Tingsanchali and Karim, 2005	R = H x V	Hazard index (equal weighting of depth and duration). Modelled by MIKE-11. Scaled to values between 0-100.	Expressed between 0-1, based on population density.	
Vojtek and Vojteková, 2016	Overlay of hazard, vulnerability, and flood intensity. Results examined all maps concurrently. No overarching mathematical calculation of total risk.	Classified based on three flood hazard categories (high, medium, low), and can be summarized as recommendations for urban planning. Analysis performed in HEC-RAS.	Three categories of risk: given area's functional land use (high acceptable risk = natural spaces; medium acceptable risk = recreation spaces and residential greenery; minimum acceptable risk = residential, commercial, agriculture, industry, other infrastructure)	Risk included a third dimension, flood intensity. This was a function of HEC-RAS modelled water depth and velocity.

Zhang et al., 2022	R = H x V Four levels of risk grouped by scores (safe (1-3), moderate (4-9), major (10-16), severe (20,25) grouped by scores (1-25). Performed for each municipality, and each H and V are weighted with specific weights assigned for each municipality.	Based on coverage of flood, percentage of inundated area, and flow velocity for each administrative area. Normalized scores of 1-5. Analysis performed in HEC-RAS.	Sum of socio-economic exposure and impact indicators (land use, livelihood, economy, infrastructure, gender, education, population density, population age/dependency) with varying weights. Then normalized scores of 1-5. Weighting method not specified.	

These papers varied by performing the calculation on grid cells, regions, or grid cells later summarized into regions.

1.2.2 HEC-RAS Rain-on-Grid

To create a hazard map of flooding, there are numerous potential models to use independently or in conjunction, such as UniCal (Costabile et al., 2021), FESWMS (Cook and Merwade, 2009), LISFLOOD-FP (Horritt and Bates, 2002), TELEMAC-2D (Horritt and Bates, 2002), MIKE 11 (MSB, 2020), and MODFLOW (Rodriguez et al., 2008) and HEC-RAS (David and Schmalz 2021, Zeiger and Hubbart 2021). To create the map of flooding itself, a hydraulic model is used to show water moving over the terrain. Conjointly using a hydrologic model can model precipitation and other conditions in the modelled area that can improve the accuracy of the hydraulic model.

The United States Army Hydrologic Engineering Center has created numerous open software programs related to this, for example, the hydrologic model (HEC-HMS) and hydraulic model (HEC-RAS). These two models can be used in multiple hazard mapping cases, such as dam ruptures, climate predictions, complex braided floodplains, and paleoflood modeling (Benito et al., 2004; Sheffer et al., 2008; Tayefi et al., 2007; Yochum et al., 2008).

There is a relatively new hydraulic-hydrodynamic function within HEC-RAS, which uses a rain-on-grid hydrodynamic model as a basis to perform 2D hydraulic functions and results (Costabile, 2020). This means that precipitation can be an input into a 2D hydraulic model. The rain-on-grid model was initially added to the HEC-RAS software in 2016. Since then, updated functionalities throughout the various HEC-RAS versions have improved its abilities and use cases drastically, particularly in recent years (Zeiger and Hubbart, 2021). This was thanks to the addition of the infiltration parameterization in 2021 and was likely the most significant software update and when rain-on-grid could truly begin to be used as a simplified hydraulic-hydrodynamic model (Costabile et al., 2021). It is now used in scientific research and for private commercial use regularly and has been shown to be effective in comparisons to other hydrological models (Costabile et al., 2021; Ginting et al., 2023; Malik and Pal, 2021).

The HEC-RAS two-dimensional rain-on-grid model uses a mesh grid, which organizes a large area into a mesh grid, creating many cells of which individual calculations can be performed. Both hydrological and hydraulic calculations are performed on this cellular level. The hydrological portion, which concentrates on the water cycle, is calculated with the new quantity of rain arriving in each mesh cell by precipitation or neighboring cell and the amount of water leaving the mesh cell by either permeation or run-off. The hydraulic portion, which concentrates on the mechanical behavior of the water over a surface, calculates the flow’s direction, height, and velocity per mesh cell, and directs run-off to the receiving mesh cell. This allows for snapshots of the quantity of water and the velocity to be displayed according to the time interval selected. An example of a snapshot and the visible mesh grid is in Figure 1.

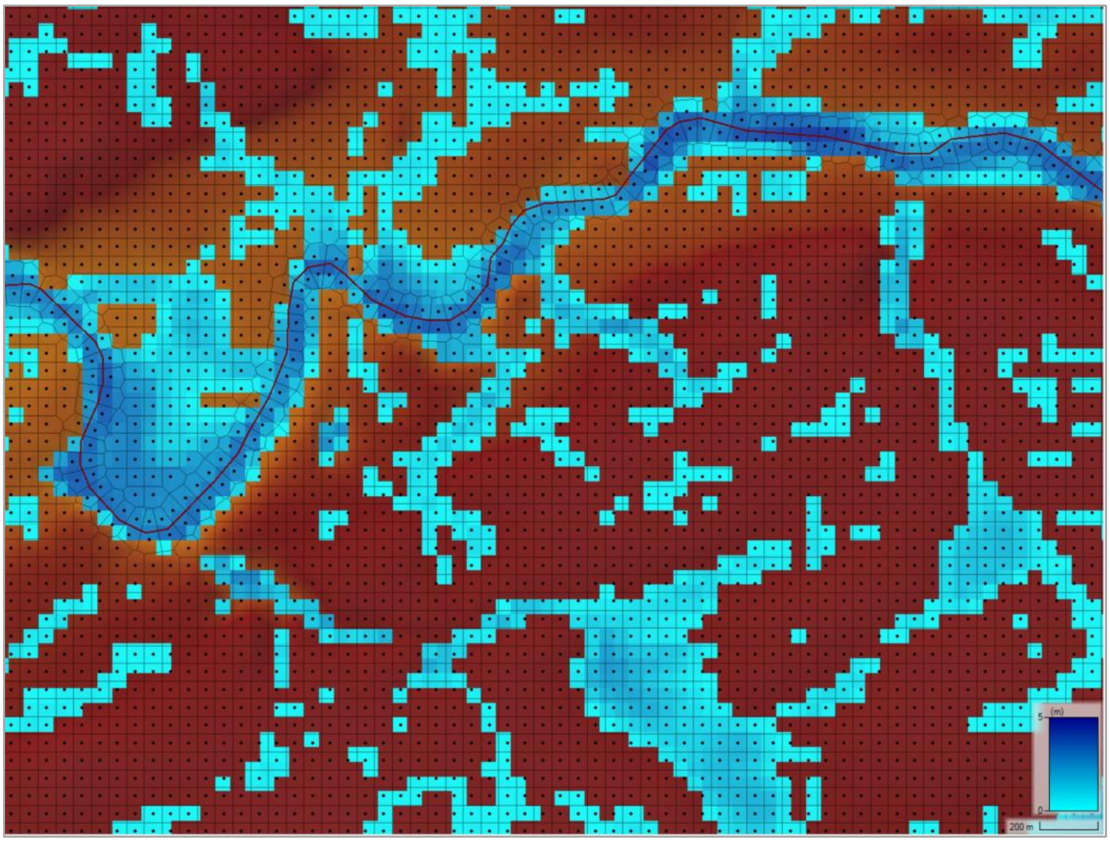

Figure 1: An example of the HEC-RAS rain-on-grid model calculating and displaying water depth of the Kävlinge Watershed, with the mesh grid overlay. Note how the mesh grid changes to follow the river geometry.

HEC-RAS 6.4.1 has two options for calculating two-dimensional unsteady flow with the two-dimensional Saint Venant equations either in full, with the shallow water equations (SWE), or partially, with the diffusion wave equations (DWE) (Hydrologic Engineering Center, n.d.-b). DWE is the default for the system as it works well in most situations. SWE must be tested against DWE and is better adapted in more dynamic cases such as highly accelerating floods, sharp bends in the river, or tidal interferences, but is also extremely time intensive (Brunner, 2022). The full two-dimensional Saint Venant equations are as follows:

$$\frac{\partial \mathrm{C}}{\partial t} + \frac{\partial p}{\partial x} + \frac{\partial q}{\partial y} = 0 \tag{2}$$

$$\frac{\partial p}{\partial t} + \frac{\partial}{\partial x}\left(\frac{p^2}{h}\right) + \frac{\partial}{\partial y}\left(\frac{pq}{h}\right) = \frac{n^2 pg\sqrt{p^2+q^2}}{h^2} - gh\frac{\partial \mathrm{C}}{\partial x} + pf + \frac{\partial}{\rho \partial x}(h\tau_{xx}) + \frac{\partial}{\rho \partial y}(h\tau_{xy}) \tag{3}$$

$$\frac{\partial q}{\partial t} + \frac{\partial}{\partial y}\left(\frac{q^2}{h}\right) + \frac{\partial}{\partial x}\left(\frac{pq}{h}\right) = \frac{n^2 qg\sqrt{p^2+q^2}}{h^2} - gh\frac{\partial \mathrm{C}}{\partial y} + qf + \frac{\partial}{\rho \partial y}(h\tau_{yy}) + \frac{\partial}{\rho \partial x}(h\tau_{xy}) \tag{4}$$

where g represents gravity acceleration (ms^{-2}), h is the depth of water in meters, n is the Manning's roughness coefficient, p and q are water flows in the x and y direction (m^2s^{-1}), C is the elevation in meters, and ρ is the density of the water in kilograms per meter cubed. τ refers to the effective shear stress of the component in question. This study does not apply to the more dynamic need cases for SWE, and therefore uses DWE, which means that equations 3 and 4 are not considered.

Unlike many other hydrological or hydraulic models, HEC-RAS' rain-on-grid is special due to its simplified nature, which makes use of the minimal inputs and amount of parameterization required. The basic inputs are all raster (a data form using rectangular cells) and include a digital elevation model, an infiltration layer, and Manning's roughness coefficient. The digital elevation model is a raster layer with an elevation value for each cell and significantly impacts the movement of the water from grid cell to grid cell. The infiltration layer determines how much water is permeating into the soil and has several methodological options, including Curve Numbers, which is a value that represents the combination of the permeability of both soil and land cover to determine how much water permeates into the ground.

The Manning's roughness coefficient is a value per cell describing the speed of water over an area, related to the amount of friction the water experiences while moving through the grid. The unit for the Manning's roughness coefficient is time over cube root distance. In addition, geometric data is created including the mesh grid where each mesh cell undergoes the calculation of water flow, and an additional boundary condition (where water exits). The last input is the boundary condition of water being input into the system (specifically, precipitation data).

The parameterization at the most basic requires only a calibration of the infiltration layer and Manning's roughness coefficient. Because of the lack of other parameters and the importance of Manning's roughness and infiltration in this model, they are tested within the range of +/- 50% (Ginting et al., 2023; Khadka et al., 2018). Occasionally, due to the limited parameterization possible, there are also cases where it is necessary to test beyond 50% (Zeiger and Hubbart, 2021). The amount of infiltration is impacted by changing the curve number primarily, and also the abstraction ratio and minimum infiltration rate.

It should be noted that both Manning's roughness coefficient and infiltration are vulnerable to temporal variability. This means that the values change depending on things like weather conditions, seasonal changes, or impacts from development (Maneta et al., 2007; Mazarei et al., 2021; Xu et al., 2019). This means that the most ideal starting values for Manning's roughness coefficient and infiltration will likely differ for different starting time periods. For the most accurate results, the model will calibrate and validate Manning's roughness coefficient and infiltration for each temporal scenario.

The 2D HEC-RAS rain-on-grid can be further optimized using additional factors. For example, there are variable time step options, which changes the rate of calculation depending on the conditions of the system and is a function of flow velocity and flow length. There are also Initial Conditions, which can be used to shorten the dry start-up period of the model. The start-up period is the period of time prior to any rainfall or other flow input, where the model is dry until there is an input of water. As such, adding Initial Conditions is necessary to add a starting quantity of water flow in the system to the beginning of the model's run, so there is water flowing prior to any rain event and as such providing a more realistic start-up to the time period.

Though HEC-RAS's 2D rain-on-grid's methods are quite simple in regard to inputs, it has comparable results at the watershed scale to other more complex models (Costabile et al., 2021; Godara et al., 2024; Zeiger and Hubbart, 2021). It has been found to be reliable in numerous use cases in the following studies. In one study that examined extreme rainfall events reliability as modeled by HEC-RAS, rain-on-grid was found to have very low error (Ansori et al., 2023). The rain-on-grid model was also tested in complicated scenarios such as areas with terraced walls for ancient agricultural practices or in wildfire burnt areas and was found to function well using synthetic storms in these cases (Alamanos et al., 2024; Stavi et al., 2024).

Advantages have been found when modeling flooding in urban spaces, including intricate drainage channels, canals, and irrigation (Ontowirjo et al., 2023; Savitri et al., 2021).

One disadvantage of HEC-RAS rain-on-grid compared to other modeling systems is the length of computation time. While access to resources such as super computers might mitigate this issue, for the majority of studies' resources, this is not a possibility, and therefore it is necessary to consider the input resolutions' effect on computation time. In fact, it is such an issue, that many studies mention computation time and how they have managed to find an appropriate balance between computation time and detail. Some studies have found that some inputs had to be generalized to reduce calculation time dependent on the watershed size (David and Schmalz, 2021; Zeiger and Hubbart, 2021). However, these compromises are not unreasonable. In the case of a large watershed, while a larger computation mesh grid is likely necessary, it does not impede accuracy significantly (David and Schmalz, 2021). In addition, a higher resolution digital elevation models (DEM), which is a raster layer that has one value of elevation for each cell, are not necessarily more accurate for HEC-RAS rain-on-grid, potentially because the rain-on grid's grid cells simplifies the DEM's information if the DEM is of a higher resolution than the established HEC-RAS grid cell (Ginting et al., 2024). In the case where large watersheds cannot make the compromise of larger cell sizes, it has been found that running separate sub-watershed models was effective (Hariri et al., 2022).

As established in Table 1, modeling hydraulics of rivers can be useful for risk assessments. However, many of the studies in Table 1 are performed with the commonly used HEC-RAS 1D or 2D, but without using the rain-on-grid function. Due to the new nature of HEC-RAS rain-on-grid, a literature review of the performance of HEC-RAS rain-on-grid would be useful and can be found in Table 2. As can be seen, HEC-RAS rain-on-grid, despite being new, is an effective method of hydraulic modelling.

The advantages of the HEC-RAS rain-on-grid model are significant because it offers a special advantage in its simplicity, concurrent hydraulic and hydrologic modelling and because there are no financial charges. This means that it can be implemented easily and cheaply in developing countries and areas with lower access to data (Costabile et al., 2021; Kalra et al., 2023; Malik and Pal, 2020). As a result, it has been and will continue to be a useful tool for risk assessments (Ennouini et al., 2024; Nkeki et al., 2022; Nkeki et al., 2023).

Table 2: Literature Review of Performance Metrics of Studies Using HEC-RAS Rain-on-grid

Reference	Use	Study Area	Performance
Alamanos et al., 2024	Simulation of historical post-fire flashflood, integrated modeling with atmospheric model for precipitation input.	Kineta Watershed (40 km^2), eastern Greece	Satisfactory Performance Critical Success Index = 0.65
Ansori et al., 2023	Case study of extreme rainfall events (100 mm in first hour)	Wiroko Sub-Watershed (183.9 km^2), Java, Indonesia	Good performance of Peak discharge difference = 0.8%, Significant discrepancy of time to peak discrepancy = 1.93 hours
Costabile et al., 2021	HEC-RAS rain-on-grid benchmark study	Small-scale real-world tests (urban Glasgow, Scotland), and synthetic tests	Good performance in simulations in real-world tests Partially unsatisfactory performance in synthetic tests
David and Schmalz, 2021	HEC-RAS rain-on-grid benchmark study	Messbach Watershed (2.13 km^2), central Germany	Good performance Nash-Sutcliffe Efficiency ≥ 0.8, Difference in Maximum Water-Surface Elevation = .03 - .05 cm, Volume Deficit = 5%, Volume Balance = 95%
Ennouini et al., 2024	Flood risk assessment at catchment level	Terdoppio Novarese Sub-Watershed (75.8 km^2), northern Italy	Good performance Difference in peak discharge = 3% Unsatisfactory performance, total volumes Tested against synthetic design hydrographs
Ginting et al., 2023	Comparison of HEC-RAS 2D rain-on-grid and several synthetic unit hydrograph methods	Katulampa Watershed (151.3 km^2), Indonesia	Good performance Root mean square error = 1.98, Pearson product moment correlation = 0.93
Godara et al., 2024	Comparison of TELEMAN-2D and HEC-RAS 2D rain-on-grid modeling techniques	Sleddalen Watershed (10.5 km^2), western Norway	Good performance Nash-Sutcliffe Efficiency = 0.7 - 0.9, Coefficient of determination = 0.93 - 0.95

Hariri et al., 2022	Testing of watershed decomposition method using HEC-RAS 2D rain-on-grid	Saar Watershed (1,747 km^2), northeastern France	Good performance Volume deficit < 12%, Nash-Sutcliffe Efficiency close to 1, ratio of the root mean square error to the standard deviation < 0.5
Malik and Pal, 2021	Case studies of historical monsoon flooding	Dwarkeswar River Watershed (4,357 km^2), eastern India	Good performance Pearson correlation = 0.93, root mean square error = 0.69, Nash-Sutcliffe Efficiency = 0.71
Nkeki et al., 2023	Flood risk mapping including analytical hierarchy process in junction with HEC-RAS rain-on-grid	Ona Watershed, western Nigeria	Good performance Results consistent with historical data = 90%
Zeigler and Hubbart, 2021	Evaluating integrated modeling approach with SWAT (Soil and Water Assessment Tool, to model rainfall rate to be used for rain-on-grid input)	Hinkson Creek Watershed (232 km^2), central United States	Good performance Nash-Sutcliffe Efficiency = 0.33-0.92, Coefficient of determination = 0.86-0.97, percent bias = 10.4-33.8%

1.2.3 Calibration and Validation Procedure

Ensuring an accurate and usable model requires a calibration and validation procedure (Bates et al., 2004; Moriasi et al., 2015). Without a calibration and validation procedure, it is not possible to know that the model created is accurately representing reality. This is particularly important when considering the possible decisions being made thanks to the results (Bennett et al., 2013; Van Calster et al., 2019).

Calibration is the initial process of changing the models' parameters as needed to make the model more closely reflect what was observed in reality. Generally, this is done by using a sensitivity analysis, which is when one parameter is adjusted at a time to find the effects of that parameter on the model, and then continuing this process until the right mix of parameter adjustments and their values are found. There are several methods during the sensitivity analysis, for example experimenting by removing certain parameters all together, performing an organized sensitivity analysis that performs every possible combination (very time-consuming), or a trial-and-error sensitivity analysis that adjusts parameters and keeps what changes are working and fixes what changes are not.

To be sure if this calibration is working, it is necessary to compare the result of the model with observed data. For previous HEC-RAS rain-on-grid studies, this has been done with several different types of observed data, including historical reports, hydrographs, flooding extent aerial imagery, and gauge data (such as height, discharge, velocity of water) (Ennouini et al., 2024; Hariri et al., 2022; Malik and Pal, 2020; Nkeki et al., 2022; Zeiger and Hubbart, 2021). When the results of the model closely reflect the observed data, the calibration can be considered finished.

However, during the calibration phase, comparing one result of the model to a piece of observed data is not enough to have confidence in the model. When possible, a model should be compared temporally and spatially, which is called a split-sample procedure (Bates et al., 2004; Vázquez et al., 2002). Considering the temporal aspect is important due to potential differences in climate; for example, calibrating a hydrological model in wet periods may not produce accurate results during a dry period in the same area (Seiller et al., 2012; Zeiger and Hubbart, 2021). As such, including multiple time periods and different conditions will likely result in a better calibrated model.

The spatial aspect adds another layer of confidence. For example, if only one site is used (or if all sites in a catchment are close together), the model is being evaluated based on one area of the catchment, and may be poorly calibrated elsewhere (Refsgaard, 1997; Seiller et al., 2012; Vázquez et al., 2002). Several HEC-RAS rain-on-grid include this method to increase the confidence level of the model (Alamanos et al., 2024; David and Schmalz, 2021; Zeiger and Hubbart, 2021). This is because many HEC-RAS rain-on-grid studies examine event-based flooding and are therefore limited in the temporal aspect. To counteract this problem, a suggested technique is to split up the event into stages, and to perform a split-time calibration using the one event (Moriasi et al., 2007).

Besides split-time and split-site, it is also possible to use different types of data. For example, some HEC-RAS rain-on-grid studies have used both gauge data and aerial imagery of flooding area to calibrate the model (David and Schmalz, 2021; Malik and Pal, 2020). The more variation in the data used in the calibration process, the more robust and accurate the model will likely be.

There is a disadvantage to this calibration process, even with split-sampling (albeit that reduces this negative effect). This is overfitting, which means that the model can explain the reality extremely well given the samples used to calibrate, but when the model is put into other scenarios it performs poorly (Radosavljevic and Anderson, 2013; Val Calster et al., 2019). To avoid this, the second stage of validation proceeds after the calibration phase.

The validation phase uses a new set of data, also preferably split-site and split-time, to evaluate the model. It is imperative for final result of the calibration and validation process that there are separate groups of data for both steps, as this prevents errors and overfitting (Bennett et al., 2013; Radosavljevic and Anderson, 2013). Likewise, as with calibration, the more varied the types of data used in the validation process, the more confident the model.

1.2.4 Saaty's Analytic Hierarchy Process (AHP)

An AHP is an effective type of multi-criteria decision analysis (MCDA), weighting multiple factors together using subjective reasoning and is used in over 40% of MCDA papers (de Brito and Evers, 2016). A commonly used method by Saaty (1980), has been said to provide a "crispness" to the subjective reasoning, including a method to consider human faults and biases into the final weights (Zou et al., 2012). It has been used often in risk assessments, occasionally for the hazard portion and typically for the vulnerability portion and was used in nearly all vulnerability weighting cases in Table 1. This is because the vulnerability is complex, unquantifiable, and dynamic, and as such using a MCDA is an effective way to evaluate it, particularly when using a spatial aspect to aide in the calculation, visualization, and analysis of vulnerability (Adger, 2006; Apel et al., 2004; Ouma and Tateishi, 2014; Weichselgartner, 2001).

Saaty's AHP uses a standard pairwise comparison to determine the weighting. Essentially, a person compares multiple variables by separately rating differences between two at a time and later calculating their subjective weighting, thus making it more comprehensive (Saaty, 1980). While very effective, breaking down the multiple comparisons to a more digestible two variables at a time has a limit around 7-10 total variables (Teknomo, 2006).

To perform an AHP, first the overall goal and hierarchical structure is determined (if there are subfactors of factors), and the ensuite step is performing a pairwise comparison matrix. This compares two of potentially many variables at a time. Because each relationship is examined twice, the reverse of the relationship is also the reverse in the matrix. For example, a relationship that is given a value of 4 will be ¼ in the reverse relationship. Depending on the number of variables, n, the structure of the pairwise comparison matrix A is as below:

$$A = \begin{bmatrix} \frac{w_1}{w_1} & \frac{w_1}{w_2} & \cdots & \frac{w_1}{w_n} \\ \frac{w_2}{w_1} & \frac{w_2}{w_2} & \cdots & \frac{w_2}{w_n} \\ \vdots & \vdots & \vdots & \vdots \\ \frac{w_n}{w_1} & \frac{w_n}{w_2} & \cdots & \frac{w_n}{w_n} \end{bmatrix} \tag{5}$$

where $w > 0$ and $\sum_{i=1}^{n} w_i = 1$.

To perform each comparison, Saaty's (1980) scale is used, of values between 1 and 9. A value of 1 is equivalent to equal importance. Where each variable is compared against itself, this value is sure to be 1. A value of 9 is representative of "extreme importance", and the scale of numbers between 1 and 9 are used correspondingly.

The next step is to calculate the weights using the matrix. This is determined by the Priority Vector, or the Normalized Eigen Vector (W). This is calculated by first finding the sum of all columns in the matrix. This sum is then used to calculate the normalized matrix, by dividing each relationship value by the sum of the relationships in its respective columns. To obtain the Normalized Eigen Vector, the normalized matrix's variable rows are averaged. The total of all Normalized Eigen Vectors should be 1, as these are the weights to be used in the analysis. This process is summarized by the following equation:

$$W = \frac{1}{n} \begin{bmatrix} \frac{w_1}{w_1} \div \sum \frac{w_i}{w_1} & \frac{w_1}{w_2} \div \sum \frac{w_i}{w_2} & \cdots & \frac{w_1}{w_n} \div \sum \frac{w_i}{w_n} \\ \frac{w_2}{w_1} \div \sum \frac{w_i}{w_1} & \frac{w_2}{w_2} \div \sum \frac{w_i}{w_2} & \cdots & \frac{w_2}{w_n} \div \sum \frac{w_i}{w_n} \\ \vdots & \vdots & \vdots & \vdots \\ \frac{w_n}{w_1} \div \sum \frac{w_i}{w_1} & \frac{w_n}{w_2} \div \sum \frac{w_i}{w_2} & \cdots & \frac{w_n}{w_n} \div \sum \frac{w_i}{w_n} \end{bmatrix} \quad (6)$$

The steps of determining the Normalized Eigen Vectors and the normalized matrix are necessary steps. While it could be possible to determine weighing coefficients simply based on the original matrix and relationship scores, using the Normalized Eigen Vectors as weights accounts for the inconsistency of human decisions, judgements, and feelings (Saaty, 2003).

Likewise, due to the nature of the fact that these comparisons are being made only two relationships at a time, it is necessary to check for consistencies throughout the relationships of all variables as a whole. An example of this is if Variable A is more important than Variable B, and Variable B is more important than Variable C, then through the transitive property, Variable A should be more important than Variable C as well. The magnitude of the difference of importance between the variables comes into play here too – if A is enormously more important than B, B enormously more important than C, it would not be logical that A is only slightly more important than C.

To check the consistency, the Consistency Ratio is determined and should be less than 10%, where the amount of inconsistency present is acceptable. This is determined in several steps, the first of which is to calculate the Principal Eigen Value. This is calculated by calculating the sum of each respective column sum in the original matrix multiplied by the respective Normalized Eigen Vector.

The next steps include the Consistency Index (CI) and the Consistency Ratio (CR), which are as follows:

$$CI = \frac{\lambda_{max} - n}{n - 1} \quad (7)$$

$$CR = \frac{\mathrm{CI}}{\mathrm{RI}} \tag{8}$$

where λ_{max} is the Principal Eigen Value and RI is the Random Index Value. The RI value is based on the number of variables in question (n, always more than 2 because AHP consists of only 3 or more variables) and can be determined by referencing Table 3. The resulting value of the Consistency Ratio should be less than 0.10, which is less than 10% and is considered within the acceptable range of inconsistency.

Table 3: Random Index Value Table

n	1	2	3	4	5	6	7	8	9	10
RI	0.00	0.00	0.58	0.90	1.12	1.24	1.32	1.41	1.45	1.49

1.3 Study Area

The study focuses a section of the Kävlinge River, in Skåne county in Southwest Sweden. The river begins at Lake Vombsjön and runs for about 50 kilometers through flatlands before supplying the Øresund Strait, which separates Sweden and Denmark and connects the Baltic Sea and North Sea. The surrounding flatlands consist of mostly agriculture, with some urban or rural infrastructure typically close to the Kävlinge River, and occasional forest patches.

The section that is being concentrated on begins at the confluence with the last major tributary, the Bråån River, and continues for the last 23.6 kilometers prior to ending in the Øresund Strait. It was decided to concentrate on this portion of the river for several reasons. Most importantly is that because the focus of this research is the risk of disaster, and therefore examines the intersection of humans' vulnerability and the natural hazard. The great majority of human populations along the Kävlinge River live in this 23.6-kilometer section, where it passes through or close to several medium sized towns: Kävlinge, Furulund, Löddeköpinge, and Bjärred (upstream to downstream). These populations close to the river are disconcerting because a study of past flow levels of the Kävlinge River shows that the river frequently floods and affects the fields and urban spaces close to the river (Baden and Davidsson, 2016). Another major reason is because of the lack of additional major tributaries, which simplifies the HEC-RAS modelling without compromising on the focus of the research. This practice of selecting a portion of river with the highest level of interest, as opposed to modeling the river in its entirety, is common and yields results (Cook and Merwade, 2009; Horritt and Bates, 2002; Knebl et al., 2005; Rahmati et al., 2016; Suriya and Mudgal, 2012).

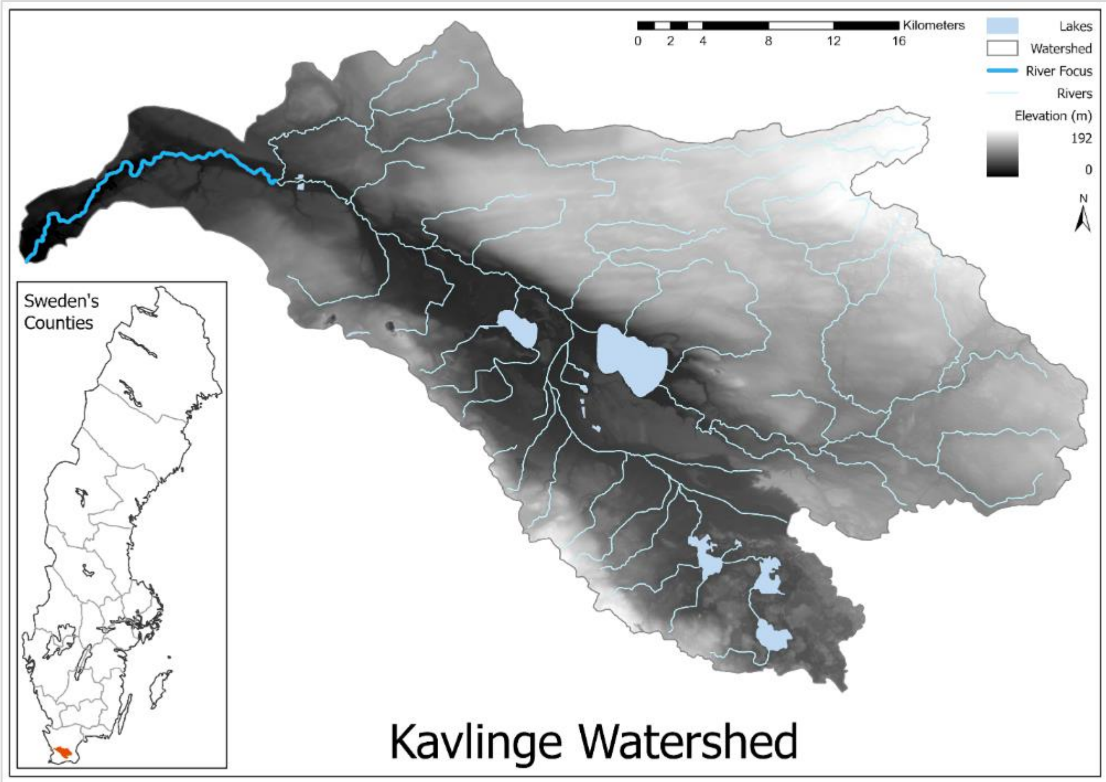

Figure 2: The Kävlinge Watershed
The map presents the elevation and extent of the watershed, along with the rivers and lakes. The main river focus of 23.6 kilometers (after to the Bråån confluence) is highlighted. For context, the watershed is shown in red in relation to Sweden and its counties.

The watershed is a relatively narrow area, as seen in Figure 2. The area of the watershed is 1203 kilometers squared, with a perimeter of 229 kilometers. The highest elevation in the watershed is 191 meters above sea level, and the lowest elevation is where the river meets the Øresund Strait, at sea level. On average, the elevation is 77 meters above sea level. The baseline of flow at the Högsmölla gauge, which is located in the center of the 23.6 kilometers this study examines, typically ranges from 2 to 5 meters cubed per second in dry months, which is typically July and August.

A review of the literature of this region shows that several studies modelling flooding have already been conducted using the Kävlinge River. These studies include university research papers and governmental inquiries. Two studies have examined the amount of discharge in climate scenarios used HEC-HMS, which is a hydrology-exclusive software program and does not perform hydraulics or mapping of the results (Hu, 2022; Wicher, 2016). Flooding has been modeled using HEC-HMS conjoined with HEC-RAS to perform the hydraulics and making to study flood scenarios using present predictions (Khadka et al., 2018). Only one study has been performed using only HEC-RAS, to test dam altering scenarios' effects on ecology (Tollgren and Walldén, 2017). Another university research paper used a different modelling software, MIKE HYDRO, which examined river straightening scenarios (Olguín, 2020). Similarly, using a different software program, a governmental inquiry examined flooding scenarios using present predictions and climate using a different modelling system, MIKE 11 (MSB, 2020). Regardless of the modeling system used, all results have shown that the calibration and validation process lead to a successful flooding prediction model in this area. As expected, the climate models show greater flooding with climate change in relation to the increase of precipitation and worsening storm events.

No previous study has used the model in a comprehensive analysis of natural disaster risk. This would include finding not only the results for flooding event scenarios to create a flood hazard map, but also creating a flood vulnerability map to combine into a natural disaster risk map. While there are other studies that examine separate vulnerabilities, they have not visualized, or combined multiple vulnerabilities into the same map, or united vulnerabilities with flood hazard (Baden and Davidsson, 2016; Lunds Kommun and VA SYD, 2017). In addition, no study has used the relatively new HEC-RAS rain-on-grid model to model this area.

2. Data and Methods

The overarching goal of this study is to examine two scenarios of natural disaster on the Kävlinge, which are present-day heavy rain period flooding and future heavy rain period flooding. To do this, vulnerability and hazard maps are made, analyzed, and multiplied together. The process and the components are shown summarized in Figure 3.

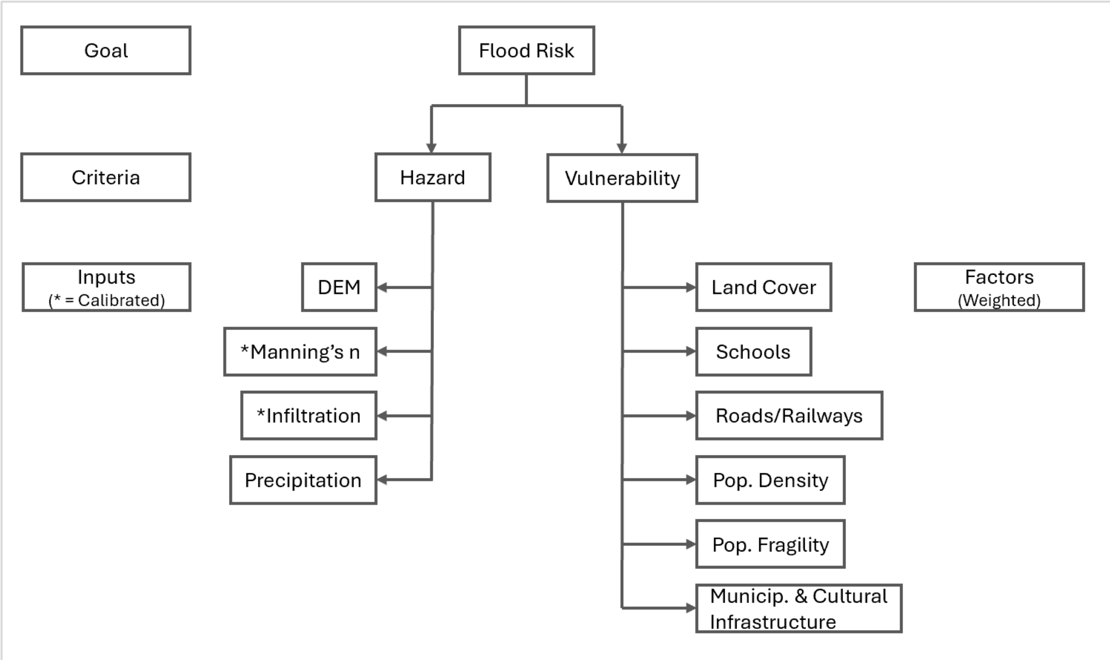

Figure 3: Risk Assessment Components

However, prior to being able to create the hazard and vulnerability maps, the initial data must be preprocessed in order to become the inputs into the model for hazard and an AHP for vulnerability.

2.1 Data

Nearly all initial data was found in publicly facing sources offered and organized by multiple organizations through the Swedish government. Only some geographic conditions required for the hazard maps was created in HEC-RAS by hand. The data downloaded or created can be found in Figure 4. A crucial first step for all geographic data was to ensure that the data is in the Transverse Mercator projection and in the SWEREF99 TM projected coordinate system (Lantmateriet, n.d.-b). This is standard for most Swedish public geographic data since 2003 when it replaced the RT90 2.5 gon V (Klokan Technologies GmbH, 2021). It can be referenced to with the EPSG Geodetic Parameter Dataset value 3006.

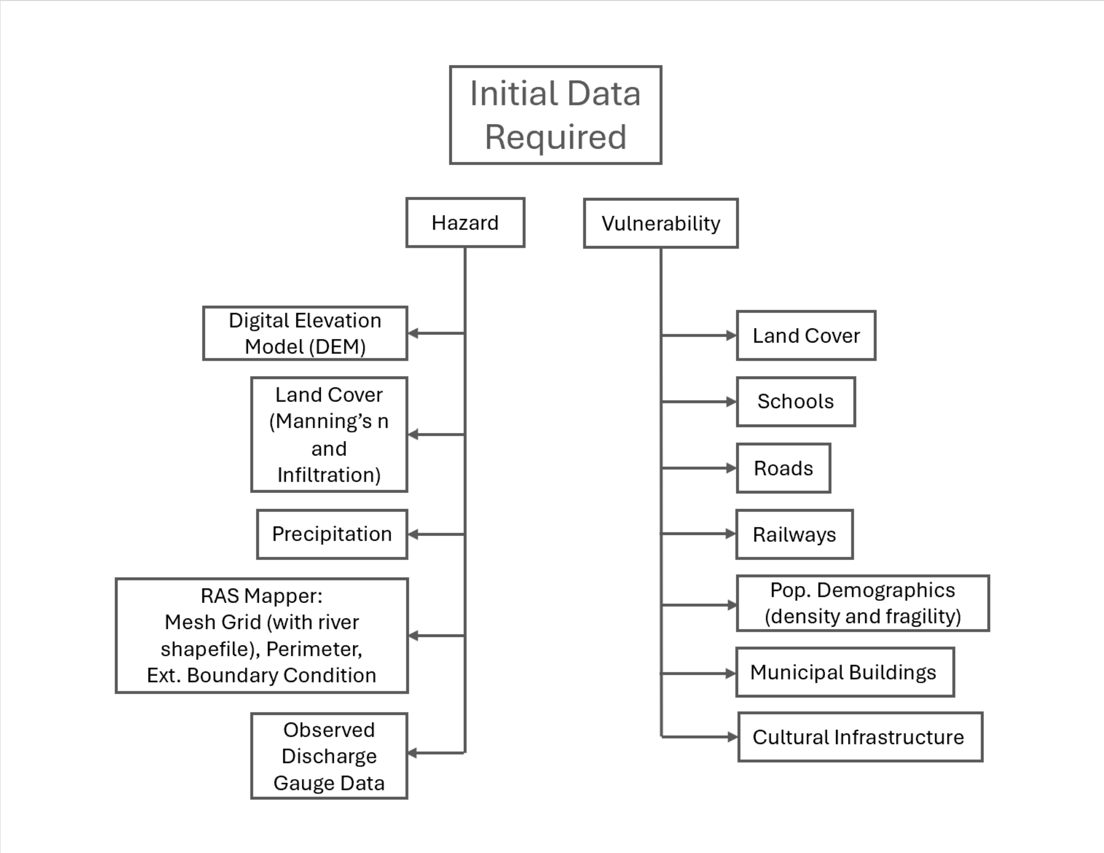

Figure 4: Data required for the methods that result in the risk assessment factors of hazard and vulnerability

2.1.1 Hazard Data Preprocessing

There are several data that are required to run the hazard model in HEC-RAS, including the DEM, Manning's roughness coefficient, an infiltration layer, perimeter, mesh grid, and an external boundary condition, as well as additional data to confirm the model is working, which is the observed discharge.

The digital elevation model is one of the most important inputs to a hydraulic model because elevation is an important determiner of where water will travel and as such the resolution should be as high as possible (Casas et al., 2006). The digital elevation model (DEM) used in this study is a 1-meter resolution model, which means that the layer is in meter-by-meter cells with one elevation value for each cell (Lantmateriet, n.d.-a). This data was downloaded in several tiles, merged together, and clipped to the watershed in order to increase processing speeds. The DEM of the watershed is shown in Figure 2. While other hydrological models require additional preprocessing steps (such as fill sinks), it is not necessary for HEC-RAS rain-on-grid (Hydrologic Engineering Center, n.d.-b). Another step used in some studies is digitizing specific bridges, buildings, or culverts; however, in large scale uses (including watersheds as in this case), there is no need because the DEM itself is sufficiently containing this information (Zeiger and Hubbart, 2021).

To create the Manning’s roughness coefficient layer and the infiltration layer, land cover data is needed. This is downloaded was for the entire country and contained dozens of different land classifications (Naturvårdsverkets, n.d.).

This land cover layer was then exported into a new layer and received Manning’s roughness coefficients according to the HEC-RAS 2D User’s Manual (Hydrologic Engineering Center, n.d.-b). Because the user’s manual typically uses a range of values, the study by Asante et al. (2008) informed initial Manning’s values. These values are one of the parameters that are later changed in the calibration process. A map separating areas by Manning’s n roughness coefficients can be found in Figure 5, where the values reflect the calibrated values. The original values and the conversion can be found in Appendix 1. While Manning’s values are nuanced because of seasonal and year-to-year differences, for simplicity, the same values are used throughout the watershed, which is standard in procedure (Ansori et al., 2024; Ennouini et al., 2024, Ginting et al., 2023; Kalra et al., 2023).

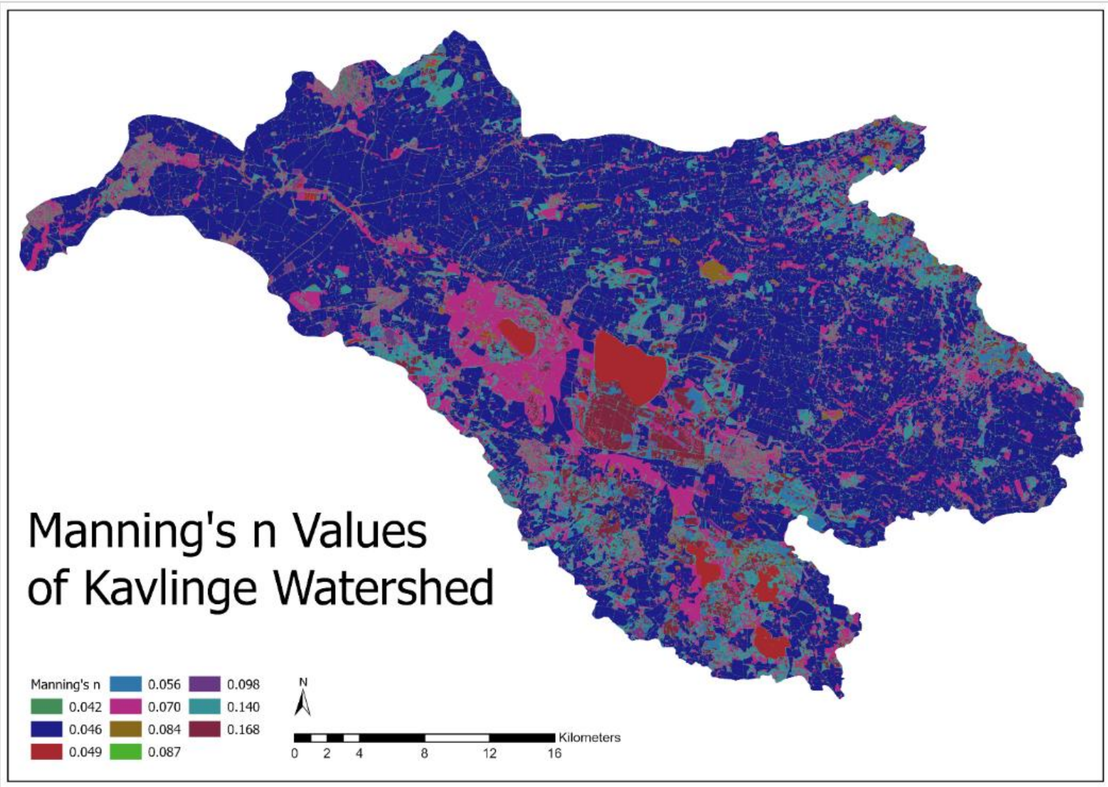

Figure 5: Manning’s n values of the Kävlinge Watershed after calibration

The land cover layer was also used to create the curve number grid which serves as the infiltration layer to be used in HEC-RAS. The infiltration layer estimates how much rainfall permeates into the ground, and can be represented using several methods, in this case, the commonly used curve number is used, which combines the land cover with a soil layer from Sveriges Geologiska Undersökning. The steps taken are outlined in Merwade’s (n.d.) tutorial and establishes a baseline of infiltration for the watershed, which is then adjusted during the running of the model to consider precedent precipitation and soil moisture (Hydrologic Engineering Center n.d.-b). This is also one of the parameters later calibrated, and the map of the calibrated curve number areas can be found in Figure 6. While the initial infiltration values are nuanced due to previous weather conditions and soil moisture, the same Curve Numbers are used, which is standard in procedure (Ansori et al., 2024; Ennouini et al., 2024, Ginting et al., 2023; Kalra et al., 2023).

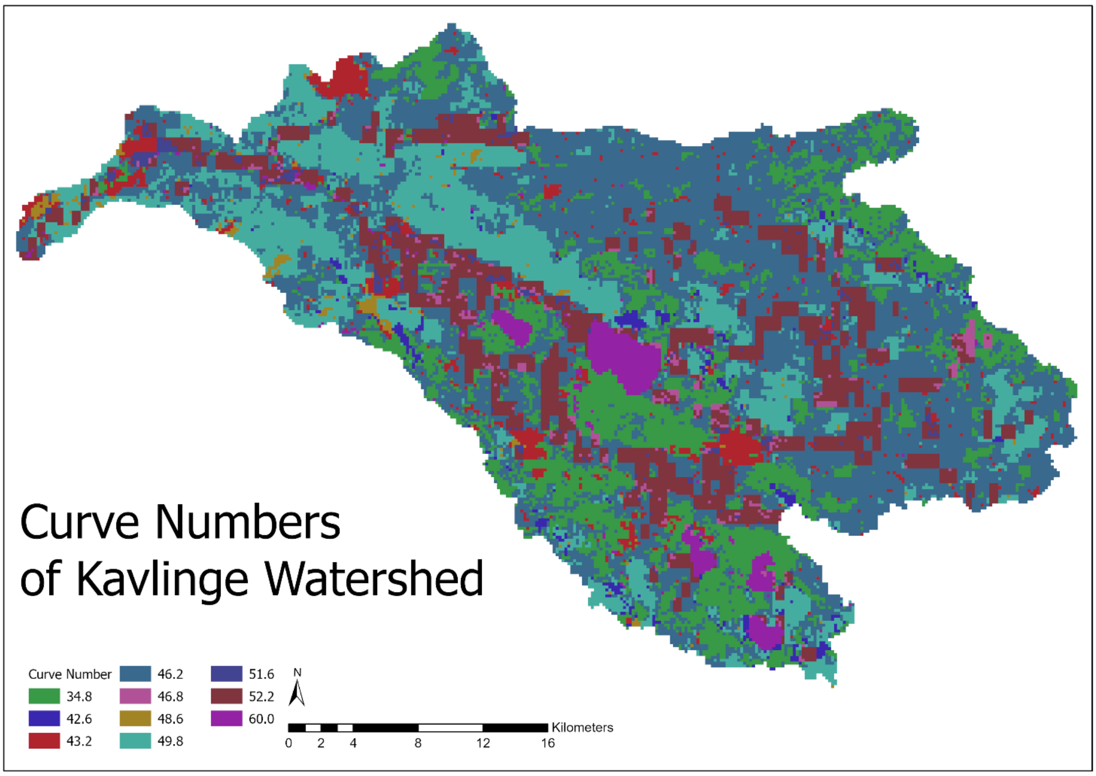

Figure 6: Curve numbers of the Kävlinge Watershed after calibration

Also necessary is the perimeter, which was created by tracing the watershed. The perimeter then is used to establish the creation of the mesh grid. This creates cells covering the watershed; each cell is a set of individual calculations regarding the movement and quantity of water. Just prior to the 2D Flow Area mesh creation, a shapefile of rivers using the Export Tool from the Humanitarian OpenStreetMap Team (n.d.) was uploaded into the breaklines layer in HEC-RAS's RAS mapper, which adjusted the cells close to the river to follow the geometry of the river and improve the model's accuracy.

The grid size chosen for this model was 40 meters by 40 meters. While this size is on the larger end of the spectrum as compared to other rain-on-grid studies, there are several conditions which allow it. These conditions include the fact that the area is generally flat and has uncomplex terrain (the velocity and direction of water are not changing quickly), overall watershed is relatively large compared to other studies (computation time is significant), and that the shape and size are adjusted along the breaklines (accuracy is improved) (Hydrologic Engineering Center, n.d.-b). In addition, the general suggested relationship between resolution of the mesh grid and watershed would result in 24 hours of computing time, and this study had an average of 48 hours of computing time per model, though this depends on computer capacity (David and Schmalz, 2021). Given the size of the study and computation times, the cell size is a necessary compromise. Also added in the RAS mapper window is a boundary condition line at the mouth of the river. With a condition type of “external” this signifies that the water along these cells can leave the perimeter.

2.1.2 Preparation of gauge data

Once all initial input data was input in the HEC-RAS RAS mapper, the next step was entering the unsteady flow data. The first boundary condition entered was for the boundary condition line, in which the normal depth condition was selected. This was calculated by finding the friction slope, which can be simplified by dividing the height lost over the distance of the river. In this case, the friction slope was .00068 (16 meters of elevation lost over 23.6 kilometers of river). This calculates the rate of which the water in the system leaves through the boundary line at the mouth of the river. The second boundary condition was to enter how much water is entering the watershed, which came from the preparation of rainfall gauge data.

Precipitation Data

The precipitation data needed as input into the rain-on-grid model was found on the Swedish Meteorological and Hydrological Institute website (Swedish Meteorological and Hydrological Institute [SMHI], 2024b). Hourly data is used to provide the model more detail and improve the accuracy of the results. Two aspects of the data required further pre-processing prior to being ready to insert into HEC-RAS; multiple gauging stations needed to be taken into account and occasional, random observations of data are missing.

While there were no hourly precipitation observation stations directly within the watershed that are currently active, there are three stations nearby: Hörby, Malmo, and Skillinge. Because of the relatively close proximity of the three weather stations and relatively flat terrain, a Thiessen interpolation of the watershed’s precipitation could be utilized here. This interpolation approach is well-known and accepted to provide a reasonable interpolation of multiple observations of precipitation for an overall watershed (Anandhi et al., 2008; Wenli, 2022). This functions by calculating a weighted average rain (WAR) according to the percentage of area that is closest to each station, as seen in the equation below.

$$\mathrm{WAR} = \frac{\sum A_t \times R_h}{A_w} \tag{9}$$

where the A_t is the area of the Thiessen polygon for a given rain observation station, R_h is the hourly rain for that observation station, and A_w is the total watershed area.

This is performed for all hourly observations to find the interpolated rain of the total watershed.

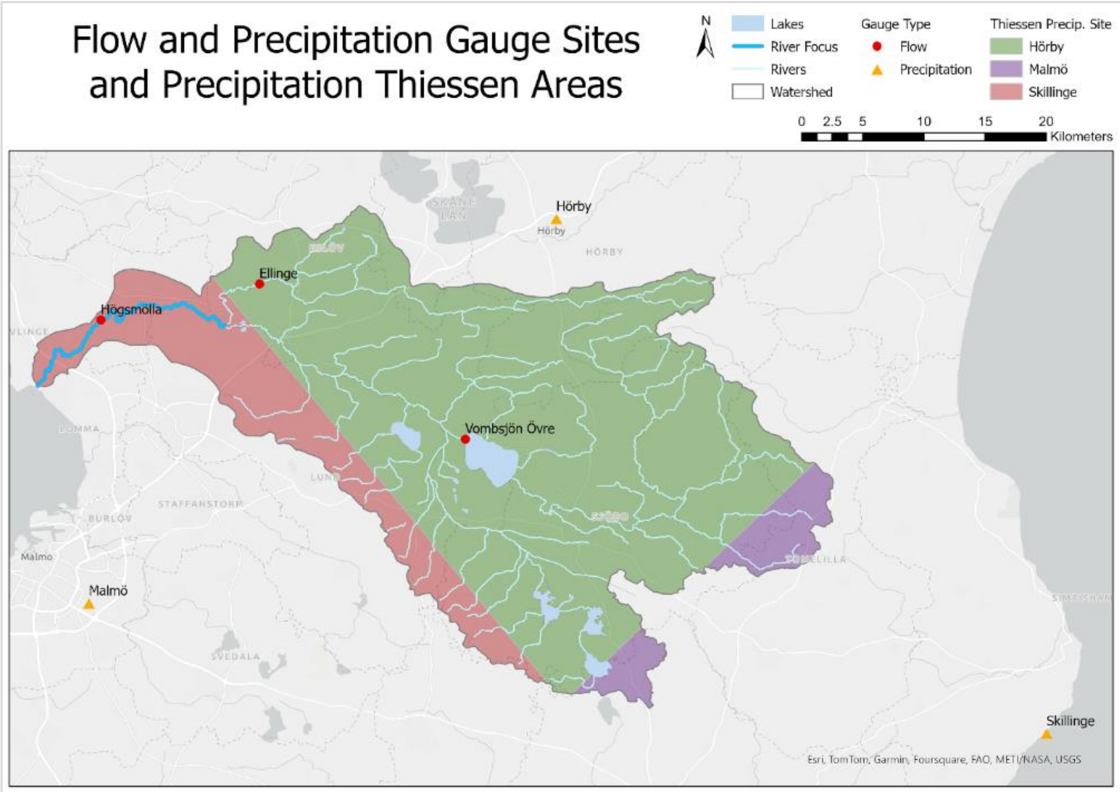

Figure 7: Flow and Precipitation Gauge Sites and Precipitation Thiessen Areas

In order to do this interpolation, Environmental Systems Research Institute, Inc. (ESRI)'s ArcGIS Pro version 3.1.3 developed in Redlands, California (USA), was used. The weather stations were plotted as points, and the function *Thiessen polygons* was performed on the watershed polygon. This splits the watershed area into areas based on which station is closest, which can be seen in Figure 7. Then using Posit's R Studio version 2023.12.1 Build 402 developed in Boston, Massachusetts (USA), the weighted average is calculated using the sizes of the respective polygons' area. In the same script, missing values were also addressed. While missing data were rare, they were accounted for by averaging the other two station's rainfall values, and if two stations' values were missing for the same observation time, then the remainder was used for the other two stations. Extremely rarely, all three stations were missing a value. In this case, the weighted sum was calculated using the average amount of precipitation in the hour before and the hour after, though this value was typically not during a rain event and was zero.

Discharge Data

The discharge data are also needed to compare if the model is functioning well because the calibration and validation is performed by comparing the simulated and observed flow of discharge. Daily instantaneous discharge was found on the Swedish Meteorological and Hydrological Institute website (SMHI, 2024b).

The more gauge stations that are included in the calibration and validation process, the more certain the results are. There are three observation gauges in the Kävlinge watershed available on the SMHI open data website (SMHI, 2024b). They are Högsmölla, Ellinge, and Vombsjön Övre. All three gauges provide daily instantaneous observed values in meters cubed per second. However, Vombsjön Övre calculates observed flow after the dam that creates Lake Vombsjön, and the water released there is a regulated flow. As such, it is not useful to use in a calibration or validation of a hydrological model, and as such it is not used. However, Högsmölla and Ellinge both monitor the natural flow. Högsmölla is the gauge in the city of Kävlinge River and therefore central to the exact length of the Kävlinge which is the study area. Ellinge is used as a secondary site to confirm the calibration is acceptable in another part of the watershed, specifically for the Bråån River which is a tributary to the Kävlinge just before the focus of the study area begins. With the exception of 2003 which had some missing hourly observations, all years of flow data have complete observations.

Selection of Time Period

Due to very long processing times, only about 6 months could be run at a time in the model. To select the time period to be used in the simulation, two visuals were referenced. First was a chart that found the average daily discharge by month between 1976 to 2023, as displayed in Figure 8. All possible years were included to anticipate an overall climate pattern of this region, and this indicated that the 6 months from November to April had the highest discharge and are therefore the wettest.

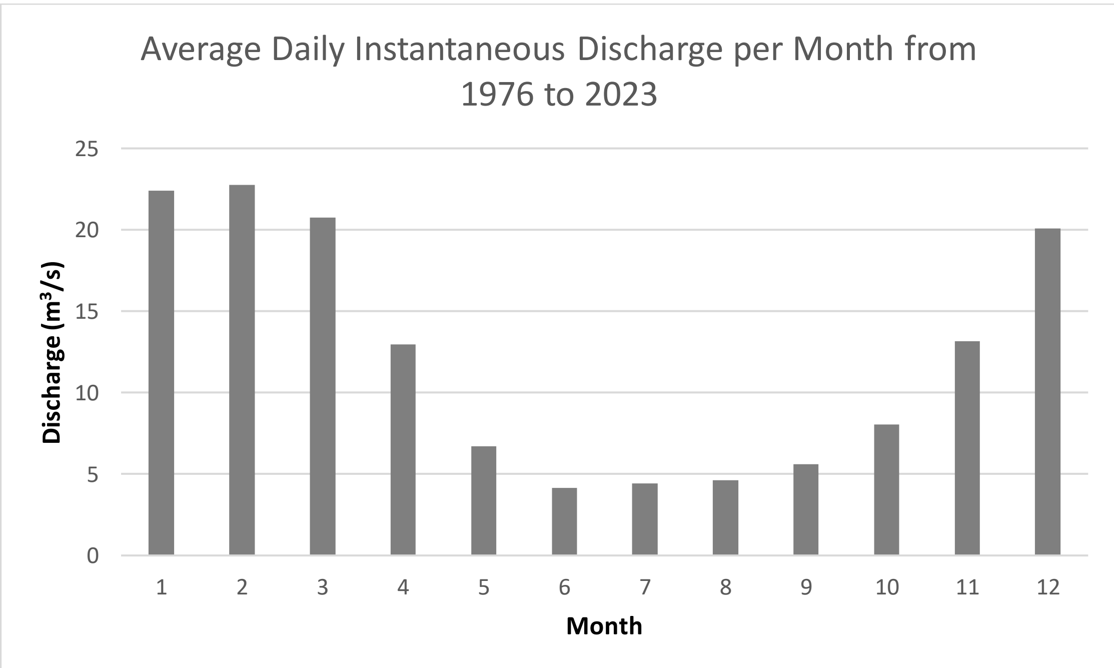

Figure 8: Average Daily Instantaneous Discharge per Month from 1976 to 2023

In addition, a bar graph of flow from 1995 to year end 2023 was analyzed and is shown in Figure 9. This also showed that the highest peak discharges were also during these winter months, generally around January and February. Flow was used to determine periods of interest as opposed to precipitation because the initial goal is to calibrate the rain-on-grid model's ability to predict flow during periods of high variation. As such, to have the results of 6 months, it was determined to begin in November and end after April so the more turbulent and therefore complex flow season is kept intact and examined.

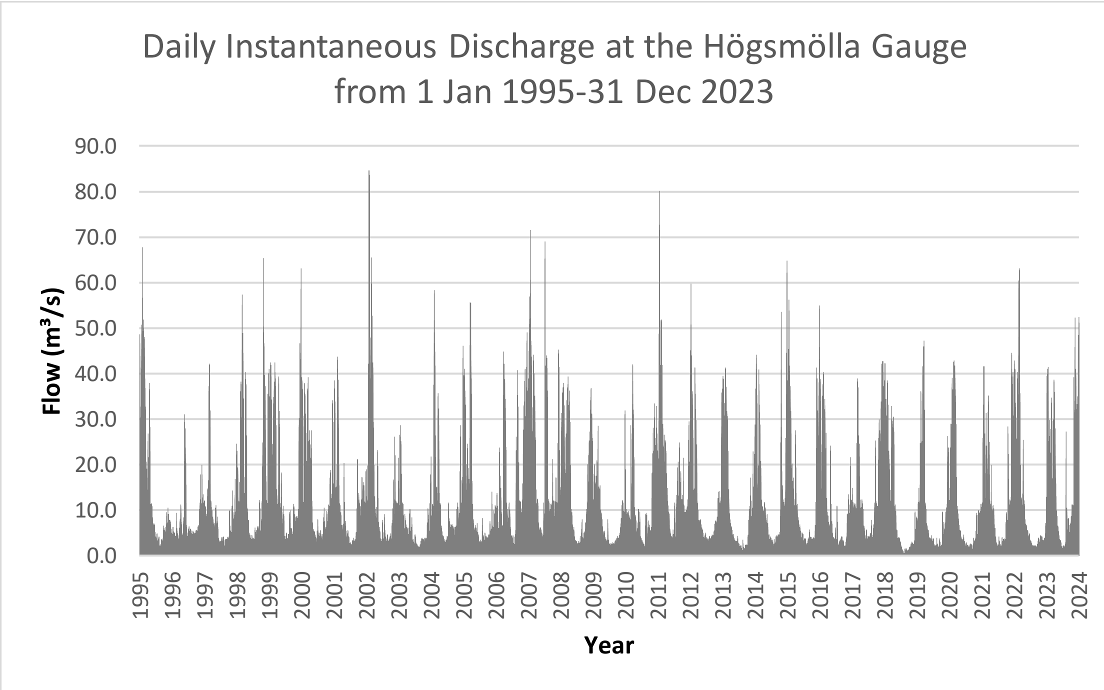

Figure 9: Daily Instantaneous Discharge at the Högsmölla Gauge from 1 Jan 1995-31 Dec 2023

Selection of Years

The years prepared were selected to input into the model based on the requirements for calibration and validation. To calibrate using a shorter-term time (typically the length of one rain event), it is better to use an above average or extreme storm case (Costabile et al., 2021; Ennouini et al., 2023). However, when using a longer-term period to calibrate which includes many rain events, it can be advantageous to include dry and average years in addition to particularly wet years to calibrate and validate (Zeiger and Hubbart, 2021). In this case, calibration was performed with a longer time period similar to Zeigler and Hubbart's study, and as such a mix of high, medium, and low total volume of discharge years were selected. To determine this, the total about of volume of discharge was determined per year, beginning July 1 of the earlier year and finishing a year later on June 30, and sorted, reflected in Table 4. Only the gauge of Högsmölla was used, due to it being the gauging site that represents the entire watershed and the area of interest. While flow records at Högsmölla begins earlier than 1997, they were not included due to incomplete or inconsistent rainfall data prior to 1997, and the yearlong period of 2002-2003 was not included due to missing flow data.

Table 4: Total Instantaneous Daily Flow per Year

Year (1 Jul-30 Jun)	Total instantaneous daily flow from July 1 – following year June 30 (m^3)
2006-2007	7002
2007-2008	6711
1998-1999	6125
2017-2018	5876
2010-2011	5495
2001-2002	5472
2021-2022	5191
1999-2000	5111
2011-2012	4961
2014-2015	4714
2004-2005	4490
2015-2016	4333
1997-1998	4006
2012-2013	3986
2019-2020	3796
2000-2001	3652
2013-2014	3573
2022-2023	3504
2008-2009	3389
2005-2006	3139
1996-1997	3078
2020-2021	3034
2016-2017	2945
2003-2004	2896
2009-2010	2833
2018-2019	2695
2002-2003	2626

For the calibration process, the years used were 2006-2007 because it was the year with the highest total discharge volume, 2001-2002 because it had the highest peak discharge (as evidenced in Figure 9), 2019-2020 because it was an average year, and 2018-2019 because it had the least total discharge volume.

The validation years were similarly selected to represent all possible conditions. These are 2007-2008 because it was the second highest total discharge volume, 2012-2013 because it was an average year, and 2009-2010 because it had the second least total discharge volume.

The prepared precipitation data is then entered into HEC-RAS under unsteady flow data as a boundary condition of precipitation. The specific steady flow data years are later selected in the unsteady flow analysis in correspondence to the calibration, validation, and climate charge scenario stages.

2.1.3 Vulnerability Factor Pre-processing

There are multiple factors that are combined into one value of vulnerability, and includes schools, cultural or municipal buildings, population density, population fragility, railroads, roads, and land use. These factors were selected based on similar factors used in other papers (Dang et al., 2010; Gain et al., 2015; Masood and Takeuchi, 2011; Suriya and Mudgal, 2012; Zhang et al., 2022) and on data availability. Some initial processing of the raw downloaded data had to be performed first.

Because the goal is a raster file and because population data was already in gridded form as a vector file, the same grid was used as a template for a new fishnet layer (this ensures all factors have overlapping cells of the same size and location, and this results in a clean final calculation). However, the population grid was set to a 1-kilometer cell size. For a more detailed result, a 500-meter cell size was used, and was aligned with the population grid.

The data to examine school vulnerability was found on the Lantmateriet geoportal. This contained several layers, including points of past schools. Only layers of presently active schools were merged into a single point layer. A spatial join with the template grid resulted in a sub-final layer that provided number of schools per cell. The maximum number of schools in one grid (22) throughout the watershed established the maximum risk value (1), and equal breaks were used to assign values between 0 – 1 to all grids.

Similarly, another point layer was included in the analysis, which measured relative risk to the public interest buildings of cultural buildings and municipal buildings. This included cultural sites and municipal buildings, found in the Länsstyrelsernas Geodatakatalog and Lantmateriet, respectively. The two layers were combined into one layer of public interest buildings, and the same steps were repeated as for the school vulnerability, also resulting in values 0-1 to each grid.

Two aspects of vulnerability stem from population statistics (Statistikmyndigheten SCB, 2024). These are population density and population fragility. Population fragility refers to vulnerability as a cause of age, due to increased difficulties with disaster communication and response (Clark et al., 1998; Müller et al., 2011). To determine population fragility, the vulnerable age groups are determined by two papers. In one paper examining vulnerability, it determined people over the age of 60 as vulnerable (Bolin and Klenow, 1983). Another paper that was analyzing vulnerability to determine flood risk, by Zhang et al. (2022), identified vulnerable age groups as children younger than 10 and adults 60 or older. As such, these age groups were used as a previously identified more fragile age groups. Statistikmyndigheten SCB data provided 5-year buckets and had the count of people in each bucket for each grid cell. To create a grid of values of between 0 and 1 (most at risk), simple calculations were made in the attribute table, totaling the number of people in the vulnerable buckets for each grid. Then the grid's percentage of more fragile age groups was determined, and the decimal value was used as the value of risk (1 being 100% of the grid's population is of a fragile age group), which assumes linearity of vulnerability and the number of people.

For population density (Statistikmyndigheten SCB, 2024), the grid was clipped to the watershed to find the highest density found in a grid completely in the watershed, and the rest of the watershed was divided as a percentage of this highest density, which provides a relative population density risk of the watershed. Any grid without population took a vulnerability value of 0.

The infrastructure of transport was also considered with the layers of roads and railways, which were exported from Trafikverket in 2024. To determine a vulnerability grid, roads and railways were merged into a single polyline shapefile. Then, the grid template was converted into a raster, so that the next step could be performed. Using the grid template raster and the infrastructure pathways shapefile, the tool *Line Density* was used to attribute the total quantity of lines in each grid cell in relation to the overall cell size. Because cell size is standardized, this leads to a value that can be compared between cells. The maximum density in the watershed was determined, and raster calculator was used to determine each cell value's percentage of the maximum density. The maximum density is closer to 1, and less dense is closer to 0.

The same land cover file as used in the HEC-RAS preparation steps (Naturvårdsverkets, n.d.) was used to determine vulnerability of the land cover itself. Using the method of Masood and Takeuchi (2011), land use was prepared by first reclassifying the values of any urban areas (labeled as 51, 52, and 52) to a high vulnerability of 10, and the values of agricultural land (with a label of 3) to a low vulnerability of 2. All other land covers are identified as no vulnerability and set to 0.

Next, the raster to converted to a polygon vector file. Using this polygon file, the *Tabulate Intersection* tool is used to find the percentage areas of vulnerability values 10 and 2 within each of the template grid's cell. The percentage areas are weighted as such, the percentage of area with a value of 10 were multiplied by 1 and the percentage of area with a value of 2 was multiplied by .2. These two weighted percentages were then combined and divided by 100 for a result that ranges from 0 to 1 (closer to 1 being more area is covered by vulnerable land). To find relative risk of the watershed, the area was clipped to find the grid cell with the highest percentage of vulnerable, and the file was recalculated to find the respective percentage of the highest land vulnerability, which ranged between 0 and 1.

To transform all layers to rasters, all polygons were transformed using the raster template created earlier to set cell size, extent, and to snap them.

2.1.4 Climate Scenario Data

The model used will be the RCP8.5 model by the IPCC (1992). While there are numerous possibilities of what will happen to the climate by 2100, the RCP8.5 model is used in this study because it is a realistic worst-case scenario, in which no effective climate change policies are able to mitigate the quantity of emissions and is often used in other studies as the anticipated worst-case (Pörtner et al., 2019; Riahi et al., 2011).

The RCP8.5's model of Sweden's percent change in precipitation changes month to month and regionally (Lind and Kjellström, 2008). To simplify the model in HEC-RAS rain-on-grid, Sweden's average percentage change of rainfall in the RCP8.5 model is used as a multiplication factor. According to the Swedish Meteorological and Hydrological Institute's Advanced Climate Change Scenario Service, the RCP8.5 model predicts a 22.4% increase in precipitation on average in Sweden between the reference years of 1971-2000 and the future years of 2071-2100 (SMHI, 2024a).

However, because this is a localized study, this expected increase of precipitation should be applied specifically to the historical precipitation of the watershed. As such, this percentage of 22.4% was used to multiply the wettest year in (hourly) record, which was the year 2006-2007. To create the data to be input into HEC-RAS, the precipitation of the year 2006-2007 was modified in Microsoft's Excel version 2410 build 18129.20116 developed in Redmond, Washington (USA) by taking each hourly precipitation value and multiplying this by 1.224. This provides the future hourly rain for a wet year for 2100.

2.2 Hazard Map Method using HEC-RAS 2D Rain-on-Grid

The two hazard maps are created using HEC-RAS's hydraulic-hydrodynamic 2D unsteady flow model with rain-on-grid. The rain-on-grid set up followed the HEC-RAS 2D manual, and used the preprocessed data described earlier (DEM, Manning's roughness coefficient, infiltration layer, perimeter, mesh grid, and external boundary condition). The unsteady flow input was created using the precipitation data for a given year. The HEC-RAS system used was the most up to date version at the time, HEC-RAS 6.4.1, and used two Dell Inspiron 16 computers simultaneously to decrease the time required to create an accurate model because computation time ranged between 43-51 hours for each run. Many runs were necessary to create an accurate model due to the calibration and validation procedure. Once the best parameters are found, the heaviest rainfall year is used as the year with the highest hazard, providing the first hazard map. The second hazard map for the climate scenario was then created using the previously prepared climate scenario data.

2.2.1 Calibration and Validation

To calibrate this model, the sensitivity analysis is performed using years 2006-2007, 2001-2002, 2019-2020, and 2018-2019. The validation used the years 2007-2008, 2012-2013, and 2009-2010. The years were selected during the Preparation of gauge data step as described earlier. To be considered an acceptable model, the performance metrics had to be within the satisfactory range or higher when comparing simulated and observed daily flow data.

To take the simulated flow values at the same locations as the observed flow gauges, two profile lines were placed at a traverse at the points of the Högsmölla and Ellinge gauges, and the flow graphs are calculated at those profile lines. As mentioned in the background, the best way to calibrate and validate the data is with split-site, split-time, and with different methods (like gauge and flood area). In this case, a split-site and split-time was possible. Two gauge sites located at two different locations in the watershed had available data for many years, which allowed for testing of dry, normal, and wet years. Because of the quantity of years, it was possible to make two separate groups of these varying rain years, so the calibration and validation sets of data did not overlap but shared a richness of data.

Performance Metrics Used for Calibration and Validation

The performance metrics used to compare the simulated and observed daily flow data was selected based on hydraulic and hydrologic modeling literature. There are a variety of performance metric statistics that test how well simulated values mirror the real observed values. Each study needs multiple statistics to measure multiple types of differences, such as if the simulated and observed peaks are a similar volume at a similar time, if all simulated values consistently lower/higher than the observed, are if the increases and decreases occur similarly, etc.).

The two earliest benchmark papers on HEC-RAS rain-on-grid are by Costabile et al. (2021) and Zeigler and Hubbart (2021). Because Costabile et al. (2021) uses aerial imagery of observed flooding to assess the performance of the model and this data is not available for the Kävlinge, the evaluation method from Zeigler and Hubbart (2021) is considered, which uses the Nash-Sutcliffe Efficiency (NSE), Coefficient of Determination (R^2), Percent Bias (PBIAS), and the ratio of the root mean square error to the standard deviation (RSR). While a meta-analysis of the best hydrological model performance metric to use found that RSR is best used for smaller datasets than this study is examining, the NSE, R^2, and PBIAS were determined to be the best combination of performance metrics possible for the watershed spatial scale and daily discharge data (Moriasi et al., 2015). These three performance metrics were therefore selected to be used in this study, and are explained as follows.

Nash-Sutcliffe Efficiency

The Nash-Sutcliffe Efficiency (NSE) is described by Nash and Sutcliffe (1970) as a normalized statistic that compares the relative variance (noise) to the measured data variance. This essentially measures how much of the variance in the data is a result of noise, and how well the observed and simulated values coincide. If plotted, then a perfect NSE would fit a 1:1 line, where higher observations are matched by simulated values and lower observations correspond to lower simulated values. The equation for this measure is as follows:

$$NSE = 1 - \left[\frac{\sum_{i=1}^{n}(Y_i^{obs} - Y_i^{sim})^2}{\sum_{i=1}^{n}(Y_i^{obs} - \bar{Y}^{obs})^2}\right] \quad (10)$$

where $Y_i^{obs}$is the observation discharge and Y_i^{sim} is the simulated discharge for a given time point, and $\bar{Y}^{obs}$ is the average observed discharge. The NSE ranges from negative infinity to 1, where 1 is the ideal value. Generally, values between 0 and 1 are satisfactory, but .5 or higher is a better cut-off for a robust model (Moriasi et al., 2007). A value at or less than zero means that the mean observed value is better at predicting than the simulated value and is therefore unacceptable.

Coefficient of Determination

The Coefficient of Determination (R^2) is the amount of variance in the observed data that is explained by the model. The value ranges between 0 and 1. The ideal R^2 is 1, which would mean that all of the variance of the observed data can be explained by the model and there is no variance stemming from errors. Anything between .5 and 1 is considered acceptable (Moriasi et al., 2007). The equation to calculate R^2 is as follows:

$$R^2 = \left[\frac{\sum_{i=1}^{n}(Y_i^{obs} - \bar{Y}^{obs})(Y_i^{sim} - \bar{Y}^{sim})}{\sqrt{(Y_i^{obs} - \bar{Y}^{obs})^2}\sqrt{(Y_i^{sim} - \bar{Y}^{sim})^2}}\right]^2 \quad (11)$$

where Y_i^{obs} and Y_i^{sim} are the observation and simulation discharges respectively, and $\bar{Y}^{obs}$ and $\bar{Y}^{sim}$ are the average observed and average simulated discharges respectively (Moriasi et al., 2015). A disadvantage of R^2 is that is sensitive to outliers and does not account for magnitude differences (for example, observed flow basculates between values 2 and 10; a simulated flow that perfectly emulates the form of the observed flows but with values between 20 and 100 could have a perfect R^2 of 1).

Percent Bias

The Percent Bias (PBIAS) measures the extent of which simulated values tend to be larger or smaller than the observed values. An ideal PBIAS is 0, and positive values indicate that the model underestimates the discharge and negative values means that the model is overestimating. For example, a negative PBIAS means that the model more consistently calculates higher discharge quantities than was observed. According to Moriasi et al. (2007), the amount of percent bias can be up to 25% for streamflow discharge. The equation for PBIAS is calculated as follows:

$$PBIAS = \left[\frac{\sum_{i=1}^{n}(Y_i^{obs} - Y_i^{sim}) * 100}{\sum_{i=1}^{n}(Y_i^{obs})}\right] \qquad (12)$$

Parameters to Calibrate and Validate

One of the most important parameters to calibrate in HEC-RAS rain-on-grid is the infiltration. This can be done by adjusting the curve number, abstraction ratio and minimum infiltration rate. In the sensitivity analysis in the Kävlinge Watershed, the curve number was the only change that led to more reliable results. The Manning's roughness coefficients were then tested with a sensitivity analysis in the +/- 50% range. After multitudes of iterations, the values that resulted in the best calibration performance tests were determined; the final Manning's roughness coefficients and infiltration values can be referenced to in the results section.

One of the factors that had a large impact on the accuracy of the results was using a variable time step, specifically with the Courant number method. The Courant number is a ratio of distance covered by water in a time step and the size of the grid cell (Hydrologic Engineering Center, n.d.-b). The variable time step method that uses the Courant number will halve the time step, should the Courant number be above the maximum Courant number given by the user in the parameters, which means the water is moving too quickly for the desired calculation rate. If during the simulation the Courant number is slower than the minimum Courant number given by the user in the parameters, then the time step (rate of calculation) will double. The Courant parameters were tested to find the most optimal. However, there was not a significant change between numbers, which is expected in flat terrain because water is not changing direction or moving as quickly as other watersheds (Hydrologic Engineering Center, n.d.-b). As such, the values that were associated with the fastest model run were used. These courant numbers are a maximum Courant of 2.0, minimum Courant of .2, 4 steps below minimum before doubling, a maximum of 16 hours doubling base time step, and a maximum of 225 seconds for halving base time step.

During the initial iterations and depending on the year, the dry start-up time varied, with the model beginning only when the first precipitation in the time period occurred. To ameliorate this and to begin with water flowing prior to any rain, the Initial Condition option called Interpolation from Previously Computed Results was used. Previous simulations were tested to find a time where discharge corresponded to observed discharge and resulted in the best performances. After adding the initial conditions, the starting period's flow values were improved.

2.2.2 Running a climate scenario

At this point the model has been confirmed to be effective. Using the calibrated and validated model, it can now be used to run potential scenarios and hypothetical events. In this case, the altered precipitation in 2100 which is caused by climate change will be examined.

The precipitation data for the wet-year climate scenario in year 2100 is then input into the model following the same methods as the historical records, using the same parameters and conditions that were already calibrated and validated for this watershed. The result is the climate change wet year in 2100 flooding hazard.

2.2.3 Exportation and Visualization of Flood Depth

Now, in RAS mapper, the maximum daily peak of flooding for all results can be exported. Because this study focuses on the rainiest year historical year and the climate scenario's rainiest year in 2100, these two runs are exported to create hazard maps in ArcGIS Pro. The hazard, represented by water depth on the peak day, was exported from HEC-RAS with a cell size of 10 by 10 meters to balance detail and file size.

Once both the results from 2006-2007 and the climate scenario were in ArcGIS Pro, export by attributes was used to set a water depth threshold for visualization purposes. This is a typical necessary step for HEC-RAS rain-on-grid models, and the water depth threshold is typically set to 0.1 meter (Ennouini et al., 2024).

To focus the area on the last segment of the river, the layer is then extracted using a mask of the area of interest. Following this, the resulting layers are processed in reclassify. This simplified the water depths into five categories: water depths up to 1 meter, between 1 and 2 meters, 2 and 3 meters, 3 and 4 meters, and more than 4 meters. These are also the categories of water hazard, with very low hazard, low hazard, moderate hazard, high hazard, and very high hazard.

2.3 Vulnerability Map Method with Analytic Hierarchy Process

As seen in the literature review, there are numerous approaches to analyzing and calculating risk and vulnerability. One of the largest differences in methodologies between these papers is the difference in factors and indicators used to calculate overall vulnerability, likely due to differences in data availability and variation in importance. An example of variation in importance is that a couple of studies in India used education and literacy as an aspect of vulnerability due to impact on information dispersal, but given Sweden's socioeconomic level, those factors are not taken into account.

The factors selected to indicate vulnerability were chosen based on relevance according to the literature review, Sweden's current socioeconomic level, and which indicators had publicly facing data. As such, the datasets considered to impact the area's vulnerability are land use (urban area or agricultural), "primary" infrastructure (schools, roads, railways), population factors (density and fragility), and "secondary" infrastructure (municipal buildings and cultural sites, which are economically important but not impacting emergency evacuations). These factors are important economically as sources of income (agriculture, cultural sites, roads, railway) and long-term assets (all infrastructure), in emergency situations as evacuation routes and shelters (schools, roads, rail, and municipal buildings), and socially due to increased difficulty of movement (population factors) and assets to education (schools).

2.3.1 Analytic Hierarchy Process

These vulnerability factors should not be weighted equally. As such, the earlier explained, commonly used analytic hierarchy process developed by Saaty in 1980 is used, with help from a 2006 tutorial developed by Teknomo. Typically, a panel of experts are consulted to perform the comparison. However, in this case, previous studies using HEC-RAS and GIS to perform risk analyses that have already demanded experts are used to generate a general ranking of importance, and this is used to perform the pairwise comparison. As such, the ranking from more important to less important was: land use; population factors and primary infrastructure; and secondary infrastructure (Dang et al., 2010; Gain et al., 2015; Masood and Takeuchi, 2011; Suriya and Mudgal, 2012; Zhang et al., 2022). This ranking informed the pairwise comparison found in Table 5. Likewise, in the chart, the resulting weights that were calculated using Microsoft's Excel version 2410 build 18129.20116 with the method as explained by Teknomo (2006) are listed. Because there are not many variables and the ranking was very clear, the consistency ratio (which measures reliability of the judgements and should be less than 10%) was 0.01.

Table 5: Pairwise Comparison of Vulnerability Factors and Resulting Normalized Weights

	Schools	Roads/Rail-ways	Land Cover	Population Density	Population Fragility	Municipal Buildings/ Cultural Sites	**Weight (Normal-ized)**
Schools	1	1	1/2	2	2	3	**0.195**
Roads/Rail-ways	1	1	1/2	2	2	3	**0.195**
Land Cover	2	2	1	3	3	4	**0.332**
Population Density	1/2	1/2	1/3	1	1	2	**0.108**
Population Fragility	1/2	1/2	1/3	1	1	2	**0.108**
Municipal Buildings/ Cultural Sites	1/3	1/3	1/4	1/2	1/2	1	**0.064**

Once the weighing has been found, raster calculator was used to combine all vulnerability factors together with their determined weighting, as referenced in Table 5. The script used for the raster calculator can be found in Appendix 2. The final combined vulnerability layer is then multiplied to create 5 categories of vulnerability, where 1 is very low, 2 is low, 3 is moderate, 4 is high, and 5 is very high vulnerability. The multiplying factor of 7.06 was decided as such so the highest value of risk in the area (about 0.7) will have the highest vulnerability value of 5, because relative vulnerability is of interest and not a value of absolute vulnerability.

2.4 Risk Map Method

To create the risk maps, the equation R = H x V is used. A risk matrix multiplies hazard and vulnerability and displays the categorized results by risk level (Ryu et al., 2017). Both hazard and vulnerability range between 1 and 5 (5 being the highest severity), and the results can be categorized into four groups, relative low, moderate, major, and severe levels of risk (Zhang et al., 2022). While Zhang et al.'s (2022) methodology was used, their use of the term 'safe' for the lowest level of hazard is substituted with the term 'low', to signify that wherever there is a risk, it cannot be considered completely safe.

Raster calculator is used for both present-day and climate change scenarios to multiply the vulnerability layer and respective hazard map to generate the two risk maps. The risk maps are then categorized using the values as seen in Figure 10.

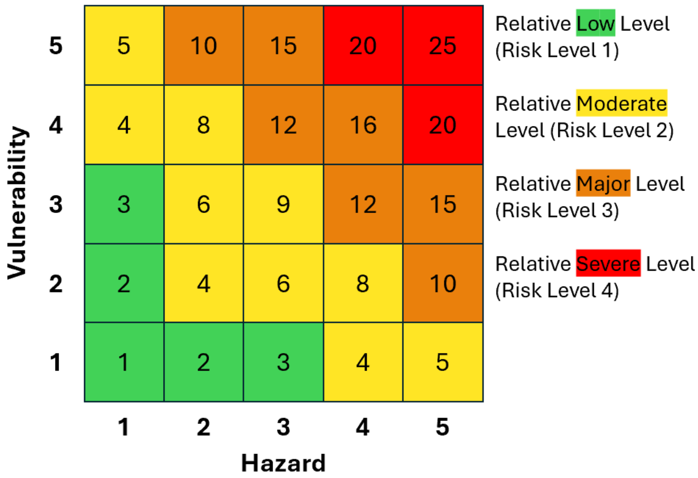

Figure 10: Risk Assessment Combination and Categorization

3. Results

3.1 Calibration and Validation of the HEC-RAS Rain-on-Grid Model

The parameter conditions that led to the best statistics were a Manning's roughness coefficient of +40 % and an infiltration adjustment of -40%. A positive change to the Manning's roughness coefficient means that the water in the model needs to experience increased friction to be more accurate. The original values of Manning's roughness ranged between 0.03 to 0.12, and after calibration the range was from 0.042 to 0.168. The attribution of values and the land use types can be found in Appendix 1.

A negative change in the infiltration adjustment likewise removes and slows water in the model, and the original CN values ranged between 58 to 100 and were adjusted to range between 34.8 to 60. For this model to be more accurate, the amount of rain that percolates into the ground as opposed to becoming run-off had to be more than the original expected quantity. The resulting statistics of the most ideal parameters can be found in Table 6.

Table 6: Calibration and Validation Performance Metric Statistics

		Högsmölla			Ellinge		
	Year	**NSE**	**R^2**	**PBIAS**	**NSE**	**R^2**	**PBIAS**
Calibration	2006-2007	0.62	0.65	18.6%	0.97	0.65	29.8%
	2001-2002	0.79	0.77	11.8%	0.91	0.51	22.8%
	2019-2020	0.75	0.66	4.3%	0.97	0.75	17.5%
	2018-2019	0.60	0.72	32.6%	0.95	0.72	11.1%
Validation	2007-2008	0.62	0.63	27.4%	0.98	0.71	20.7%
	2012-2013	0.50	0.46	37.6%	0.98	0.50	7.6%
	2009-2010	-0.34	0.00	11.3%	0.88	0.09	3.6%

Highlighted in dark green are values within the commonly used Moriasi et al. (2007) standards, and light green are the values considered satisfactory by the Hydrologic Engineering Center performance metric standard (Hydrologic Engineering Center, n.d.-a). Orange values are considered unsatisfactory.

The calibration phase was relatively successful with only an occasional performance metric value considered unsatisfactory by Moriasi and co-author's (2007) standards. Only the wettest 6-month time period of 2006-2007 and the driest 6-months 2018-2019 had a discrepancy each, both of which for the PBIAS for the Ellinge and Högsmölla station respectively, as listed in Table 6. However, in comparison to the unsatisfactory PBIAS values prior to calibration, they are not far from the acceptable range. Other than this, all statistics were suitable. An example of the calibrated wettest period's (November 2006-April 2007) hydrograph comparing the observed and simulated discharge can be seen in Figure 11. Though the hydrographs between observed and simulated are not exact copies, the shape of both Högsmölla and Ellinge's hydrographs largely mirrors the observed hydrographs, and most peaks are close to the same quantity of discharge and the simulated dips are slightly lower than the observed. According to the performance metrics, the Ellinge gauge station is modelled slightly more accurately than the Högsmölla station, particularly seen in the NSE values. This is also visualized in Figure 11, as the Ellinge simulated values follow the observed discharge values than for Högsmölla. The other hydrographs for the rest of the rest of the calibrated years can be found in Appendix 3.

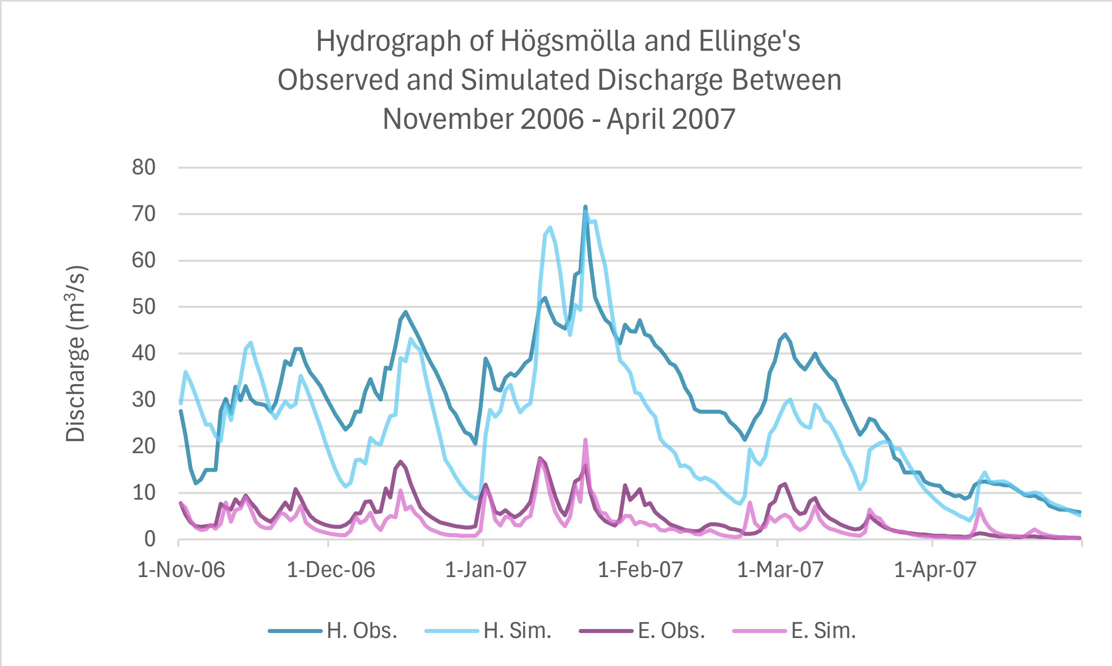

Figure 11: Calibration hydrograph of Högsmölla and Ellinge's Observed and Simulated Discharge Between November 2006 - April 2007, a 6-month period used for calibration for the HEC-RAS rain-on-grid model for the Kävlinge River.

The validation run had mostly acceptable statistics. However, the second driest year 2009-2010 had problematic results, the NSE at Högsmölla and both stations' R^2 were unacceptable. However, the second wettest year 2007-2008 and the validation average year 2012-2013 had nearly perfect results, with one discrepancy each, for the PBIAS and R^2 respectively. Unlike the dry year, these values were extremely close to being in the acceptable range. Figure 12 shows the example of the validation period November 2007-April 2008's hydrograph comparing the observed and simulated hydrographs for both Högsmölla and Ellinge. In comparison with the calibration year, there are more differences between the hydrographs, but the simulated hydrographs still follow the observed hydrographs well. While there are more differences in the discharge value of the peaks in the validation run, the differences between the observed and simulated dips are similar as to in the calibration scenario. Similar to the calibrated hydrograph, the Ellinge gauge station is better performing than Högsmölla. The other two years of validation's hydrographs can be referenced in Appendix 4.

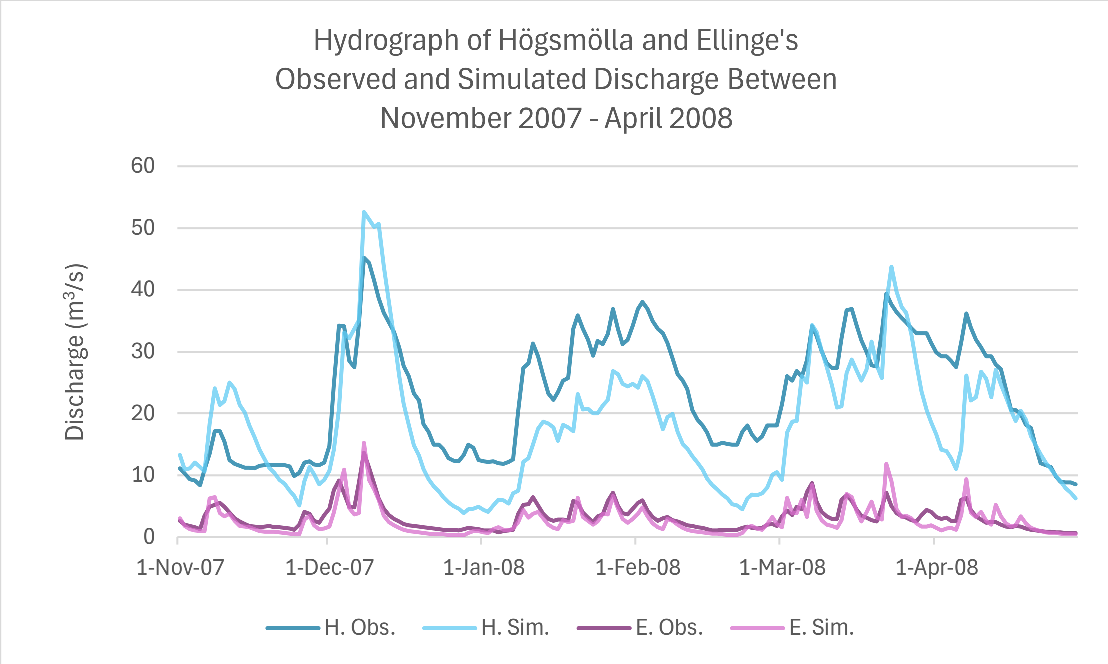

Figure 12: Validation hydrograph of Högsmölla and Ellinge's Observed and Simulated Discharge Between November 2007 - April 2008, a 6-month period used for validation of the HEC-RAS rain-on-grid model for the Kävlinge River.

There are many possible reasons for discrepancies in these statistics, which includes impact of snowmelt, groundwater, and fact there are many dams along the Kävlinge River, namely the Vombsjön dam that controls a majority of water of the watershed, as well as the Eslöv water treatment facility that is just upstream of Ellinge. However, because the majority of statistics are suitable, this model's parameters were adequate for further use to model the hazard. In addition, it is convenient that the only truly inadequate year was a dry year while this study's purpose is to model wet years, and therefore this uncertainty is less important.

3.2 Hazard Map – Present-day High Rain Year

The flooding of a present-day high rain year, which by historical record analysis was 2006-2007, shows mostly light flooding on land away from the Kävlinge River, and the most severe flooding typically on or close to the river, as seen in Figure 13. There are very few areas with high flooding of between 3-4 meters, and extremely rare cells not obviously seen of severe flooding of more than 4 meters. The area away from the river that experiences flooding is mostly at the very low hazard level, with less than a meter of water. There are some areas that have higher flooding, between 1-2 meters of depth.

Upon an inspection with satellite imagery, most areas flooded are flooding agricultural fields. While this is problematic for farmers and potentially damaging economically, the flooding is relatively light. Where the flooding is more severe, this covers less area. Two particular areas of concern identified were in the town of Kävlinge, because the river has high flooding in the area in close proximity to the city, and close to the mouth of the river, while having a depth of only up to 2 meters, the flooding is extremely wide and covers a large area. These areas can be examined up close in Figure 14.

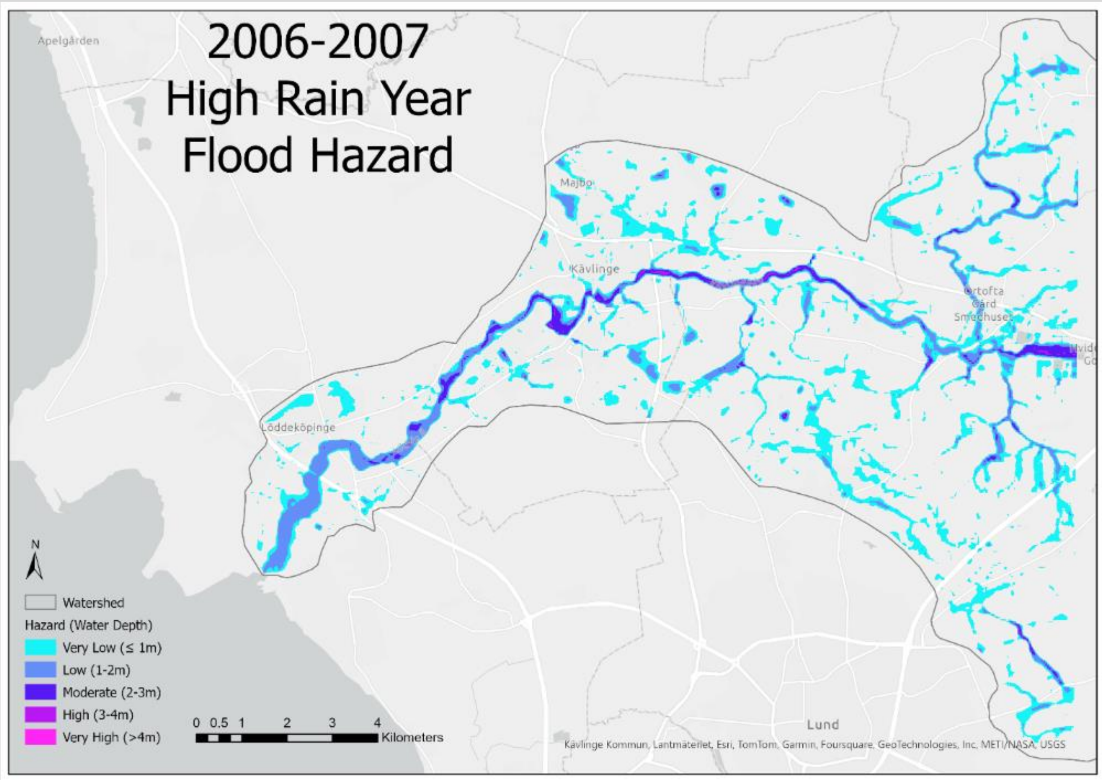

Figure 13: 2006-2007 High Rain Year Flood Hazard
Taken from the HEC-RAS rain-on-grid model for the Kävlinge River. The flooding is representative of the peak flood height during the November 2006 – April 2007 period, the wettest period in historically hourly rainfall.

Examining the town of Kävlinge up close reveals that the town has partially planned with consideration for flooding zones. Where flooding is worst, in the southeast and southwest areas close to the river, the riverbanks are generous, and suggest the town has given the river a margin with the natural freedom to swell as necessary without needing complex infrastructure to address flooding. The most problematic area as shown in Figure 14 is on the northern riverbank in the town of Kävlinge's central area, to the east of the railway bridge. There are several properties in a relatively dense residential area that are impacted by up to moderate hazard flooding.

The central town has a few very small patches of very low hazard flooding. However, there are larger patches of very low hazard flooding and low hazard flooding on the outskirts of the town. In the northwest corner, there are two patches of what appears to be a residential area partially covered by very low and low hazard flooding. In the northeast corner and near the U-shaped bend, commercial areas are covered by a large area of very low hazard flooding. Where the high and very high hazard flooding is in the Kävlinge, this area remains in green space and close to the original path of the river.

The other area identified as most problematic is leading up to the mouth of the river. The flooding bypasses Löddeköpinge, a town to the north of the Kävlinge and the last town along the river. The river swells with flooding to towards the south, maintaining nearly the same river edge as normal. Halfway between Löddeköpinge and the sea on the east bank, there is either residential, farming, or a combination of those infrastructure that is partially covered by very low and low hazard flooding. The rest of the wide area of very low and low hazard flooding is in agricultural or green space areas.

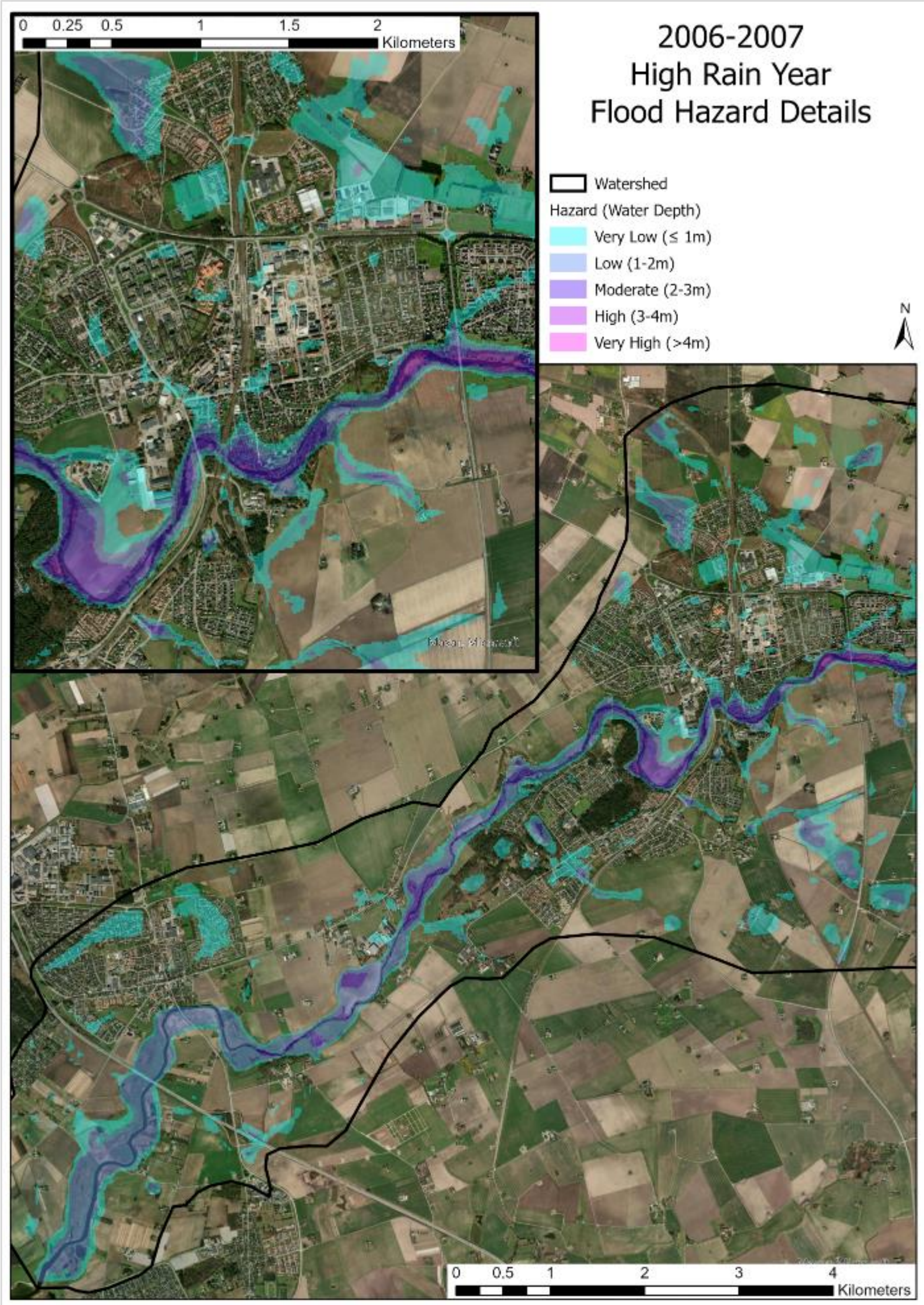

Figure 14: 2006-2007 High Rain Year Flood Hazard Details
Taken from the HEC-RAS rain-on-grid model for the Kävlinge River. The flooding is representative of the peak flood height during the November 2006 – April 2007 period, the wettest period in historically hourly rainfall. Satellite imagery from ESRI's basemap collection.

3.3 Hazard Map – RCP8.5 Scenario High Rain Year

There are not many differences between the climate scenario's high rain year in 2100 and the high rain year in 2006-2007, as displayed in Figure 15. On the higher scale, the differences are particularly difficult to notice on a first glance. However, in comparison, the differences present themselves in two ways. First is that along the river, especially towards the mouth of the river, the breadth of flooding is wider and the general flooding along the river covers a larger area. However, the "puddled" flooding outside of the river area have very little change in size and depth. The depth of the flooding is also more severe, mainly in towards the middle-east area of the Kävlinge River focus segment. This includes the river in the town of Kävlinge and specifically to the east of the town of Kävlinge.

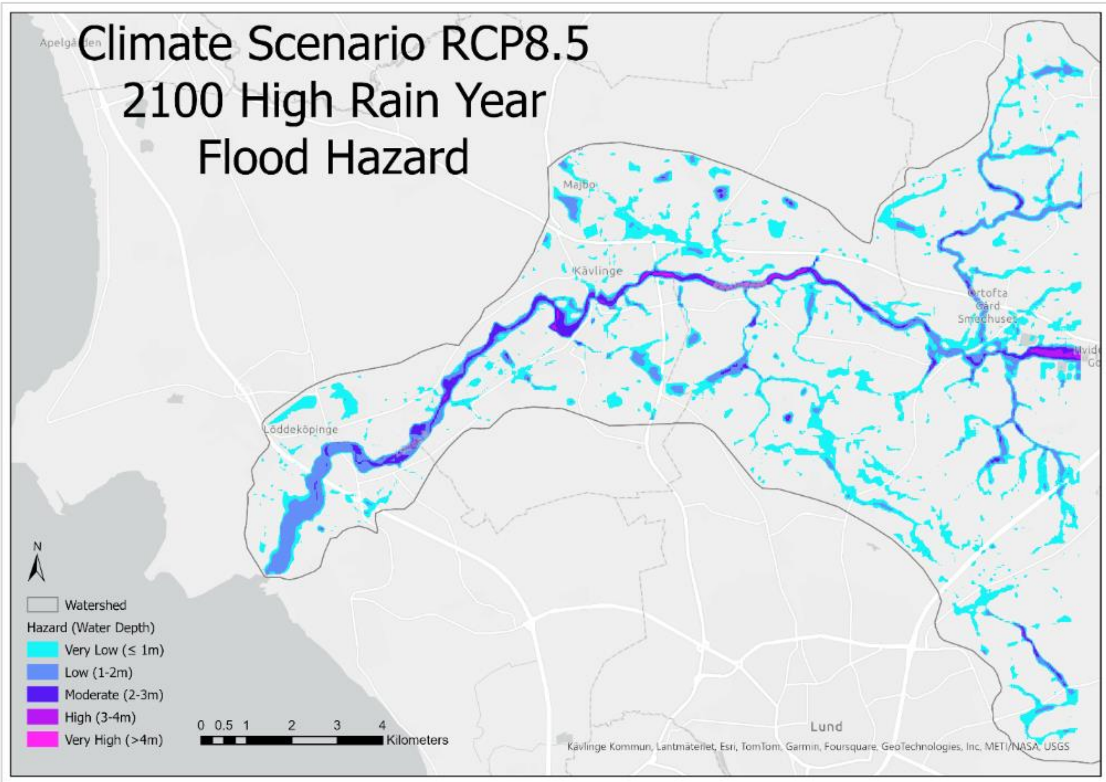

Figure 15: Climate Scenario RCP8.5 2100 High Rain Year Flood Hazard
Taken from the HEC-RAS rain-on-grid model for the Kävlinge River. The flooding is representative of the peak flood height during a 6-month high rain period in 2100 using the climate scenario RCP8.5.

The increase of flood severity in the town of Kävlinge can be found in Figure 16. The extent of high and very high hazard flooding is larger than in 2006-2007. This is true throughout the area that is the Kävlinge River, particularly in three areas. One of these areas is in the U-shaped area in the west, however this space is generally flooding green space except for some commercial buildings. In the climate scenario, this area is more flooded in area in total, and has more very high hazard flooding than in 2006-2007. Another area is in the east, where the flooding has slightly encroached towards the residential area to the north. This area may be of concern due to the quick deepening of the hazard level towards the center of the river, and because the extent of high and very high hazard flooding is larger than that in the 2006-2007 model. The central area to the east of the railway bridge is also problematic, due to the dual encroachment of flooding and increased hazard severity in the area.

Other small flooding zones in the town of Kävlinge have not shown noticeable changes when compared to 2006-2007 levels and area. The flooding downriver, though only mostly extends in area and relatively little in severity, does not impact any new areas of concern. Löddeköpinge’s firm riverbank remains in the same location, leaving the town untouched by flooding of the Kävlinge, apart from a small encroachment on a seemingly commercial property in Löddeköpinge’s southwest (shown by a large white building next to the river).

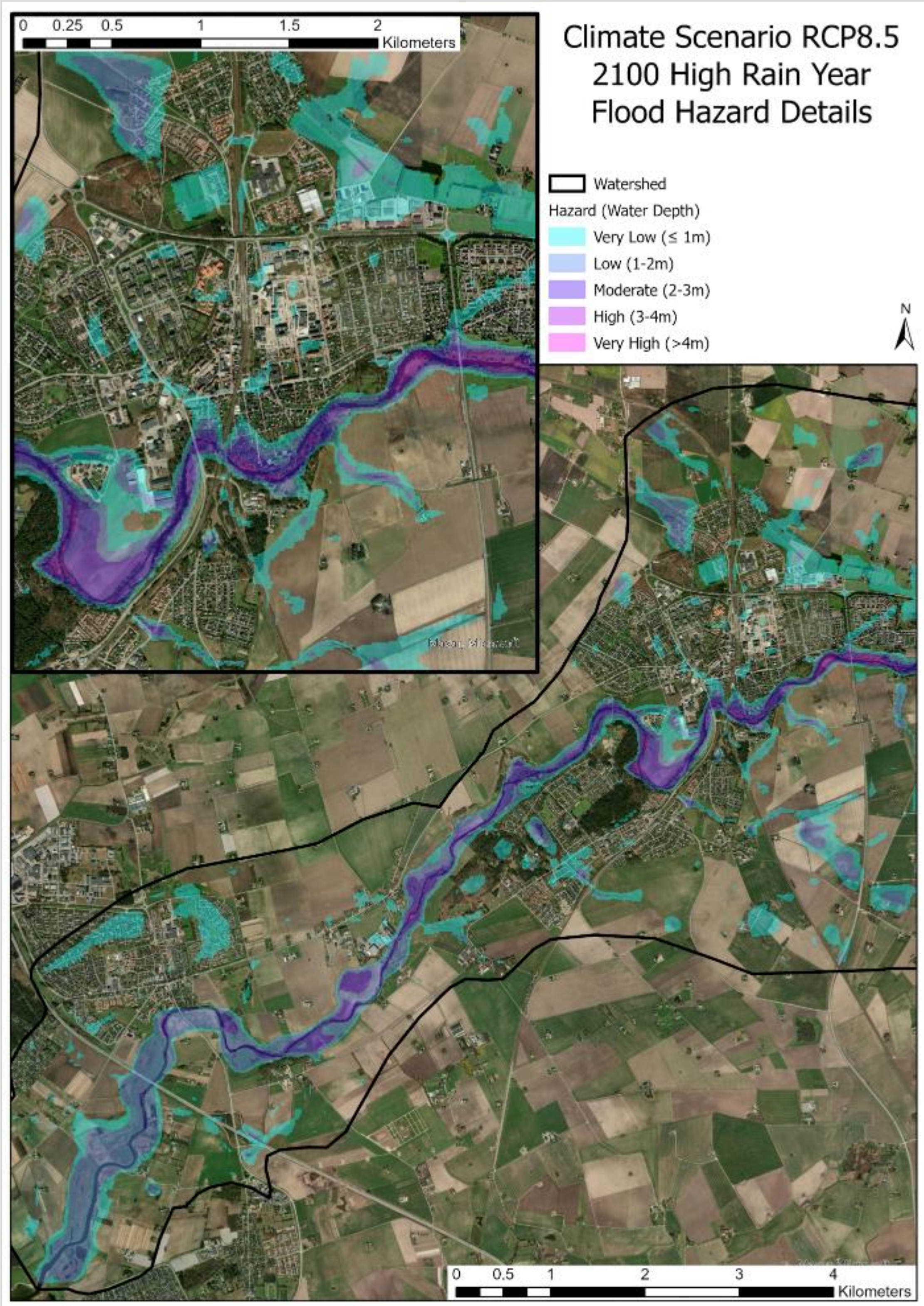

Figure 16: Climate Scenario RCP8.5 2100 High Rain Year Flood Hazard Details Taken from the HEC-RAS rain-on-grid model for the Kävlinge River. The flooding is representative of the peak flood height during a 6-month high rain period in 2100 using the climate scenario RCP8.5. Satellite imagery is current, and from ESRI's basemap collection.

3.4 Vulnerability Map

A map of each factor of vulnerability prior to weighting and totaling can be found in Appendices 5-10. The final resulting total vulnerability map, as seen in Figure 17, indicates that overall, the vulnerability throughout the watershed is very low. As expected, the last leg of the river, and the area to be examined in the risk maps, has a generally higher vulnerability than the rest of the watershed. However, most of the vulnerability in that area is still at a low vulnerability, with occasional areas of moderate vulnerability. Where the town of Kävlinge is, there are several areas of high vulnerability. This is also as expected, due to the higher prevalence and density of buildings (school, cultural, and homes), population, and infrastructure such as roads.

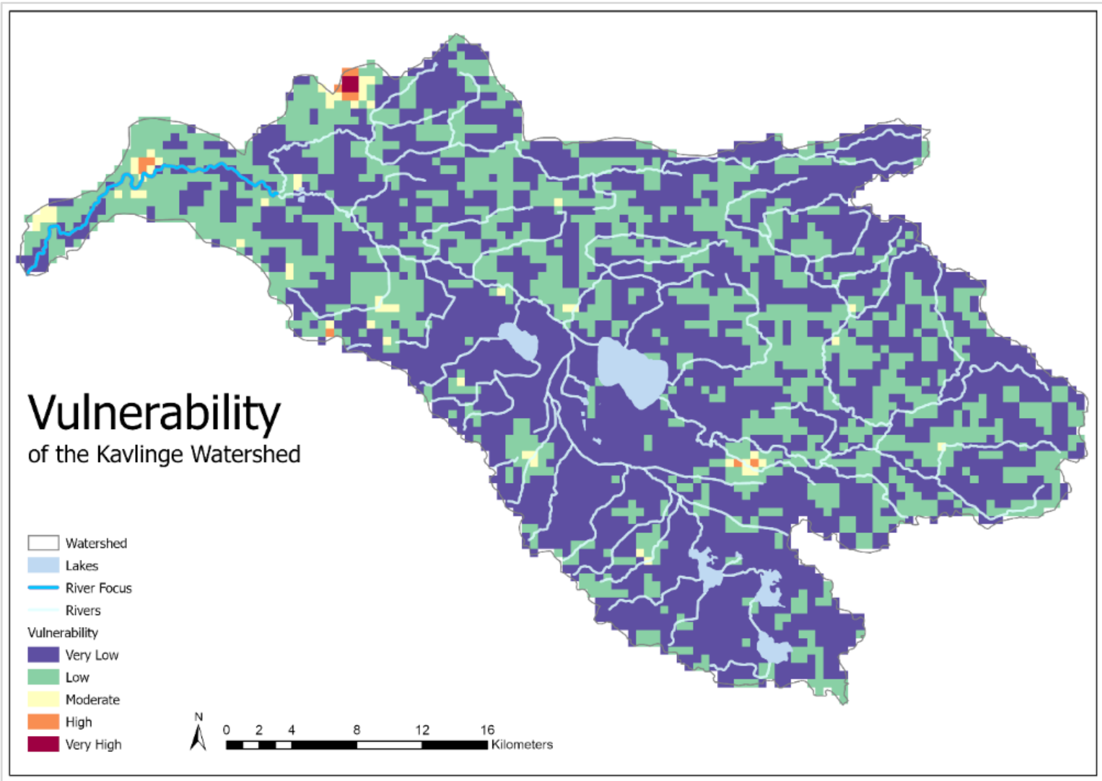

Figure 17: Vulnerability Map of the Kävlinge Watershed
AHP formed total relative vulnerability using ESRI's ArcGIS Pro.

What was unexpected was the very high vulnerability in Eslöv. It was unexpected due to its proximity to the watershed boundary and therefore was not certain to be fully included. However, it appears that much of the town is within the watershed and is a more expansive area than Kävlinge with a very high vulnerability in the center. While this means that Eslöv has a considerable vulnerability, the fact that it is on the border of the watershed does not draw too much concern for the fact that it is an area not examined in the later risk map. Being on the border of the watershed typically means that it is land that is more convex and higher than surrounding areas.

As such, despite having a higher vulnerability, its risk is likely less. In addition, it is not immediately next to a river, which also indicates a lower risk.

The southerly portion of the watershed is generally very low vulnerability, and except for the towns of Eslöv and Kävlinge, there are only two small areas that show moderate vulnerability elsewhere in the watershed. The low vulnerability is in a higher concentration in the northern side of the watershed, and moderate vulnerability appears to be evenly distributed but extremely seldom with the exception of the two towns and the area of interest. The section of river that is the area of interest is left on the map for reference in Figure 17.

3.5 Risk Map – Present-day High Rain Year

Multiplying the relative vulnerability map of the Kävlinge watershed and the hazard map modelling of flooding in the area of interest in 2006-2007 results in Figure 18. Notably, this led to no areas of severe relative risk but was kept in the legend for reference of the scale of risk.

The majority of areas are all under a relatively low risk, with occasional moderate risk and rare occurrences of major risk. When comparing this map to the hazard flood map of 2006-2007, the impact of the additional consideration of vulnerability into the equation makes a few things more obvious. Most importantly is the major relative risk in the area in the town of Kävlinge. Another interesting aspect is the moderate relative risk in the area close to Löddeköpinge when surrounding flooded areas have a low relative risk rating, which is a direct result of higher vulnerability in that area.

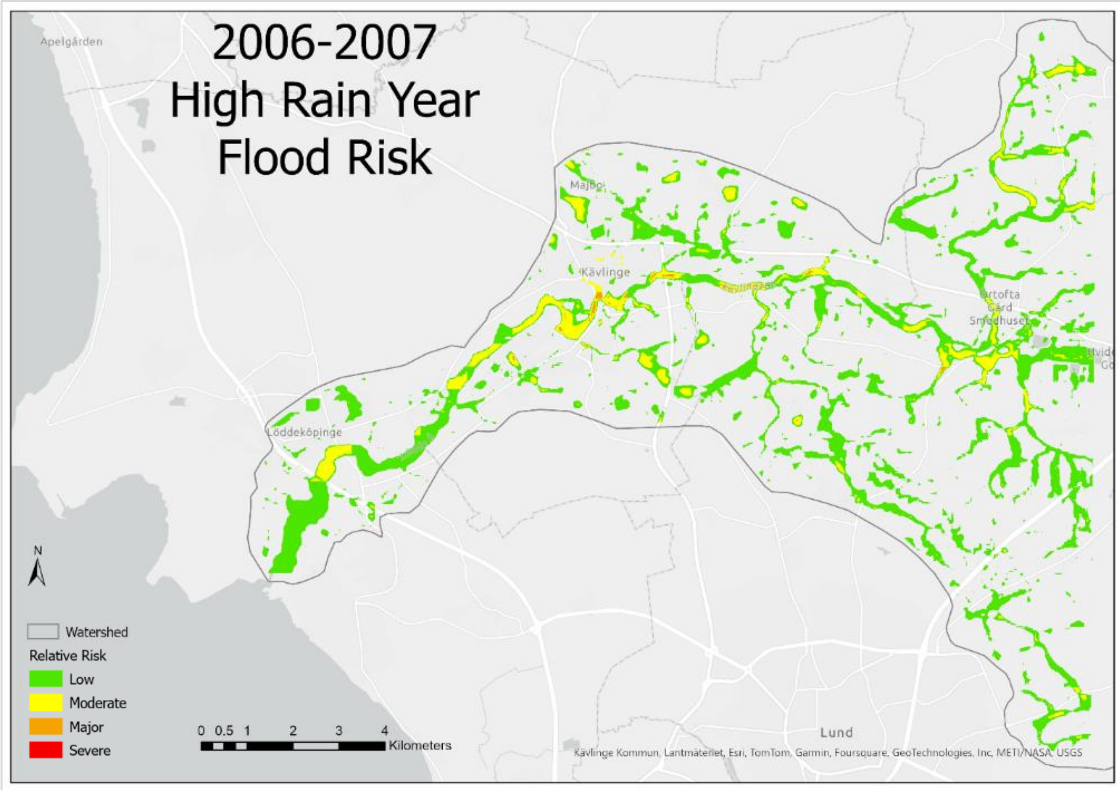

Figure 18: 2006-2007 High Rain Year Flood Risk
Calculated and displayed using ESRI's ArcGIS Pro using previously determined flood hazard and vulnerability. Flood hazard is peak flood height during the November 2006 – April 2007 period, the wettest period in historically hourly rainfall

In a detailed map of the result as presented in Figure 19, the moderate and major areas of risk are interesting. For example, the small areas of very low hazard flooding in the center of Kävlinge are of a moderate relative risk due to their placement in an area with many vulnerable factors and a high vulnerability rating. In addition, the flooded residential areas, particularly those to the east and west of the railroad and to the west are shown to have a major relative risk. Throughout the detailed map, including within the town of Kävlinge itself, the risk equation is shown to be an effective method of highlighting where to prioritize. Along the river, the addition of vulnerability rightly identifies regions that originally had high hazard but very low vulnerability as a low relative risk level, thanks to the green spaces in those areas. In addition, it highlights areas of concern to show where improvements should be considered and where future funding could benefit.

Figure 19: 2006-2007 High Rain Year Flood Risk Details
Calculated and displayed using ESRI's ArcGIS Pro using previously determined flood hazard and vulnerability. Flood hazard is peak flood height during the November 2006 – April 2007 period, the wettest period in historically hourly rainfall. Satellite imagery from ESRI's basemap collection.

3.6 Risk Map – RCP8.5 Scenario High Rain Year

The multiplication of the vulnerability map and the climate scenario hazard map provides a clear emphasis on how the risk will change in the future. In both the original risk map, shown in Figure 20 and the detailed risk map in Figure 21, the enlarged area of major and moderate risk is apparent. This enlargement of the higher risk areas is noticeable along the Kävlinge River.

This begins at the central eastern-most extent, where the moderate relative risk is much higher. Moving westward along the Kävlinge, there are not many more additional areas of moderate relative risk with the exception in the U-shaped bend in Kävlinge, which has a new moderate level risk to the north, close to commercial areas. However, in the middle stretch of this river segment, the amount of area that has changed to become a major relative risk is significant. Because changes in vulnerability over time are not predicted and the vulnerability portion remains a constant, this change is due to the deepening of the flooding and resulting in a higher hazard level. The increased area of major relative risk and the areas proximity to the town of Kävlinge has implications for future development and decision making of the town, considering the trajectory of the climate.

However, it should also be noted that in most areas, the risk for the climate scenario and 2006-2007 models are very similar. These similarities are in the areas farther from the river itself, and besides the widening of the low relative risk along the river, the central area of the river is where most of the changes occurred. A small detail that has potentially important ramifications is by the major road of Löddeköpinge. In the 2006-2007 model, the road is covered by a low relative risk level, however in the climate scenario, this changes to being completely covered by a moderate relative risk level. The change in hazard level over the road has largely impacted this major road, and this may be interesting for future renovation plans.

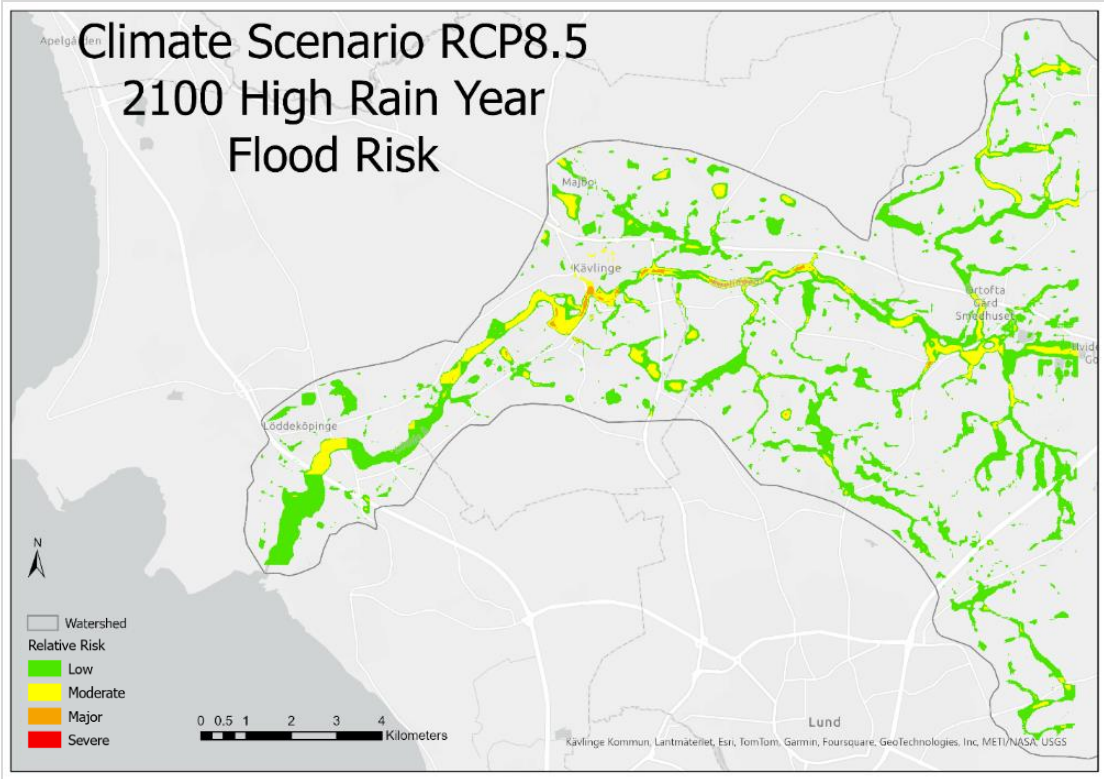

Figure 20: Climate Scenario RCP8.5 2100 High Rain Year Flood Risk
The risk is calculated and displayed using ESRI's ArcGIS Pro, and is representative of vulnerability and peak flood height during a 6-month high rain period in 2100 using the climate scenario RCP8.5.

Figure 21: Climate Scenario RCP8.5 2100 High Rain Year Flood Risk Details
The risk is calculated and displayed using ESRI's ArcGIS Pro and is representative of vulnerability and peak flood height during a 6-month high rain period in 2100 using the climate scenario RCP8.5. Satellite imagery is current, and from ESRI's basemap collection.

In a comparison of areas covered by different risk levels, as shown in Table 7, the patterns as described above are well summarized. The area differences between the 2006-2007 time period and the climate scenario in 2100 for a low risk level did not change enormously, by only 1.7%. The moderate risk level increased by a higher percentage, as seen in smaller areas such as the road close to Löddeköpinge and the U-shaped bend of the river close to the town of Kävlinge. Concerningly was the difference of change in the major risk level area, with a change of 54.7%. This reflects the importance of analyzing risk as a function of vulnerability and hazard, to better understand which areas need to be prioritized and to understand how the future climate may affect humans' safety and infrastructure.

Table 7: Differences in Present-Day and Future Risk Level Area Sizes

Risk Level	2006-2007 Area (m^2)	2100 Area (m^2)	Percent Increase
Low	17264900	17556100	1.7%
Moderate	3363500	3870200	15.1%
Major	11700	18100	54.7%

4. Discussion

There are several considerations to be discussed in relation to this study. These considerations include similarities with previous studies in the area, similar methodological studies, applications of the results, technical and theoretical limitations, and interesting potential methodological additions.

4.1 Previous Studies in the Area

This study's results are in line with other studies' findings of the hydrological and hydraulic nature within the Kävlinge Watershed. For example, two studies also examined the differences in the hydrology of the river in 2100 with the change of IPCC's RCP8.5 climate model using HEC-HMS. While there was no hydraulic analysis of the flooded area, but both found significantly increased discharge (Hu, 2022; Wicher, 2016). One of these papers, by Hu (2022), also used similar statistical methods (R^2, PBIAS, and peak error) for the calibration and validation process and had similarly well performing results (with the exclusion of Vombsjön, which Hu mentioned was not a worthwhile addition into the process due to its regulated flows and discrepancies between simulated and observed values). In the calibration process, both this study and Hu's study had nearly all statistics within the satisfactory bounds. Likewise, validation had some statistics outside of the satisfactory bounds, but this was still an acceptable performance of the model.

Another study of the area that was performed with both hydrological and hydraulic nature was conducted by Khadka et al. (2018) using HEC-HMS and HEC-RAS, which found similar results as in this study, in which there was not significant flooding outside of the normal defined flow route. Their results were compared to another a wild river in Nepal which is also in a relatively flat area, and it was clear that the Kävlinge did not have the same freedom to move and was more contained. Similarly, in this study the results reflected that the river did not flood out widely and stayed relatively contained within the river's flow route.

That the Kävlinge River typically stays within its flow path is seen in a few other governmental studies as well. This has been attributed to the fact that in the 1900's, the area was altered to funnel water through dedicated and robust waterway channels with a margin for flooding (Lunds Kommun and VA SYD, 2017). This was motivated by the desire for more agricultural area, and therefore reduced the wetland and flooding plain area to 1.5% of its original area.

The fact that the infrastructure and channel are well designed to account for flooding is also seen in an engineering study by MSB (2020). They used the MIKE 11 hydrodynamic modelling system to test 100 year and 200-year floods, and neither scenario lead to flooding over the bridge platform (however, one and two bridges respectively were touching the water flooding, which may lead to damage or blockages). However, they mentioned that a study of climate change adapted flows for 100- and 200-year floods would be of interest, considering that they are likely more severe and likely to impact the infrastructure (MSB, 2020). Specifically, they suggested using IPCC reports and models to do this future study, which is what this study has used. As seen in the results of in this study, the rainiest year in 2100 does appear to impact one of the bridges in Kävlinge, and the bridge in Löddeköpinge is in the very low hazard level in the present climate and increases to the low hazard level in the future climate. This suggests the need for future studies of the bridges to ensure that any needed preventative measures can be implemented, and to investigate the differences between the MSB (2020) study and this study.

A similar qualitative study by Baden and Davidsson in 2016 also found that infrastructure is not impacted. Looking at the specific river segment of interest, Baden and Davidsson have also found that in high flow periods, the Kävlinge does overflow into the agricultural areas leading up to the sea. This mirrors what was found in this study, with the largest flooded areas being the agricultural areas prior to the sea. The study also mentions that the waterways are generally well controlling of the peak flow periods, with not many areas of flooding, which is also what was determined by this study's hazard maps.

A further reason that the flooding has not been found to be very severe is the influence of infiltration and groundwater. Khadka et al. (2018) explained that the Kävlinge watershed has a high influence of groundwater within the hydrological system. The infiltration is also assumed to be a large influence due to the quantity or agricultural land and limited urban or paved areas (Lunds Kommun and VA SYD, 2017). This influence of groundwater and infiltration would explain some of the discrepancies in this study's imperfect statistic, as well as explain why the Manning's coefficient and infiltration layer have the relatively high corrective factors of +/- 40% after calibration, to take this into account. In addition, the fact that only one set of Manning's roughness coefficient values and one set of infiltration values for the watershed are used as the input into each model, while in reality these values change from season to season, year-to-year, and in relation to past weather conditions, also impacts the reliability of the results. However, all studies were similar in that they have used a set of values for the Manning's n and infiltration that were calibrated and validated generally, but not for separate instances or years.

Most studies did not mention any aspect of risk to the area or the populations, despite there being an impact on the agriculture of the area and the potential for impact on populations, as seen in this study. However, Lunds Kommun and VA SYD (2017) did emphasize the ecological importance of the watershed, and that this could be impacted by repeated or large flooding events. It is possible that there has not been a comprehensive flooding risk report due to previous reports stating the well-designed river channels. Due to the nature of climate change and changes in precipitation, this was a worthwhile confirmation that the river channels are equivalently effective in protecting the agricultural and vulnerable areas as it is currently. As seen in this paper, the river channels, while effective, are not perfect.

4.2 Similar Studies using HEC-RAS Rain-on-Grid

As a relatively new option to hydrological-hydraulic modelling, this study showed an overall good performance of HEC-RAS rain-on-grid after the calibration and validation procedure by using long-term time periods.

Many other studies have similarly successful results while looking at similar statistical measures of validation. For example, Zeiger and Hubbart's (2021) study in also used split-site calibration and had good performance metrics with an NSE of 0.33-0.92. R^2 of 0.86-0.97, and PBIAS of 10.4-33.8%. Other studies used a variety of statistical measures that differed from this study, such as Malik and Pal (2020) which used NSE (of 0.71) and RMSE, and Hariri et al. (2022) which had NSE (between 0.92-0.94), RMSE/SD, and water volume error. In comparison with the split sites validation values of this study, with most values between 0.5-0.98 for NSE, 0.5-0.71 for R^2, and 3.6-27.4% for PBIAS. This means that for the NSE values, compared to the other similar studies that used it, it is comparable to or better performing than all three studies that used NSE. Comparing this study to Zeiger and Hubbart (2021) for R^2 and PBIAS, this study had slightly lower performing metrics for R^2 and slightly better performing metrics for PBIAS.

Where many studies differed in methodologies was the use of event-based storm(s) to perform the calibration and validation process, where this study performed long-term periods (Ansori et al., 2024; Hariri et al., 2022; Malik and Pal, 2020; Nkeki et al., 2022; Zeiger and Hubbart, 2021). Interestingly, one study compared HEC-RAS rain-on-grid's validity with both particular storm events and long duration multi-peak time periods and was not able to validate the long duration time periods, whereas the model worked well for storm events (Godara et al., 2024). Although this is contradictory to what this study found, the terrain between the two studies are very different. Where the long-duration time period did not work, it was steep mountainous terrain in Norway, where in this study where the long-duration time period use was validated, it was on flat agricultural area in southern Sweden. Using HEC-RAS rain-on-grid for specific events may be controversial, considering that one study found that the parameters in the calibration stages must be recalibrated for each event, potentially due to changing infiltration values in relation to previous weather conditions that vary from event to event (Ginting et al., 2023). Perhaps, when possible, long time periods allow for a more accurate calibration outside of specific events and provide parameters that can be used more universally.

Methodologies also range between papers, showing potential applicability of HEC-RAS rain-on-grid. For example, calibration was done with historical reports (Nkeki et al., 2022), observed hydrographs (Zeiger and Hubbart, 2021), synthetic hydrographs (Ennouini et al., 2024), flooding extent (Hariri et al., 2022), and limited gauge height data (Malik and Pal, 2020). This study used gauge discharge flows and comparatively was very data rich, temporally because it was every hour for an extended period of time and spatially because it was possible to perform a split-site calibration. Because the data input into calibration is rich, this likely increases the validity and applicability of the results of this study.

Two HEC-RAS rain-on-grid studies have used the results to perform risk analyses. Similar to this study, Nkeki et al. (2022) looked at building, road, and rail density as vulnerabilities and flood hazard area. While this area in Sweden has well-structured waterways and small areas of typically relatively low vulnerability, the Ona River Basin in Nigeria has high levels of hazard and high levels of vulnerability, and it was found that 48.2% of the overall basin is at moderate risk or above, whereas in this study the area of moderate risk or above is very small. Another study also used the HEC-RAS result to make hazard maps, but also incorporated flow velocity with water depth (Ennouini et al., 2024). The methodology also differed in respects to the vulnerability and risk, because vulnerability was only considering buildings, and the quantity of risk was a categorization of building damages in euros. This thinking that risk and vulnerability are only associated with buildings would not provide a holistic view of overall vulnerability of a human population in that given area, considering that building infrastructure is not the sole determinant of the health or economy of the people who live there.

4.3 Applications of the Results

Risk assessments have useful applications for informing decision makers, budget planning, civil engineering, and storm preparedness. Despite limitations, on a local level for planning, this can be an incredible tool to help establish and evaluate current and future policies to minimize potential risk (Gain et al., 2015). In addition to policies, risk assessments are also a powerful tool to simulate engineering advancements, and therefore this study or the methodology of this study may be helpful in future advancements that can take climate change into account as well (Abdessamed and Abderrazark, 2019).

To maximize risk assessments' efficacy, it is recommended that local populations are informed and listened to because their inclusion has shown to further reduce risk (Tran et al., 2008). Using this study in joint with locals would multiply positive benefits, such as addressing and finding solutions for at-risk commercial, residential, and transportation infrastructure. A potential fix may be improved river management, including transferring more at-risk areas into space for the Kävlinge River to meander more freely, which would benefit the area ecologically and economically due to fewer or no vulnerabilities (Buffin-Bélanger et al., 2015). Due to costs, this is perhaps suitable as a long-term goal.

Beyond informing decisions made in the study's area of interest, this study could also be used as a blueprint for future studies. This is particularly useful thanks to HEC-RAS rain-on-grid's simplicity in parameters, combined concurrent hydraulic and hydrologic model, minimized error, and uncomplex data requirements (Kalra et al., 2023; Zeiger and Hubbart, 2021).

4.4 Limitations of this Study

There are several limitations of this study, namely due to necessary limitations due to time. A model such as this can always be improved to achieve a result closer to perfection, but it is a function of time that controls how many considerations can be reasonably taken into account. Some of the considerations that had to be passed over for timing's sake were related to the HEC-RAS rain-on-grid model and the vulnerability methods.

Improving and expanding inputs into the HEC-RAS rain-on-grid model would be beneficial. For example, there is an option in the HEC-RAS unsteady flow setup that allows the person to input temperature, wind, and pressure into the "Global Boundaries" function. However, this multiplies the amount of data preparation and input. In addition, there are limited resources to understand to what degree this improves the accuracy of the model. It is important to consider what impact including more inputs such as temperature, wind speed, wind direction, and pressure may have on the results.

In addition, groundwater, snowmelt, sediment, and regulated flows (dams) impact the real water flow volumes and flooding models of the Kävlinge River. However, in this study these could not be considered in the model. However, groundwater in this area has been remarked to be an important contributor to the river flow, and there are several dams along the Kävlinge River that regulate water flow (Khadka et al., 2018)

One of the HEC-RAS rain-on-grid layers that can impact the results is the grid size (Costabile et al., 2021). One benchmark HEC-RAS rain-on-grid study tested different mash sizes, with the largest being 30 meters by 30 meters (David and Schmalz, 2021). In this case, a compromise was made because of the relatively large watershed size and the fact that even with a mesh grid size of 40 meters by 40 meters, the computation time for each model simulation was between 43- 52 hours.

Improving or including these aspects would likely improve the model. For example, it would make the simulated flow more accurate and precise, and therefore would decrease the differences between the simulated and observed values, resulting in improved calibration and validation statistics. Current differences in the simulated flow and observed flow may be explained by these factors.

Additional limitations are within the vulnerability portion, such as determining the best resolution to perform the vulnerability. An extremely small cellular size might lead to too much detail (for example, there is only one school per cell, the cells draw the roads, etc. Instead of a generalized map of vulnerability, it might appear to be more of a landmark map. Grids that are too large may not provide enough detail (if the entire study area was made up of just 3 grid cells, it would be more difficult to draw conclusions of where to focus efforts). In this study, a grid cell size was determined to attempt to be an effective medium between these two exaggerated cases. However, ideal grid size for the vulnerability analysis could be tested out and determined given more time. It is likely a relative optimization that does not translate well to other papers with other vulnerabilities and scales.

Another aspect of vulnerability that might be improved is sub-weighting within the weighted factors. An example of this may be weighing larger roads more heavily than size streets that are used by remote residents. Of course, larger roads that are used by many people to travel long distances, such as in instances of evacuations, should be rated as more important than farming side-roads.

Vulnerability itself is also a very subjective concept and differs regionally and topically. This is typically addressed in other papers by bringing in other scientific experts and having them rate the vulnerability factors' importance. Due to time and resources, this was performed as best as possible using other papers' rankings that were determined by experts (for example, two papers identified people over 60 as a fragile population, while this may be a disputed idea, especially regionally). Including experts of this region and who understand flooding vulnerability would improve the vulnerability portion.

Another subjectivity is the overall idea of risk and disaster and the limitation of scale. When comparing impacts of flooding for a small area of the watershed due to localized weather patterns to world-wide events such as mass extinctions, identifying flooding as a "severe" risk level is very relative (Wisner et al., 1994). To address this, the term "relative" is used often for risk and vulnerability.

Related to this, identifying 1 meter of water as a very low flood hazard level may seem reasonable compared to deeper levels of flooding. But, on a small neighborhood scale, 1 meter of flooding can flood houses, destroy infrastructure and belongings, creates a need for evacuation, and presents a very severe hazard for small children. For these people, this would not feel like a "very low flood hazard level". However, this paper had to accept a certain level of subjectivity and addressed this by following previous studies' methodologies and viewing flooding generally and relatively.

4.5 Potential Methodological Additions

Addressing the potential improvements related to the limitations discussed above keeps the general methodology of this paper intact. However, there are several interesting potential additions to the methodology that were tempting to include, but due to lack of time, they could not be incorporated. This included performing an entire watershed analysis, a flood frequency analysis or precipitation analysis, adding other factors into hazard calculation, calibration and validation using satellite imagery, and adding future vulnerability predictions.

When originally selecting the area of focus for this study, an aerial image of the area was visually examined, and the last segment of the river appeared to be the most interesting because it seemed to be the most vulnerable due to proximity of infrastructure and the river. However, during the vulnerability calculation of the overall watershed, it was found that the Eslöv area would have been interesting, along with other areas that had moderate vulnerability along the rivers. In addition, it might be possible to see a relationship with low vulnerability in the south of the watershed and increased flooding, to examine if flooding was already regular or severe enough that populations took this into account. To examine the entire watershed in detail, it would be necessary to perform a tiling function in ArcGIS Pro.

A flood frequency analysis or a precipitation analysis with an intensity-duration-frequency aspect would be interesting to model specific events, such as a 100-year flood or 200-year rainstorm. This takes historical data and applies it to an optimal statistical distribution, which provides predicted quantities of river flow or precipitation. A study that examines a specific event or events would replace the simple “high rain year” and is an improvement because it quantifies the return period and size. Therefore, there are more reliable implications for planning purposes and civic engineering projects. Another interesting aspect of the event-based model is looking at peak rain and not a long-term rainy period that spreads out the rain over time. The long-term method was used in this study because of the fact that a high peak of precipitation does not guarantee a high peak of flow, and long periods of rain can create high peaks of flow as well (Vangelis et al., 2022). If the peak rain method was used, it would be necessary to do an initial analysis of the start-up conditions prior to the rain event. In addition, it would be difficult to run a scenario of one rain event and assume it is a representative hyetograph (like a hydrograph, but of quantity of precipitation over time) of most rain events, and as such would require additional analyses.

Adding other factors into the hazard calculation has been done by other papers as well, as seen in Table 1. While using only flood depth is one standard of hazard calculation, other papers have taken aspects such as flow velocity as well. Flooding of 1 meter of standing water is much less dangerous and destructive than flooding of 1 meter of powerful, rushing water. As such, this would improve the hazard map and therefore the risk map as well. Another factor that might be interesting to take into the hazard calculation for the Kävlinge River, particularly in this study’s focus area is impacts of coastal storm surges or tidal impacts of flooding on the river (Zhong et al., 2024). This is relevant given the unruly North Sea, increased precipitation corresponding with storm surges, sea level rise due to climate change, and the inevitable combination of all three (Pasquier et al., 2019). Conveniently, HEC-RAS is capable of taking this into account using mixed flow, where it can take tidal flow into consideration (Suriya and Mudgal, 2012; Zhong et al., 2024).

During the literature review and data collection phase of this study, one of the initial goals was to use observed flooded area to perform the calibration and validation. This paper uses flooded area to determine hazard but uses volume through a checkpoint to confirm that the model is correct. In theory it is possible that the model’s discharge is correct but does not distribute the flooded waters correctly. As such, this paper would be improved if flooded area is used to calibrate and validate. It is not always possible to have observed flooded areas as a resource. For this study, the observed flooded area was searched for in the European Union databases and in satellite imagery. Unluckily, it was not found in European Union databases for specific events, and satellite imagery was always taken too late during a flooding episode or was too corrupted to be used for the calibration and validation process. Future flooding and well-timed satellite imagery might be useful to improve the calibration and validation process in later studies.

This study nearly surely incorrectly assumes no change in vulnerability factors between current and future demographics and infrastructures. Including an additional vulnerability analysis for future conditions would be a worthwhile addition. For example, the future vulnerability analysis could make use 0f the dataset by Li et al. (2021) which predicts urban land areas in 2100. Other prediction datasets for demographics, land cover, and other potential vulnerability factors could be combined for a more comprehensive future risk assessment. The urban areas layer could also be used to augment the infiltration and Manning's roughness coefficient layers in HEC-RAS, which would anticipate future flooding even better because of the negative impact that urban area has on flooding extent, velocity, and timing (Devi et al., 2019; Oumaima et al., 2019; Sholichin and Qadri, 2020; Suriya and Mudgal, 2012; Zope et al., 2014).

5. Conclusions

The objectives of this study, meant to be informative for planning for present and future flooding, accomplished all objectives originally sought out. The HEC-RAS rain-on-grid was shown to be an effective and simple model to predict flooding along the Kävlinge River, and resulted in good calibration and validation performance metric values according to the commonly used NSE, R^2, and PBIAS standards. The satisfactory NSE values were between 0.98-0.5, R^2 values ranged form 0.75-0.46, and PBIAS values from 3.6-29.8%, though there an occasional outlier in the validation phase. This ensured that the resulting flooding extents and depths would be a reliable output to use as hazard maps. Both the present-day (2006-2007) and future climate (year 2100) showed relatively similar results, with hazardous areas in the town of Kävlinge and along the Kävlinge river in the last 23.6 kilometers. Other hazardous areas with lighter flooding were mostly agricultural. However, the future climate scenario model showed a slight increase in overall hazardous areas, and demonstrated that within the flooded areas, the depth will increase and therefore be more hazardous. This was especially true close to, within, and upstream of the town of Kävlinge. The vulnerability portion that provided relative vulnerability within the watershed, revealed very high but concentrated vulnerability outside of the study's focus area, and has implications for future studies. Though, the second most vulnerable area was within the study's concentration, and the elevated vulnerability was also more dispersed throughout the study's focus. As such, the focus area selected was confirmed to be an area of concern which requires an effective risk assessment. Within the focus area, the most vulnerable area was the town of Kävlinge.

The combination of the present-day and future climate hazard maps with vulnerability each then calculated the risk map of flooding. This proved that the combination of the vulnerable town of Kävlinge and the more hazardous conditions in that area leads to an overall higher risk and therefore should be monitored for future improvements. In addition, this highlighted another area of elevated risk close to the town of Löddeköpinge. The risk map also provided evidence that the relative risk is not severe in the study's area, and that the area is generally well adapted for the given levels of hazard.

While there are some limitations to the study and potential for fine-tuning individual aspects, the study accomplished the objectives effectively. The results have potential uses for the planning of projects, infrastructure, budgets, and policies. Particularly pertinent is the ability to plan in advance for future flooding, which has been proven to be more severe due to the changing climate.

6. References

Abdessamed, D., & Abderrazak, B. (2019). Coupling HEC-RAS and HEC-HMS in rainfall–runoff modeling and evaluating floodplain inundation maps in arid environments: Case study of Ain Sefra city, Ksour Mountain. SW of Algeria. *Environmental Earth Sciences*, *78*(19). https://doi.org/10.1007/s12665-019-8604-6

Adger, W. N. (2006). Vulnerability. *Global Environmental Change*, *16*(3), 268–281. https://doi.org/10.1016/j.gloenvcha.2006.02.006

Aksha, S. K., Resler, L. M., Juran, L., & Carstensen, L. W., Jr. (2020). A geospatial analysis of multi-hazard risk in Dharan, Nepal. *Geomatics, Natural Hazards and Risk*, *11*(1), 88–111. https://doi.org/10.1080/19475705.2019.1710580

Alamanos, A., Papaioannou, G., Varlas, G., Markogianni, V., Papadopoulos, A., & Dimitriou, E. (2024). Representation of a post-fire flash-flood event combining meteorological simulations, remote sensing, and hydraulic modeling. *Land*, *13*(1), 47. https://doi.org/10.3390/land13010047

Alfieri, L., Burek, P., Feyen, L., & Forzieri, G. (2015). Global warming increases the frequency of river floods in Europe. *Hydrology and Earth System Sciences*, *19*(5), 2247–2260. https://doi.org/10.5194/hess-19-2247-2015

Alfieri, L., Feyen, L., Dottori, F., & Bianchi, A. (2015). Ensemble flood risk assessment in Europe under high end climate scenarios. *Global Environmental Change*, *35*, 199–212. https://doi.org/10.1016/j.gloenvcha.2015.09.004

Anandhi, A., Srinivas, V. V., Nanjundiah, R. S., & Nagesh Kumar, D. (2008). Downscaling precipitation to river basin in India for IPCC SRES scenarios using support vector machine. *International Journal of Climatology*, *28*(3), 401–420. https://doi.org/10.1002/joc.1529

Ansori, M. B., Lasminto, U., & Gde Kartika, A. A. (2023). Reliability of Runoff Hydrograph Model for Extreme Rainfall Events using HEC-RAS 2D Flow Hydrodynamics Rain-On-Grid. *IOP Conference Series: Earth and Environmental Science*, *1276*(1), 012034. https://doi.org/10.1088/1755-1315/1276/1/012034

Ansori, M. B., Lasminto, U., & Kartika, A. A. G. (2024). Runoff hydrograph analysis of HEC-RAS 2D flow hydrodynamics meteorological rain-on-grid on observed watershed: A case study of Wiroko Sub-watershed. *International Journal on Advanced Science, Engineering and Information Technology*, *14*(2), 575–581. https://doi.org/10.18517/ijaseit.14.2.19813

Apel, H., Aronica, G. T., Kreibich, H., & Thieken, A. H. (2008). Flood risk analyses—how detailed do we need to be? *Natural Hazards*, *49*(1), 79–98. https://doi.org/10.1007/s11069-008-9277-8

Apel, H., Thieken, A. H., Merz, B., & Blöschl, G. (2004). Flood risk assessment and associated uncertainty. *Natural Hazards and Earth System Sciences*, *4*(2), 295–308. https://doi.org/10.5194/nhess-4-295-2004

Asante, K. O., Artan, G. A., Pervez, S., Bandaragoda, C., & Verdin, J. P. (2008). Technical Manual for the Geospatial Stream Flow Model (GeoSFM). *U.S. Geological Survey Open-File Report 2007–1441*. U.S. Geological Survey; U.S. Department of the Interior. https://pubs.usgs.gov/of/2007/1441/pdf/ofr2008-1441.pdf

Baden, E., & Davidsson, T. (2016). Höga och låga vattenflöden i vattendrag i Kävlingeåns avrinningsområde [High and low water flows in watercourses in the Kävlingeån catchment area]. In K. Holmström (Ed.), *https://kavlingean.se/rapporter/Floedesrapport_ver_september20160928.pdf*.

Bates, P. D., Horritt, M. S., Aronica, G., & Beven, K. (2004). Bayesian updating of flood inundation likelihoods conditioned on flood extent data. *Hydrological Processes*, *18*(17), 3347–3370. https://doi.org/10.1002/hyp.1499

Benito, G., Díez-Herrero, A., & Fernández de Villalta, M. (2004). Flood response to solar activity in the Tagus Basin (central Spain) over the last millennium. *Climatic Change*, *66*(1/2), 27–28. https://doi.org/10.1023/b:clim.0000043334.30365.e0

Bennett, N. D., Croke, B. F. W., Guariso, G., Guillaume, J. H. A., Hamilton, S. H., Jakeman, A. J., Marsili-Libelli, S., Newham, L. T. H., Norton, J. P., Perrin, C., Pierce, S. A., Robson, B., Seppelt, R., Voinov, A. A., Fath, B. D., & Andreassian, V. (2013). Characterising performance of environmental models. *Environmental Modelling & Software*, *40*, 1–20. https://doi.org/10.1016/j.envsoft.2012.09.011

Blaikie, P. M., Cannon, T., Davis, I., & Wisner, B. (1994). *At risk: Natural hazards, people's vulnerability, and disasters*. Routledge.

Bolin, R., & Klenow, D. J. (1983). Response of the elderly to disaster: An age-stratified analysis. *The International Journal of Aging and Human Development*, *16*(4), 283–296. https://doi.org/10.2190/mqeg-yn39-8d5v-wkmp

Bronselaer, B., Winton, M., Griffies, S. M., Hurlin, W. J., Rodgers, K. B., Sergienko, O. V., Stouffer, R. J., & Russell, J. L. (2018). Change in future climate due to Antarctic meltwater. *Nature*, *564*(7734), 53–58. https://doi.org/10.1038/s41586-018-0712-z

Brunner, G. (2022). *Diffusion Wave vs Full Momentum (SWE)*. Hydrologic Engineering Center. https://www.hec.usace.army.mil/confluence/rasdocs/rastraining/files/latest/183111063/183111162/1/1709778222434/2.5+L-Diff-vs-FEQ.pdf

Buffin-Bélanger, T., Biron, P. M., Larocque, M., Demers, S., Olsen, T., Choné, G., Ouellet, M.-A., Cloutier, C.-A., Desjarlais, C., & Eyquem, J. (2015). Freedom space for rivers: An economically viable river management concept in a changing climate. *Geomorphology*, *251*, 137–148. https://doi.org/10.1016/j.geomorph.2015.05.013

Cardona, O.-D., van Aalst, M. K., Birkmann, J., Fordham, M., McGregor, G., Perez, R., Pulwarty, R. S., Schipper, E. L. F., & Sinh, B. T. (2012). Determinants of Risk: Exposure and Vulnerability. In *Managing the Risks of Extreme Events and Disasters to Advance Climate Change Adaptation*. Cambridge University Press.

Casas, A., Benito, G., Thorndycraft, V. R., & Rico, M. (2006). The topographic data source of digital terrain models as a key element in the accuracy of hydraulic flood modelling. *Earth Surface Processes and Landforms*, *31*(4), 444–456. https://doi.org/10.1002/esp.1278

Chakraborty, S., & Mukhopadhyay, S. (2019). Assessing flood risk using analytical hierarchy process (AHP) and geographical information system (GIS): Application in Coochbehar district of West Bengal, India. *Natural Hazards*, *99*(1), 247–274. https://doi.org/10.1007/s11069-019-03737-7

Chang, H., Lafrenz, M., Jung, I.-W., Figliozzi, M., Platman, D., & Pederson, C. (2010). Potential impacts of climate change on flood-induced travel disruptions: A case study of Portland, Oregon, USA. *Annals of the Association of American Geographers*, *100*(4), 938–952. https://doi.org/10.1080/00045608.2010.497110

Clark, G. E., Moser, S. C., Ratick, S. J., Dow, K., Meyer, W. B., Emani, S., Jin, W., Kasperson, J. X., Kasperson, R. E., & Schwarz, H. E. (1998). Assessing the Vulnerability of Coastal Communities to Extreme Storms: The case of Revere, MA., USA. *Mitigation and Adaptation Strategies for Global Change*, *3*(1), 59–82. https://doi.org/10.1023/a:1009609710795

Cook, A., & Merwade, V. (2009). Effect of topographic data, geometric configuration and modeling approach on flood inundation mapping. *Journal of Hydrology*, *377*(1–2), 131–142. https://doi.org/10.1016/j.jhydrol.2009.08.015

Costabile, P., Costanzo, C., Ferraro, D., & Barca, P. (2021). Is HEC-RAS 2D accurate enough for storm-event hazard assessment? Lessons learnt from a benchmarking study based on rain-on-grid modelling. *Journal of Hydrology*, *603*(2), 126962. https://doi.org/10.1016/j.jhydrol.2021.126962

Costabile, P., Costanzo, C., Ferraro, D., Macchione, F., & Petaccia, G. (2020). Performances of the new HEC-RAS version 5 for 2-D hydrodynamic-based rainfall-runoff simulations at basin scale: Comparison with a state-of-the art model. *Water*, *12*(9), 2326. https://doi.org/10.3390/w12092326

Cutter, S. L., Barnes, L., Berry, M., Burton, C., Evans, E., Tate, E., & Webb, J. (2008). A place-based model for understanding community resilience to natural disasters. *Global Environmental Change*, *18*(4), 598–606. https://doi.org/10.1016/j.gloenvcha.2008.07.013

Dang, N. M., Babel, M. S., & Luong, H. T. (2010). Evaluation of food risk parameters in the Day River Flood Diversion Area, Red River Delta, Vietnam. *Natural Hazards*, *56*(1), 169–194. https://doi.org/10.1007/s11069-010-9558-x

Danumah, J. H., Odai, S. N., Saley, B. M., Szarzynski, J., Thiel, M., Kwaku, A., Kouame, F. K., & Akpa, L. Y. (2016). Flood risk assessment and mapping in Abidjan district using multi-criteria analysis (AHP) model and geoinformation techniques, (cote d'ivoire). *Geoenvironmental Disasters*, *3*(1). https://doi.org/10.1186/s40677-016-0044-y

Darabi, H., Choubin, B., Rahmati, O., Torabi Haghighi, A., Pradhan, B., & Kløve, B. (2019). Urban flood risk mapping using the GARP and QUEST models: A comparative study of machine learning techniques. *Journal of Hydrology*, *569*, 142–154. https://doi.org/10.1016/j.jhydrol.2018.12.002

David, A., & Schmalz, B. (2021). A systematic analysis of the interaction between rain-on-grid-simulations and spatial resolution in 2D hydrodynamic modeling. *Water*, *13*(17), 2346. https://doi.org/10.3390/w13172346

de Brito, M. M., & Evers, M. (2016). Multi-criteria decision-making for flood risk management: A survey of the current state of the art. *Natural Hazards and Earth System Sciences*, *16*(4), 1019–1033. https://doi.org/10.5194/nhess-16-1019-2016

Devi, N. N., Sridharan, B., & Kuiry, S. N. (2019). Impact of urban sprawl on future flooding in Chennai city, India. *Journal of Hydrology*, *574*, 486–496. https://doi.org/10.1016/j.jhydrol.2019.04.041

Easterling, D. R., Evans, J. L., Groisman, P. Y., Karl, T. R., Kunkel, K. E., & Ambenje, P. (2000). Observed variability and trends in extreme climate events: A brief review. *Bulletin of the American Meteorological Society*, *81*(3), 417–425. https://doi.org/10.1175/1520-0477(2000)081<0417:ovatie>2.3.co;2

Easterling, D. R., Meehl, G. A., Parmesan, C., Changnon, S. A., Karl, T. R., & Mearns, L. O. (2000). Climate extremes: Observations, modeling, and impacts. *Science*, *289*(5487), 2068–2074. https://doi.org/10.1126/science.289.5487.2068

Edamo, M. L., Hatiye, S. D., Minda, T. T., & Ukumo, T. Y. (2023). Flood inundation and risk mapping under climate change scenarios in the lower Bilate catchment, Ethiopia. *Natural Hazards*, *118*(3), 2199–2226. https://doi.org/10.1007/s11069-023-06101-y

Ennouini, W., Fenocchi, A., Petaccia, G., Persi, E., & Sibilla, S. (2024). A complete methodology to assess hydraulic risk in small ungauged catchments based on HEC-RAS 2D Rain-On-Grid simulations. *Natural Hazards*. https://doi.org/10.1007/s11069-024-06515-2

Gain, A. K., Mojtahed, V., Biscaro, C., Balbi, S., & Giupponi, C. (2015). An integrated approach of flood risk assessment in the eastern part of Dhaka City. *Natural Hazards*, *79*(3), 1499–1530. https://doi.org/10.1007/s11069-015-1911-7

Ghosh, A., & Kar, S. K. (2018). Application of analytical hierarchy process (AHP) for flood risk assessment: A case study in Malda district of West Bengal, India. *Natural Hazards*, *94*(1), 349–368. https://doi.org/10.1007/s11069-018-3392-y

Ginting, B. M., Lidyana, P., Christopher, C., Yudianto, D., & Yuebo, X. (2023). Comparison of flood hydrograph prediction between synthetic unit hydrograph methods and rain-on-grid model for Katulampa watershed, Indonesia. *Acta Hydrotechnica*, 81–94. https://doi.org/10.15292/acta.hydro.2023.05

Ginting, B. M., Lidyana, P., Christopher, C., Yudianto, D., & Yuebo, X. (2024). Evaluating the satellite-derived DEM accuracy with rain-on-grid modeling for flood hydrograph prediction of Katulampa Watershed, Indonesia. *International Journal of River Basin Management*, 1–18. https://doi.org/10.1080/15715124.2024.2312857

Godara, N., Bruland, O., & Alfredsen, K. (2024). Comparison of two hydrodynamic models for their rain-on-grid technique to simulate flash floods in steep catchment. *Frontiers in Water*, *6*. https://doi.org/10.3389/frwa.2024.1384205

Guerreiro, S. B., Dawson, R. J., Kilsby, C., Lewis, E., & Ford, A. (2018). Future heat-waves, droughts and floods in 571 European cities. *Environmental Research Letters*, *13*(3), 034009. https://doi.org/10.1088/1748-9326/aaaad3

Gustafsson, M., Rayner, D., & Chen, D. (2010). Extreme rainfall events in southern Sweden: Where does the moisture come from? *Tellus A*, *62A*(5). https://doi.org/10.3402/tellusa.v62i5.15715

Hariri, S., Weill, S., Gustedt, J., & Charpentier, I. (2022). A balanced watershed decomposition method for rain-on-grid simulations in HEC-RAS. *Journal of Hydroinformatics*, *24*(2), 315–332. https://doi.org/10.2166/hydro.2022.078

Hoque, M. A.-A., Phinn, S., Roelfsema, C., & Childs, I. (2017). Cyclone disaster mapping, monitoring and management using satellite remote sensing and spatial analysis. *International Journal of Disaster Risk Reduction*, *22*. https://doi.org/10.14264/uql.2017.908

Horritt, M. S., & Bates, P. D. (2002). Evaluation of 1D and 2D numerical models for predicting river flood inundation. *Journal of Hydrology*, *268*(1–4), 87–99. https://doi.org/10.1016/s0022-1694(02)00121-x

Hu, W. (2022). *Combining continuous and event-based hydrological modeling in Kävlinge River Basin with HEC-HMS*. LUP Student Papers; Lund University. http://lup.lub.lu.se/student-papers/record/9087504

Humanitarian OpenStreetMap Team. (n.d.). *Humanitarian OpenStreetMap Team Export Tool*. Retrieved May 13, 2024, from https://export.hotosm.org/v3/

Hydrologic Engineering Center. (n.d.-a). *HEC-HMS Tutorials and Guides*. Retrieved June 23, 2024, from https://www.hec.usace.army.mil/confluence/hmsdocs/hmsguides

Hydrologic Engineering Center. (n.d.-b). *HEC-RAS 2D User's Manual*. Retrieved February 28, 2024, from https://www.hec.usace.army.mil/confluence/rasdocs/r2dum/latest

Intergovernmental Panel on Climate Change. (n.d.). *Climate change widespread, rapid, and intensifying*. Retrieved June 23, 2024, from https://www.ipcc.ch/2021/08/09/ar6-wg1-20210809-pr

Intergovernmental Panel on Climate Change. (1992). *IPCC IS92 Scenarios*. https://sedac.ciesin.columbia.edu/ddc/is92/index.html

Jena, R., & Pradhan, B. (2020). Integrated ANN-cross-validation and AHP-TOPSIS model to improve earthquake risk assessment. *International Journal of Disaster Risk Reduction*, *50*, 101723. https://doi.org/10.1016/j.ijdrr.2020.101723

Kalra, A., Thakur, B., Aryal, A., & Gupta, R. (2023). A 2D rain-on-mesh model for simultaneous hydrologic and hydraulic computation. *World Environmental and Water Resources Congress 2023*. http://dx.doi.org/10.1061/9780784484852.057

Khadka, J., Bhaukajee, J., Zhang, L., & Frisk, M. (2018). *Using HEC-HMS and HEC-RAS models for rainfall-runoff simulation and flood inundation mapping: Case studies from Nepal and Sweden*. *2018*. Abstract from AGU (American Geophysical Union) Fall Meeting, 2018, Washington, United States.

Klokan Technologies GmbH. (2021). *SWEREF99 TM*. EPSG. https://epsg.io/3006

Knebl, M. R., Yang, Z.-L., Hutchison, K., & Maidment, D. R. (2005). Regional scale flood modeling using NEXRAD rainfall, GIS, and HEC-HMS/RAS: A case study for the San Antonio River Basin Summer 2002 storm event. *Journal of Environmental Management*, *75*(4), 325–336. https://doi.org/10.1016/j.jenvman.2004.11.024

Länsstyrelsernas Geodatakatalog. (n.d.). Retrieved May 13, 2024, from https://ext-geodatakatalog.lansstyrelsen.se/GeodataKatalogen/srv/swe/catalog.search#/home

Lantmateriet. (n.d.-a). *Geodataprodukter [Geodata products]*. Retrieved January 11, 2024, from https://geotorget.lantmateriet.se/geodataprodukter

Lantmateriet. (n.d.-b). *SWEREF 99, projections*. Retrieved January 9, 2024, from https://www.lantmateriet.se/en/geodata/gps-geodesi-och-swepos/reference-systems/two-dimensional-systems/SWEREF-99-projektioner/#anchor-0

Li, X., Zhou, Y., Hejazi, M., Wise, M., Vernon, C., Iyer, G., & Chen, W. (2021). Global urban growth between 1870 and 2100 from integrated high resolution mapped data and urban dynamic modeling. *Communications Earth & Environment*, *2*(1). https://doi.org/10.1038/s43247-021-00273-w

Lind, P., & Kjellström, E. (2008). *Temperature and precipitation changes in Sweden, a wide range of model-based projections for the 21st century*. https://www.smhi.se/polopoly_fs/1.3297!/RMK113_rapport_090421.pdf

Lunds Kommun, & VA SYD. (2017). *Sjö- Och Vattendragsplan [Lake and watercourse plan]*.

https://lund.se/download/18.402bf0b018388c67fde1411d/1666247759597/Sj%C3%B6-%20och%20vattendragsplan%20Lunds%20kommun.pdf

Maingi, J. K., & Marsh, S. E. (2002). Quantifying hydrologic impacts following dam construction along the Tana River, Kenya. *Journal of Arid Environments*, *50*(1), 53–79. https://doi.org/10.1006/jare.2000.0860

Malik, S., & Pal, S. C. (2020). Application of 2D numerical simulation for rating curve development and inundation area mapping: A case study of monsoon dominated Dwarkeswar river. *International Journal of River Basin Management*, *19*(4), 553–563. https://doi.org/10.1080/15715124.2020.1738447

Malik, S., & Pal, S. C. (2021). Potential flood frequency analysis and susceptibility mapping using CMIP5 of MIROC5 and HEC-RAS model: A case study of lower Dwarkeswar River, Eastern India. *SN Applied Sciences*, *3*(1). https://doi.org/10.1007/s42452-020-04104-z

Maneta, M. P., Pasternack, G. B., Wallender, W. W., Jetten, V., & Schnabel, S. (2007). Temporal instability of parameters in an event-based distributed hydrologic model applied to a small semiarid catchment. *Journal of Hydrology*, *341*(3–4), 207–221. https://doi.org/10.1016/j.jhydrol.2007.05.010

Mani Murali, R., Ankita, M., Amrita, S., & Vethamony, P. (2013). Coastal vulnerability assessment of Puducherry coast, India, using the analytical hierarchical process. *Natural Hazards and Earth System Sciences*, *13*(12), 3291–3311. https://doi.org/10.5194/nhess-13-3291-2013

Maskrey, A. (1989). *Disaster mitigation: A community based approach*. Oxfam Publications.

Masood, M., & Takeuchi, K. (2011). Assessment of flood hazard, vulnerability and risk of mid-eastern Dhaka using DEM and 1D hydrodynamic model. *Natural Hazards*, *61*(2), 757–770. https://doi.org/10.1007/s11069-011-0060-x

Mazarei, R., Mohammadi, A. S., Ebrahimian, H., & Naseri, A. A. (2021). Temporal variability of infiltration and roughness coefficients and furrow irrigation performance under different inflow rates. *Agricultural Water Management*, *245*, 106465. https://doi.org/10.1016/j.agwat.2020.106465

Merwade, V. (n.d.). *Creating CN Grid in QGIS from NLCD Landuse and SSURGO Soil data*. Lyles School of Civil Engineering, Purdue University. https://web.ics.purdue.edu/~vmerwade/education/qcngrid.pdf

Mishra, K., & Sinha, R. (2020). Flood risk assessment in the Kosi megafan using multi-criteria decision analysis: A hydro-geomorphic approach. *Geomorphology*, *350*, 106861. https://doi.org/10.1016/j.geomorph.2019.106861

Moriasi, D. N., Arnold, J. G., Van Liew, M. W., Bingner, R. L., Harmel, R. D., & Veith, T. L. (2007). Model evaluation guidelines for systematic quantification of accuracy in watershed simulations. *Transactions of the ASABE*, *50*(3), 885–900. https://doi.org/10.13031/2013.23153

Moriasi, D. N., Gitau, M. W., Pai, N., & Daggupait, P. (2015). Hydrologic and water quality models: Performance measures and evaluation criteria. *Transactions of the ASABE*, *58*(6), 1763–1785. https://doi.org/10.13031/trans.58.10715

Müller, A., Reiter, J., & Weiland, U. (2011). Assessment of urban vulnerability towards floods using an indicator-based approach – a case study for Santiago de Chile. *Natural Hazards and Earth System Sciences*, *11*(8), 2107–2123. https://doi.org/10.5194/nhess-11-2107-2011

Myndigheten för samhällsskydd och beredskap. (2020). *Översvämningskartering utmed Kävlingeån [Flood mapping along the river Kävlinge]*. https://www.msb.se/siteassets/dokument/amnesomraden/skydd-mot-olyckor-och-farliga-amnen/naturolyckor-och-klimat/oversvamning/oversvamningskartering-vattendrag/kavlingean-2020.pdf

Nash, J. E., & Sutcliffe, J. V. (1970). River flow forecasting through conceptual models part I — A discussion of principles. *Journal of Hydrology*, *10*(3), 282–290. https://doi.org/10.1016/0022-1694(70)90255-6

Naturvårdsverkets. (n.d.). *National Land Cover Database (NMD)*. Retrieved January 11, 2024, from https://www.naturvardsverket.se/en/services-and-permits/maps-and-map-services/national-land-cover-database/

Nkeki, F. N., Bello, E. I., & Agbaje, I. G. (2022). Flood risk mapping and urban infrastructural susceptibility assessment using a GIS and analytic hierarchical raster fusion approach in the Ona River Basin, Nigeria. *International Journal of Disaster Risk Reduction*, *77*, 103097. https://doi.org/10.1016/j.ijdrr.2022.103097

Nkeki, F. N., Bello, E. I., & Agbaje, I. G. (2023). Is the existing methods sustainable? A hybrid approach to flood risk mapping. *MethodsX*, *11*, 102348. https://doi.org/10.1016/j.mex.2023.102348

Nyberg, L., Hakkarainen, H., Blumenthal, B., & Moberg, J.-O. (2019). *Konsekvenser av sommarskyfall i Sverige under åren 2009–2018 [Impact of summer rainfall in Sweden in 2009-2018]*. Centrum för klimat och säkerhet [Center for Climate and Security]. https://www.kau.se/files/2019-05/CCS_2019-2.pdf

Olguín, E. F. (2020). *Geomorphology alteration effects over Kävlinge River Basin*. LUP Student Papers; Lund University. https://lup.lub.lu.se/luur/download?func=downloadFile&recordOId=9025697&fileOId=9025698

Ontowirjo, B., Fathurrahman, I., Ramadhan, M. V., Zahriani, A., Zahra, M., & Wahyudi, H. (2023). LiDAR DEM and HEC-RAS on-grid rainfall hydrograph model for irrigation system. *IOP Conference Series: Earth and Environmental Science*. http://dx.doi.org/10.1088/1755-1315/1198/1/012023

Orencio, P. M., & Fujii, M. (2013). A localized disaster-resilience index to assess coastal communities based on an analytic hierarchy process (AHP). *International Journal of Disaster Risk Reduction*, *3*, 62–75. https://doi.org/10.1016/j.ijdrr.2012.11.006

Ouma, Y., & Tateishi, R. (2014). Urban flood vulnerability and risk mapping using integrated multi-parametric AHP and GIS: Methodological overview and case study assessment. *Water*, *6*(6), 1515–1545. https://doi.org/10.3390/w6061515

Oumaima, B., Yves, T., El Mehdi, S. M., Simon, G., & Frederic, L. (2019). Flood hazard mapping using two digital elevation models: Application in a semi-arid environment of Morocco. *European Scientific Journal ESJ*, *15*(33). https://doi.org/10.19044/esj.2019.v15n33p338

Pasquier, U., He, Y., Hooton, S., Goulden, M., & Hiscock, K. M. (2019). An integrated 1D–2D hydraulic modelling approach to assess the sensitivity of a coastal region to compound flooding hazard under climate change. *Natural Hazards*, *98*(3), 915–937. https://doi.org/10.1007/s11069-018-3462-1

Peterson, T. C., Karl, T. R., Kossin, J. P., Kunkel, K. E., Lawrimore, J. H., McMahon, J. R., Vose, R. S., & Yin, X. (2013). Changes in weather and climate extremes: State of knowledge relevant to air and water quality in the United States. *Journal of the Air & Waste Management Association*, *64*(2), 184–197. https://doi.org/10.1080/10962247.2013.851044

Pinter, N., Ploeg, R. R. van der, Schweigert, P., & Hoefer, G. (2005). Flood magnification on the River Rhine. *Hydrological Processes*, *20*(1), 147–164. https://doi.org/10.1002/hyp.5908

Pörtner, H.-O., Roberts, D., Masson-Delmotte, V., Zhai, P., Poloczanska, E., Mintenbeck, K., Tignor, M., Petzold, J., Weyer, N., Okem, A., Craig, M., Nicolai, M., Alegría, A., Langsdorf, S., Rama, B., & Freund, A. (2019). *IPCC Special Report on Ocean and Cryosphere in a Changing Climate (SROCC) Technical Summary*. Intergovernmental Panel on Climate Change. https://www.ipcc.ch/site/assets/uploads/sites/3/2019/11/SROCC_FD_TS_Final.pdf

Prein, A. F., Liu, C., Ikeda, K., Trier, S. B., Rasmussen, R. M., Holland, G. J., & Clark, M. P. (2017). Increased rainfall volume from future convective storms in the US. *Nature Climate Change*, *7*(12), 880–884. https://doi.org/10.1038/s41558-017-0007-7

Radosavljevic, A., & Anderson, R. P. (2013). Making better Maxent models of species distributions: Complexity, overfitting and evaluation. *Journal of Biogeography*, *41*(4), 629–643. https://doi.org/10.1111/jbi.12227

Rahmati, O., Zeinivand, H., & Besharat, M. (2016). Flood hazard zoning in Yasooj region, Iran, using GIS and multi-criteria decision analysis. *Geomatics, Natural Hazards and Risk*, *7*(3), 1000–1017. https://doi.org/10.1080/19475705.2015.1045043

Refsgaard, J. C. (1997). Parameterisation, calibration and validation of distributed hydrological models. *Journal of Hydrology*, *198*(1–4), 69–97. https://doi.org/10.1016/s0022-1694(96)03329-x

Riahi, K., Rao, S., Krey, V., Cho, C., Chirkov, V., Fischer, G., Kindermann, G., Nakicenovic, N., & Rafaj, P. (2011). RCP 8.5—A scenario of comparatively high greenhouse gas emissions. *Climatic Change*, *109*(1–2), 33–57. https://doi.org/10.1007/s10584-011-0149-y

Rincón, D., Khan, U., & Armenakis, C. (2018). Flood risk mapping using GIS and multi-criteria analysis: A greater toronto area case study. *Geosciences*, *8*(8), 275. https://doi.org/10.3390/geosciences8080275

Rodriguez, L. B., Cello, P. A., Vionnet, C. A., & Goodrich, D. (2008). Fully conservative coupling of HEC-RAS with MODFLOW to simulate stream–aquifer interactions in a drainage basin. *Journal of Hydrology*, *353*(1–2), 129–142. https://doi.org/10.1016/j.jhydrol.2008.02.002

Rojas, R., Feyen, L., & Watkiss, P. (2013). Climate change and river floods in the European Union: Socio-economic consequences and the costs and benefits of adaptation. *Global Environmental Change*, *23*(6), 1737–1751. https://doi.org/10.1016/j.gloenvcha.2013.08.006

Roudier, P., Andersson, J. C. M., Donnelly, C., Feyen, L., Greuell, W., & Ludwig, F. (2015). Projections of future floods and hydrological droughts in Europe under a +2°C global warming. *Climatic Change*, *135*(2), 341–355. https://doi.org/10.1007/s10584-015-1570-4

Ryu, J., Yoon, E. J., Park, C., Lee, D. K., & Jeon, S. W. (2017). A flood risk assessment model for companies and criteria for governmental decision-making to minimize hazards. *Sustainability*, *9*(11), 2005. https://doi.org/10.3390/su9112005

Saaty, T. L. (1980). *The analytic hierarchy process: Planning, priority setting, resource allocation*. McGraw-Hill International Book Company.

Saaty, T. L. (2003). Decision-making with the AHP: Why is the principal eigenvector necessary. *European Journal of Operational Research*, *145*(1), 85–91. https://doi.org/10.1016/s0377-2217(02)00227-8

Savitri, Y. R., Kakimoto, R., Anwar, N., Wardoyo, W., & Suryani, E. (2021). Reliability of 2d hydrodynamic model on flood inundation analysis. *International Journal of Geomate*, *21*(83). https://doi.org/10.21660/2021.83.j2073

Seiller, G., Anctil, F., & Perrin, C. (2012). Multimodel evaluation of twenty lumped hydrological models under contrasted climate conditions. *Hydrology and Earth System Sciences*, *16*(4), 1171–1189. https://doi.org/10.5194/hess-16-1171-2012

Shahid, S., & Behrawan, H. (2008). Drought risk assessment in the western part of Bangladesh. *Natural Hazards*, *46*(3), 391–413. https://doi.org/10.1007/s11069-007-9191-5

Sheffer, N. A., Rico, M., Enzel, Y., Benito, G., & Grodek, T. (2008). The Palaeoflood record of the Gardon River, France: A comparison with the extreme 2002 flood event. *Geomorphology*, *98*(1–2), 71–83. https://doi.org/10.1016/j.geomorph.2007.02.034

Sholichin, M., & Qadri, W. (2020). Predicting flood hazards area using swat and hec-ras simulation in Bila river, South Sulawesi. *IOP Conference Series: Earth and Environmental Science*, *437*(1), 012055. https://doi.org/10.1088/1755-1315/437/1/012055

Shrestha, S., & Lohpaisankrit, W. (2017). Flood hazard assessment under climate change scenarios in the Yang River Basin, Thailand. *International Journal of Sustainable Built Environment*, *6*(2), 285–298. https://doi.org/10.1016/j.ijsbe.2016.09.006

Smit, B., & Wandel, J. (2006). Adaptation, adaptive capacity and vulnerability. *Global Environmental Change*, *16*(3), 282–292. https://doi.org/10.1016/j.gloenvcha.2006.03.008

Statistikmyndigheten SCB. (2024). *Open data for grid statistics*. https://www.scb.se/en/services/open-data-api/open-geodata/grid-statistics/

Stavi, I., Eldad, S., Xu, C., Xu, Z., Gusarov, Y., Haiman, M., & Argaman, E. (2024). Ancient agricultural terrace walls control floods and regulate the distribution of Asphodelus ramosus geophytes in the Israeli arid Negev. *CATENA*, *234*, 107588. https://doi.org/10.1016/j.catena.2023.107588

Suriya, S., & Mudgal, B. V. (2012). Impact of urbanization on flooding: The Thirusoolam sub watershed – A case study. *Journal of Hydrology*, *412–413*, 210–219. https://doi.org/10.1016/j.jhydrol.2011.05.008

Sveriges Geologiska Undersökning. (2024). *Soil types 1:25 000-1:100 000*. https://www.sgu.se/produkter-och-tjanster/geologiska-data/data-enligt-inspire/framtagna-inspiredata/ge.jordarter-125000-1100000/

Swedish Meteorological and Hydrological Institute. (2024a). *Advanced climate change scenario service*. https://www.smhi.se/en/climate/future-climate/advanced-climate-change-scenario-service/met/sverige/medelnederbord/rcp85/2071-2100/year/abs

Swedish Meteorological and Hydrological Institute. (2024b). *Data och analyser för väder samt Sveriges klimat och miljö [Data and analysis for weather and Sweden's climate and environment]*. https://www.smhi.se/data

Tayefi, V., Lane, S. N., Hardy, R. J., & Yu, D. (2007). A comparison of one- and two-dimensional approaches to modelling flood inundation over complex upland floodplains. *Hydrological Processes*, *21*(23), 3190–3202. https://doi.org/10.1002/hyp.6523

Teknomo, K. (2006). *Analytic Hierarchy Process (AHP) Tutorial*. Revoledu. https://people.revoledu.com/kardi/tutorial/AHP/

Tingsanchali, T., & Karim, M. F. (2005). Flood hazard and risk analysis in the southwest region of Bangladesh. *Hydrological Processes*, *19*(10), 2055–2069. https://doi.org/10.1002/hyp.5666

Tollgren, J., & Walldén, J. (2017). *En flödesanalys för Kävlingeån - HEC-RAS modellering med fokus på dämmens inverkan [A flow analysis for Kävlingeån - HEC-RAS modeling with focus on the impact of the dam]*. LUP Student Papers; Lund University. https://lup.lub.lu.se/luur/download?func=downloadFile&recordOId=8928253&fileOId=8928257

Trafikverket. (2024). *Traffic Data*. Trafficdata.Se. https://trafficdata.se/dataset/

Tran, P., Shaw, R., Chantry, G., & Norton, J. (2008). GIS and local knowledge in disaster management: A case study of flood risk mapping in Viet Nam. *Disasters*, *33*(1), 152–169. https://doi.org/10.1111/j.1467-7717.2008.01067.x

Turner, B. L., Kasperson, R. E., Matson, P. A., McCarthy, J. J., Corell, R. W., Christensen, L., Eckley, N., Kasperson, J. X., Luers, A., Martello, M. L., Polsky, C., Pulsipher, A., & Schiller, A. (2003). A Framework for Vulnerability Analysis in Sustainability Science. *Proceedings of the National Academy of Sciences of the United States of America*, *100*(14). https://doi.org/10.1073/pnas.1231335100

United Nations International Strategy for Disaster Reduction. (2009). *Terminology on disaster risk reduction*. https://www.unisdr.org/files/7817_UNISDRTerminologyEnglish.pdf

Van Calster, B., McLernon, D. J., van Smeden, M., Wynants, L., & Steyerberg, E. W. (2019). Calibration: The Achilles heel of predictive analytics. *BMC Medicine*, *17*(1). https://doi.org/10.1186/s12916-019-1466-7

van Westen, C. J., van Asch, T. W. J., & Soeters, R. (2005). Landslide hazard and risk zonation—why is it still so difficult? *Bulletin of Engineering Geology and the Environment*, *65*(2), 167–184. https://doi.org/10.1007/s10064-005-0023-0

Vangelis, H., Zotou, I., Kourtis, I. M., Bellos, V., & Tsihrintzis, V. A. (2022). Relationship of rainfall and flood return periods through hydrologic and hydraulic modeling. *Water*, *14*(22), 3618. https://doi.org/10.3390/w14223618

Vázquez, R. F., Feyen, L., Feyen, J., & Refsgaard, J. C. (2002). Effect of grid size on effective parameters and model performance of the MIKE-SHE code. *Hydrological Processes*, *16*(2), 355–372. https://doi.org/10.1002/hyp.334

Vojtek, M., & Vojteková, J. (2016). Flood hazard and flood risk assessment at the local spatial scale: A case study. *Geomatics, Natural Hazards and Risk*, *7*(6), 1973–1992. https://doi.org/10.1080/19475705.2016.1166874

Weichselgartner, J. (2001). Disaster mitigation: The concept of vulnerability revisited. *Disaster Prevention and Management: An International Journal*, *10*(2), 85–95. https://doi.org/10.1108/09653560110388609

Wicher, K. (2016). *Rainfall Runoff Modeling in Kävlinge River Basin with HEC-HMS*. LUP Student Papers; Lund University. https://lup.lub.lu.se/luur/download?func=downloadFile&recordOId=8890161&fileOId=8890402

Wisner, B., Blaikie, P. M., Cannon, T., & Davis, I. (1994). *At risk: Natural hazards, people's vulnerability, and disasters* (2nd ed.). Routledge.

Wu, J., Chen, X., & Lu, J. (2022). Assessment of long and short-term flood risk using the multi-criteria analysis model with the AHP-Entropy method in Poyang Lake basin. *International Journal of Disaster Risk Reduction*, *75*, 102968. https://doi.org/10.1016/j.ijdrr.2022.102968

Wu, Y., Zhong, P., Zhang, Y., Xu, B., Ma, B., & Yan, K. (2015). Integrated flood risk assessment and zonation method: A case study in Huaihe River basin, China. *Natural Hazards*, *78*(1), 635–651. https://doi.org/10.1007/s11069-015-1737-3

Xu, J., Cai, H., Saddique, Q., Wang, X., Li, L., Ma, C., & Lu, Y. (2019). Evaluation and optimization of border irrigation in different irrigation seasons based on temporal variation of infiltration and roughness. *Agricultural Water Management*, *214*, 64–77. https://doi.org/10.1016/j.agwat.2019.01.003

Yochum, S. E., Goertz, L. A., & Jones, P. H. (2008). Case study of the big bay dam failure: Accuracy and comparison of breach predictions. *Journal of Hydraulic Engineering*, *134*(9), 1285–1293. https://doi.org/10.1061/(ASCE)0733-9429(2008)134:9(1285)

Zeiger, S. J., & Hubbart, J. A. (2021). Measuring and modeling event-based environmental flows: An assessment of HEC-RAS 2D rain-on-grid simulations. *Journal of Environmental Management*, *285*, 112125. https://doi.org/10.1016/j.jenvman.2021.112125

Zhang, K., Shalehy, M. H., Ezaz, G. T., Chakraborty, A., Mohib, K. M., & Liu, L. (2022). An integrated flood risk assessment approach based on coupled hydrological-hydraulic modeling and bottom-up hazard vulnerability analysis. *Environmental Modelling & Software*, *148*, 105279. https://doi.org/10.1016/j.envsoft.2021.105279

Zhong, M., Xiao, L., Li, X., Mei, Y., Jiang, T., Song, L., & Chen, X. (2024). A study on compound flood prediction and inundation simulation under future scenarios in a coastal city. *Journal of Hydrology*, *628*, 130475. https://doi.org/10.1016/j.jhydrol.2023.130475

Zope, P. E., Eldho, T. I., & Jothiprakash, V. (2015). Impacts of urbanization on flooding of a coastal urban catchment: A case study of Mumbai City, India. *Natural Hazards*, *75*(1), 887–908. https://doi.org/10.1007/s11069-014-1356-4

Zou, Q., Zhou, J., Zhou, C., Song, L., & Guo, J. (2012). Comprehensive flood risk assessment based on set pair analysis-variable fuzzy sets model and fuzzy AHP. *Stochastic Environmental Research and Risk Assessment*, *27*(2), 525–546. https://doi.org/10.1007/s00477-012-0598-5

Appendices

Appendix 1: Manning's Coefficient of Roughness (n) Values

Table A1: Manning's Coefficient of Roughness (n) Values used as Parameters in the HEC-RAS Rain-on-Grid Model

Name	Classification Value	Original n ($s/m^{1/3}$)	Calibrated n (+40%, $s/m^{1/3}$)
Open wetland	2	0.05	0.07
Arable land	3	0.033	0.0462
Non-vegetated other open land	41	0.03	0.042
Vegetated other open land	42	0.05	0.07
Artificial surfaces, building	51	0.03	0.042
Artificial surfaces, not building or road/railway	52	0.07	0.098
Artificial surfaces, road/railway	53	0.03	0.042
Inland water	61	0.035	0.049
Pine forest not on wetland	111	0.12	0.168
Spruce forest not on wetland	112	0.12	0.168
Mixed coniferous not on wetland	113	0.12	0.168
Mixed forest not on wetland	114	0.1	0.14
Deciduous forest not on wetland	115	0.1	0.14
Deciduous hardwood forest not on wetland	116	0.1	0.14
Deciduous forest with deciduous hardwood forest not on wetland	117	0.1	0.14
Temporarily non-forest not on wetland	118	0.04	0.056
Pine forest on wetland	121	0.062	0.0868
Spruce forest on wetland	122	0.062	0.0868
Mixed coniferous on wetland	123	0.062	0.0868
Mixed forest on wetland	124	0.06	0.084
Deciduous forest on wetland	125	0.06	0.084
Deciduous hardwood forest on wetland	126	0.06	0.084
Deciduous forest with deciduous hardwood forest on wetland	127	0.06	0.084
Temporarily non-forest on wetland	128	0.05	0.07

Appendix 2: Total Vulnerability Raster Calculator Script

```
"Vulnerability\OtherRas" * .064 + "Vulnerability\AgeRas" *.108 + "Vulnerability\PopDenRas" *.108 + "Vulnerability\SchoolRas" *.195 + "Vulnerability\LCRas" *.332 + "Vulnerability\pathcon" *.195
```

Appendix 3: Comparing Calibrated Observed and Simulated Hydrographs

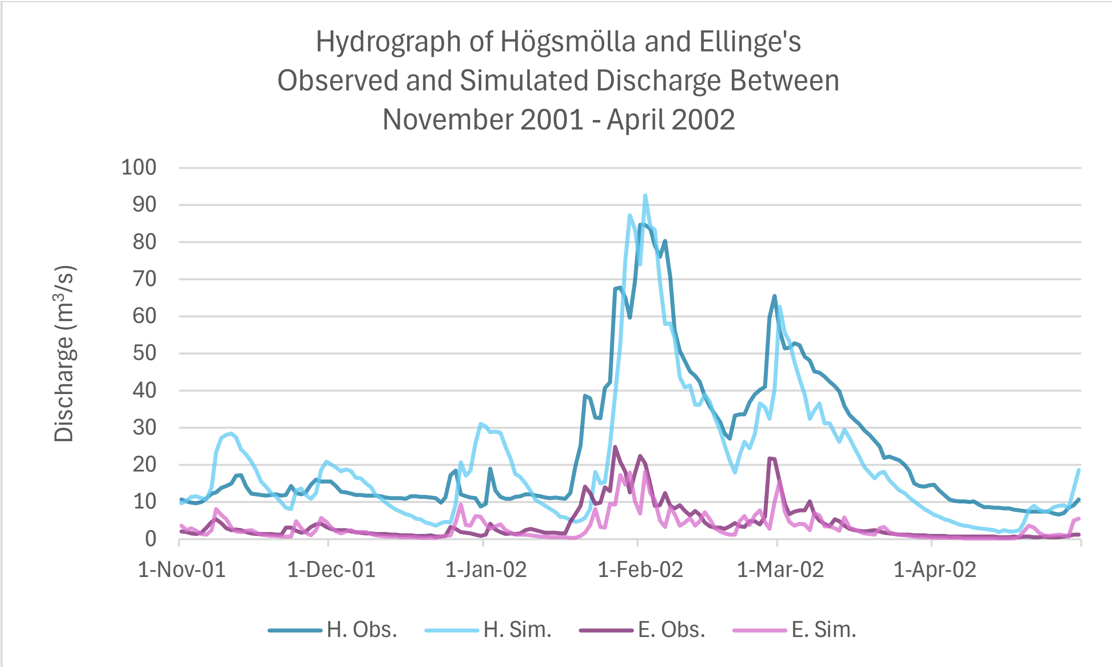

Figure A1: Comparison of hydrographs of Högsmölla and Ellinge's Observed and Simulated Discharge Between November 2001 - April 2002, a 6-month period used for calibration for the HEC-RAS rain-on-grid model for the Kävlinge River.

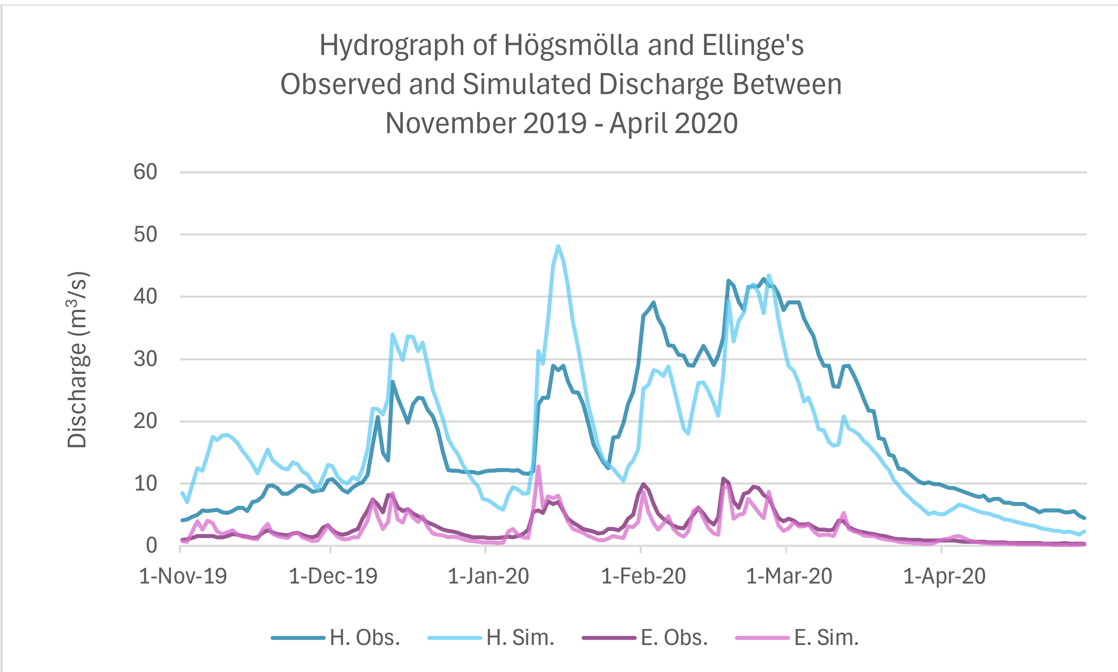

Figure A2: Comparison of hydrographs of Högsmölla and Ellinge's Observed and Simulated Discharge Between November 2019 - April 2020, a 6-month period used for calibration for the HEC-RAS rain-on-grid model for the Kävlinge River.

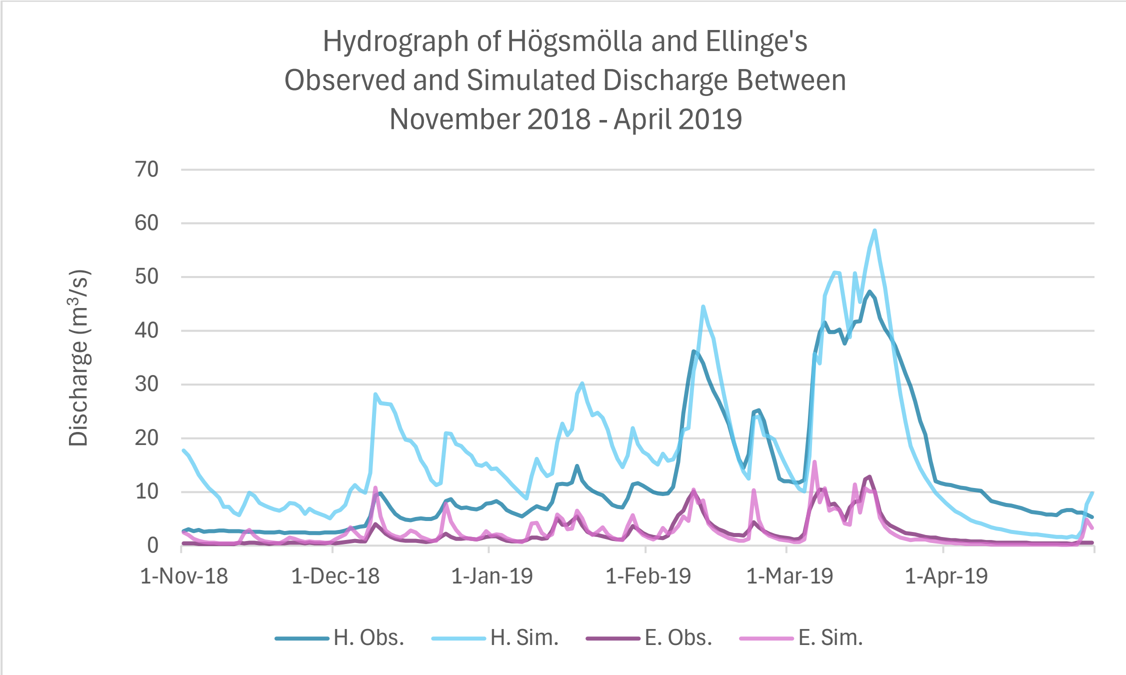

Figure A3: Comparison of hydrographs of Högsmölla and Ellinge's Observed and Simulated Discharge Between November 2018 - April 2019.

a 6-month period used for calibration for the HEC-RAS rain-on-grid model for the Kävlinge River.

Appendix 4: Comparing Validated Observed and Simulated Hydrographs

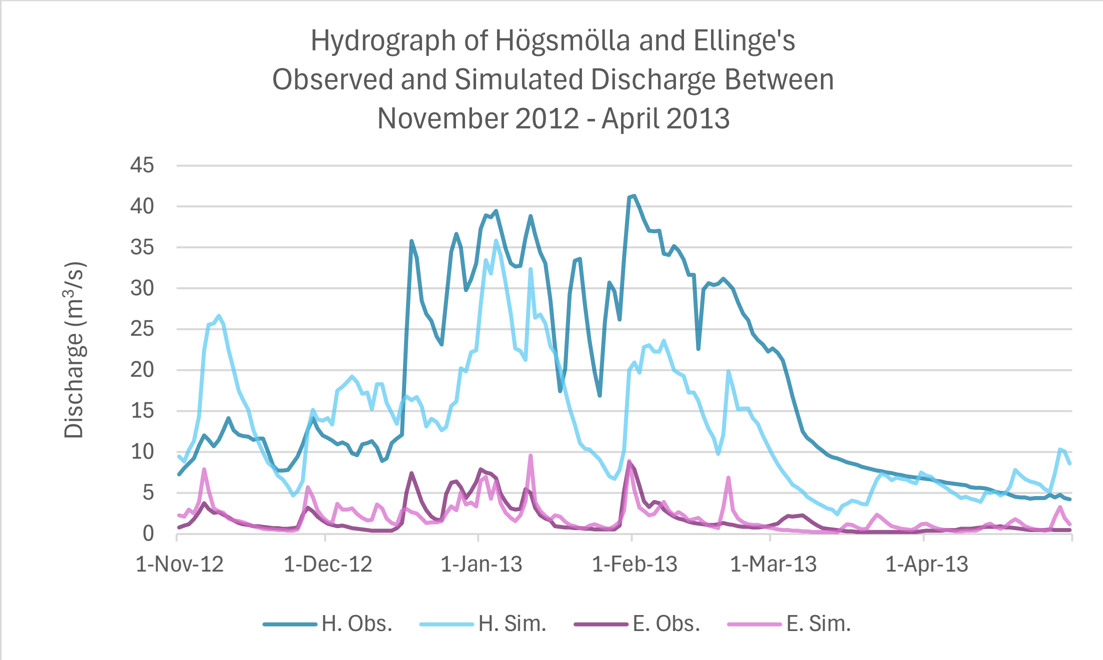

Figure A4: Comparison of hydrographs of Högsmölla and Ellinge's Observed and Simulated Discharge Between November 2012 - April 2013, a 6-month period used for validation of the HEC-RAS rain-on-grid model for the Kävlinge River.

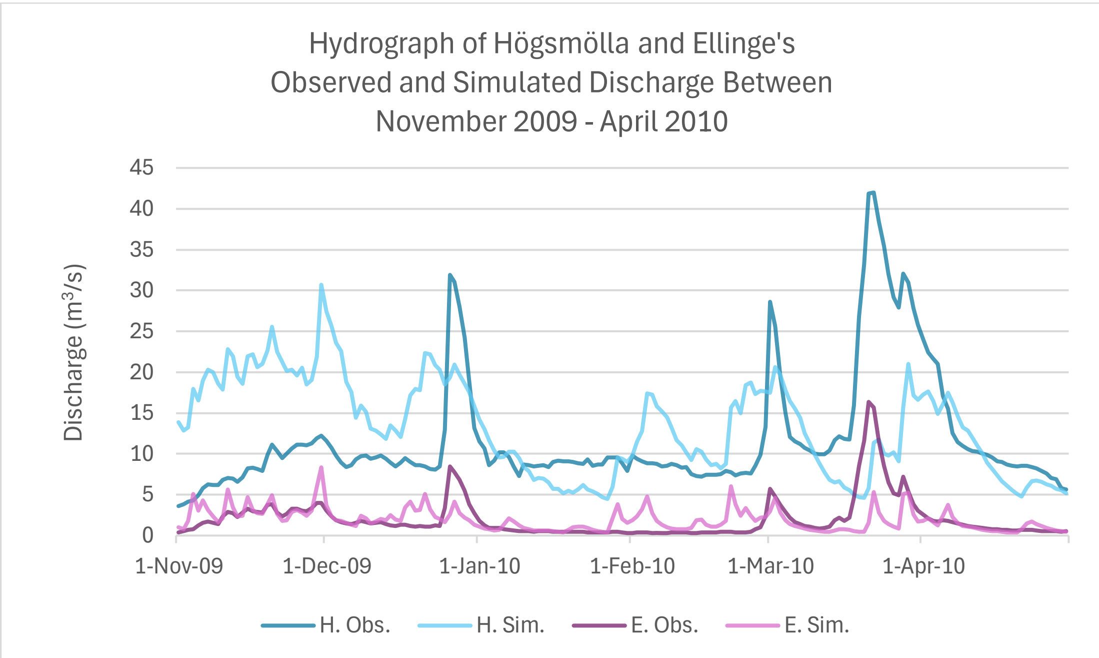

Figure A5: Comparison of hydrographs of Högsmölla and Ellinge's Observed and Simulated Discharge Between November 2009 - April 2010, a 6-month period used for validation of the HEC-RAS rain-on-grid model for the Kävlinge River.

Appendix 5: Vulnerability Map – Land Cover

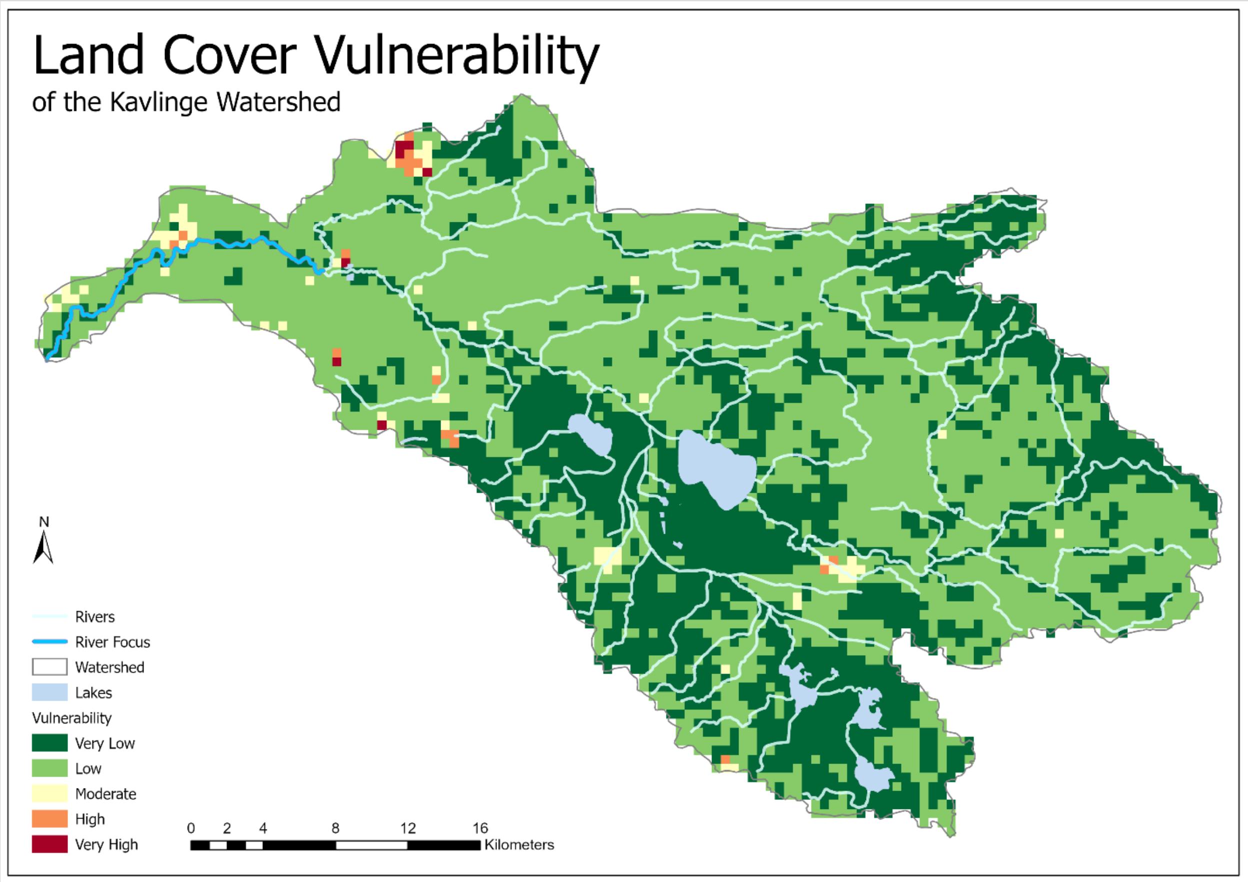

Figure A6: Map of Relative Land Cover Vulnerability of the Kävlinge Watershed, created using ArcGIS Pro.

Appendix 6: Vulnerability Map – Schools

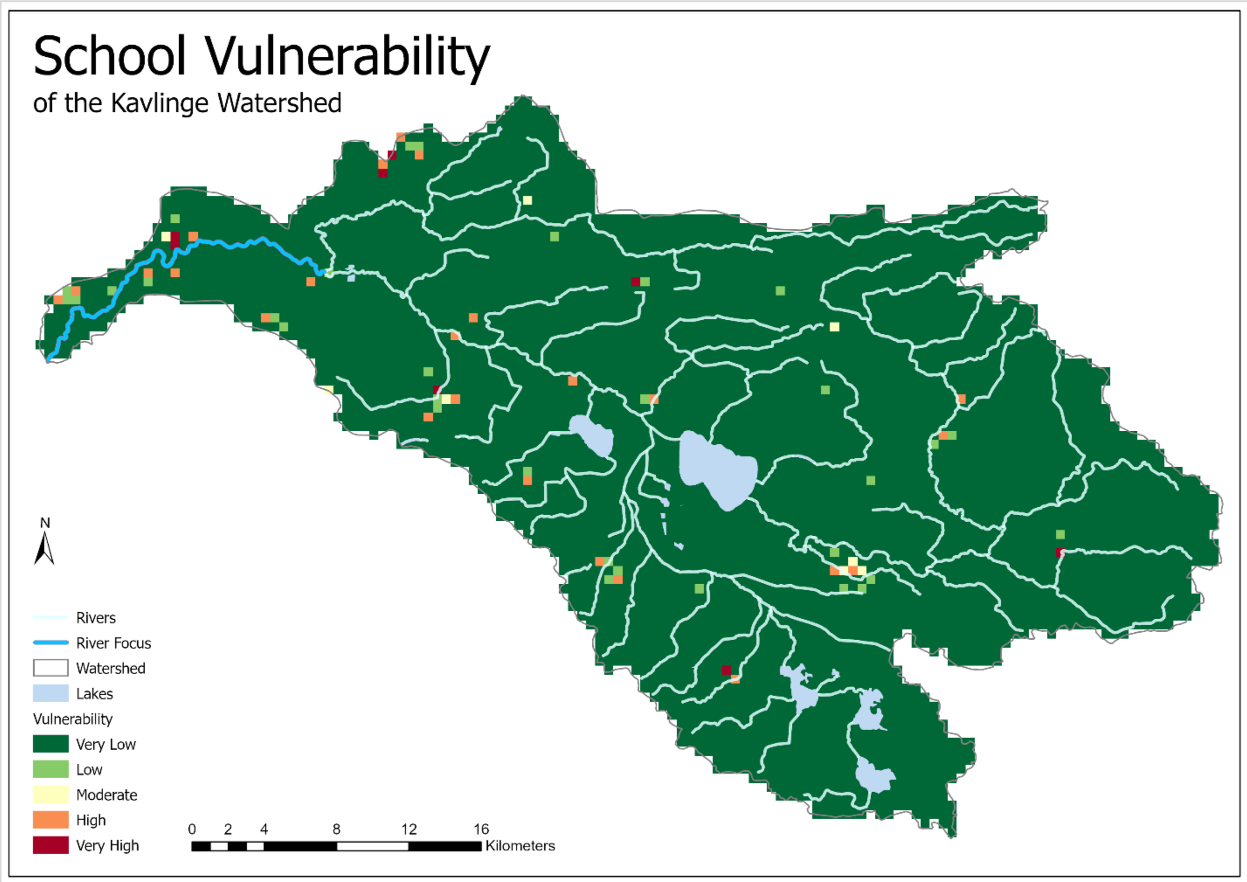

Figure A7: Map of Relative School Proximity Vulnerability of the Kävlinge Watershed, based on density. Created using ArcGIS Pro.

Appendix 7: Vulnerability Map – Roads and Railways

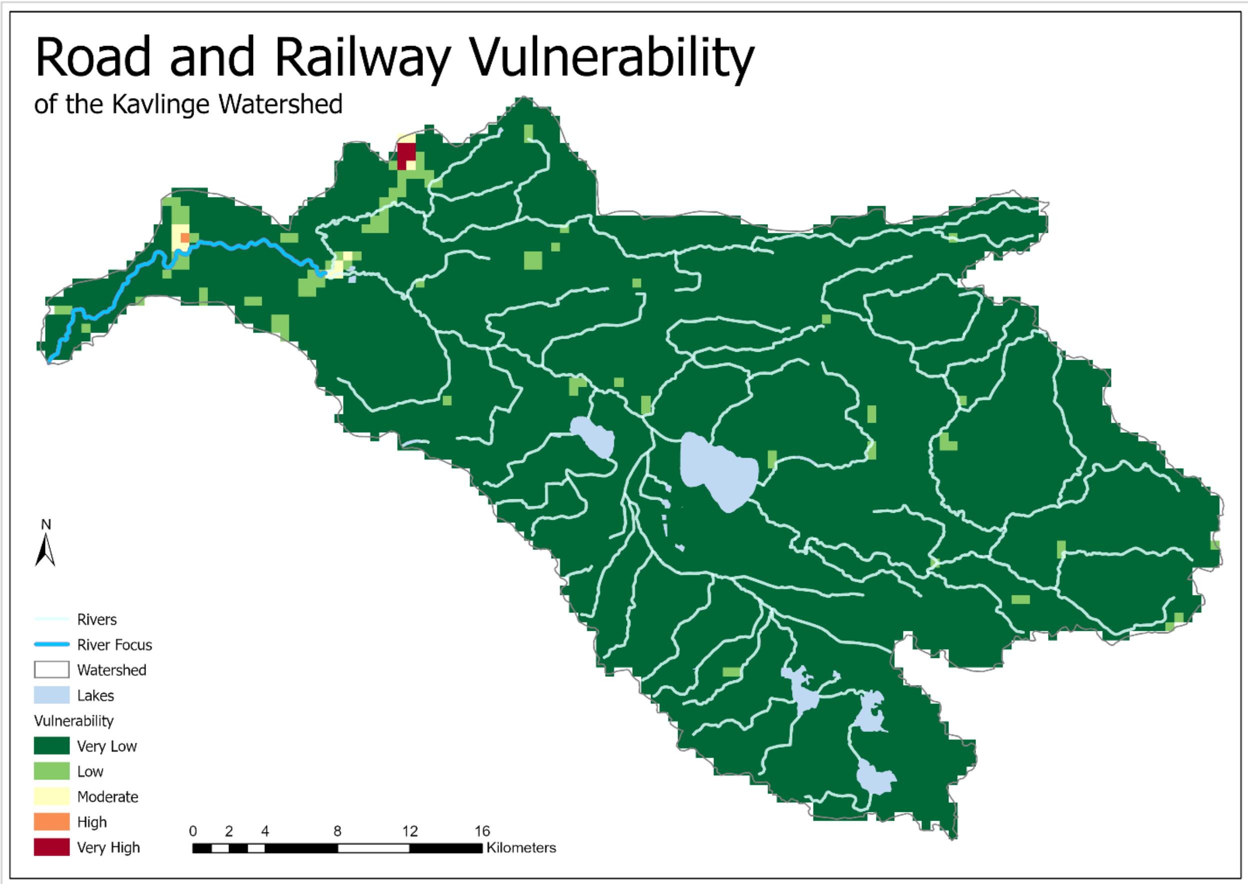

Figure A8: Map of Relative Road and Railway Vulnerability of the Kävlinge Watershed, based on density. Created using ArcGIS Pro.

Appendix 8: Vulnerability Map – Population Density

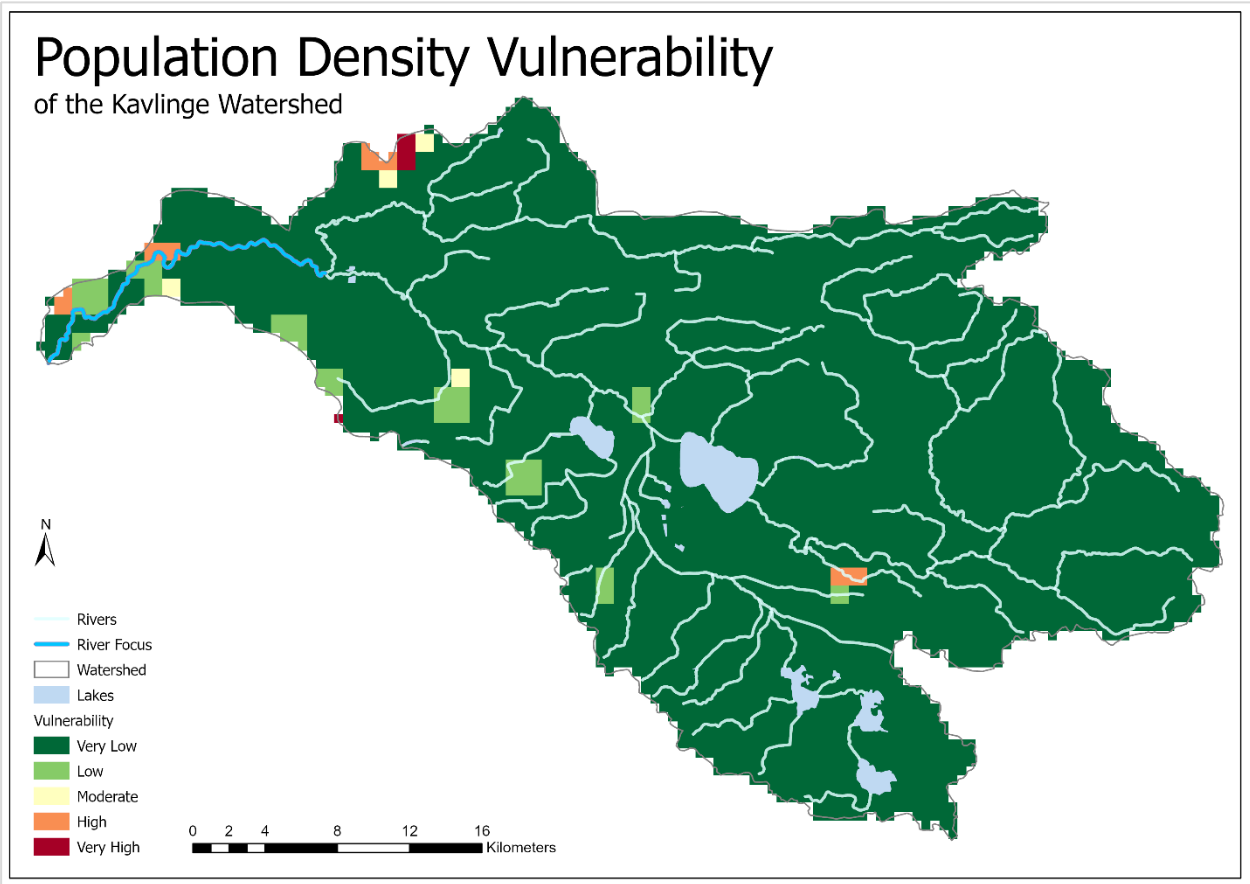

Figure A9: Map of Relative Population Density Vulnerability of the Kävlinge Watershed, created using ArcGIS Pro.

Appendix 9: Vulnerability Map – Population Fragility

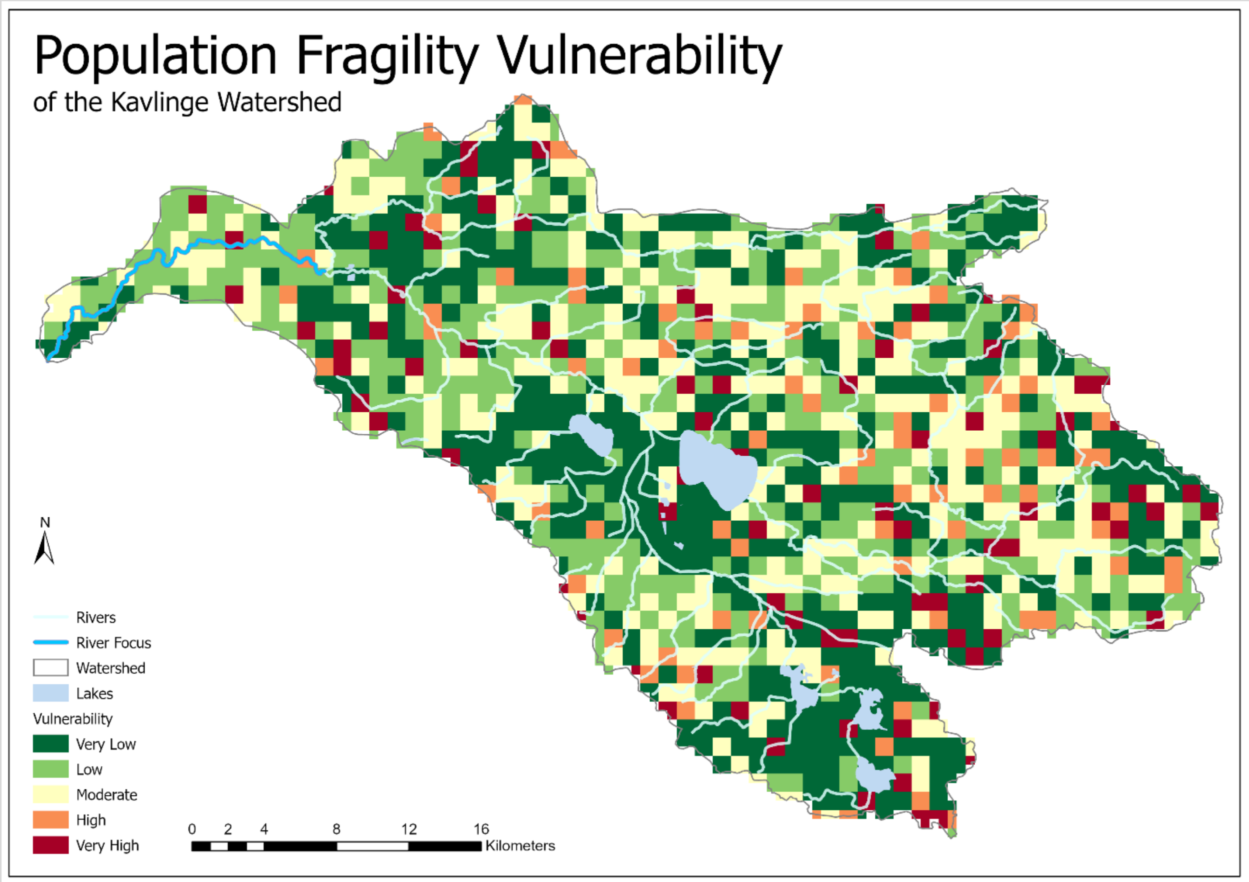

Figure A10: Map of Relative Population Fragility Vulnerability of the Kävlinge Watershed, based on density of ages under 10 and over 60.
Created using ArcGIS Pro.

Appendix 10: Vulnerability Map – Municipal Building and Cultural Sites

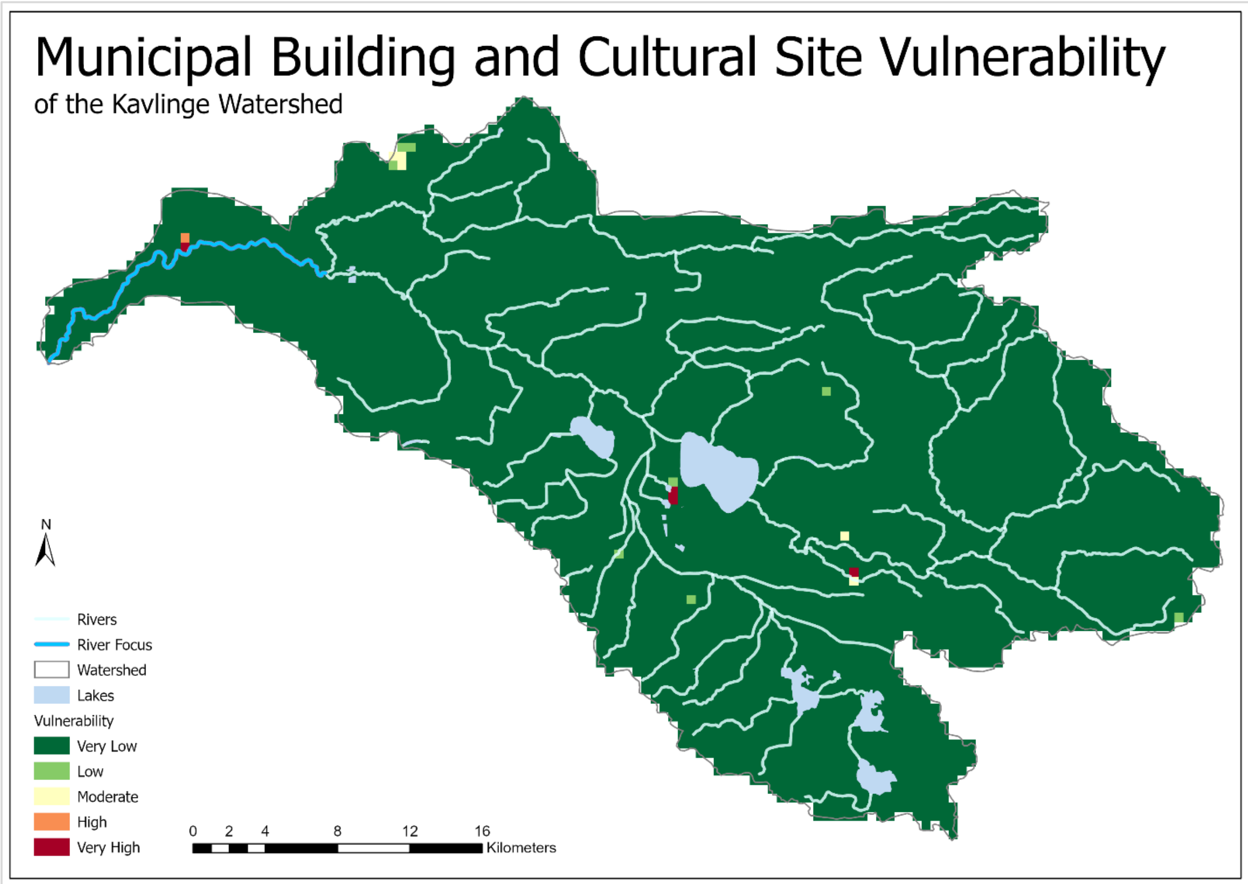

Figure A11: Map of Relative Municipal Building and Cultural Site Vulnerability of the Kävlinge Watershed, based on density. Created using ArcGIS Pro.

Series from Lund University

Department of Physical Geography and Ecosystem Science

Master Thesis in Geographical Information Science

1. *Anthony Lawther:* The application of GIS-based binary logistic regression for slope failure susceptibility mapping in the Western Grampian Mountains, Scotland (2008).
2. *Rickard Hansen:* Daily mobility in Grenoble Metropolitan Region, France. Applied GIS methods in time geographical research (2008).
3. *Emil Bayramov:* Environmental monitoring of bio-restoration activities using GIS and Remote Sensing (2009).
4. *Rafael Villarreal Pacheco:* Applications of Geographic Information Systems as an analytical and visualization tool for mass real estate valuation: a case study of Fontibon District, Bogota, Columbia (2009).
5. *Siri Oestreich Waage:* a case study of route solving for oversized transport: The use of GIS functionalities in transport of transformers, as part of maintaining a reliable power infrastructure (2010).
6. *Edgar Pimiento:* Shallow landslide susceptibility – Modelling and validation (2010).
7. *Martina Schäfer:* Near real-time mapping of floodwater mosquito breeding sites using aerial photographs (2010).
8. *August Pieter van Waarden-Nagel:* Land use evaluation to assess the outcome of the programme of rehabilitation measures for the river Rhine in the Netherlands (2010).
9. *Samira Muhammad:* Development and implementation of air quality data mart for Ontario, Canada: A case study of air quality in Ontario using OLAP tool. (2010).
10. *Fredros Oketch Okumu*: Using remotely sensed data to explore spatial and temporal relationships between photosynthetic productivity of vegetation and malaria transmission intensities in selected parts of Africa (2011).
11. *Svajunas Plunge:* Advanced decision support methods for solving diffuse water pollution problems (2011).

12. *Jonathan Higgins:* Monitoring urban growth in greater Lagos: A case study using GIS to monitor the urban growth of Lagos 1990 - 2008 and produce future growth prospects for the city (2011).

13. *Mårten Karlberg:* Mobile Map Client API: Design and Implementation for Android (2011).

14. *Jeanette McBride:* Mapping Chicago area urban tree canopy using color infrared imagery (2011).

15. *Andrew Farina:* Exploring the relationship between land surface temperature and vegetation abundance for urban heat island mitigation in Seville, Spain (2011).

16. *David Kanyari*: Nairobi City Journey Planner: An online and a Mobile Application (2011).

17. *Laura V. Drews:* Multi-criteria GIS analysis for siting of small wind power plants - A case study from Berlin (2012).

18. *Qaisar Nadeem:* Best living neighborhood in the city - A GIS based multi criteria evaluation of ArRiyadh City (2012).

19. *Ahmed Mohamed El Saeid Mustafa:* Development of a photo voltaic building rooftop integration analysis tool for GIS for Dokki District, Cairo, Egypt (2012).

20. *Daniel Patrick Taylor*: Eastern Oyster Aquaculture: Estuarine Remediation via Site Suitability and Spatially Explicit Carrying Capacity Modeling in Virginia's Chesapeake Bay (2013).

21. *Angeleta Oveta Wilson:* A Participatory GIS approach to *unearthing* Manchester's Cultural Heritage '*gold mine'* (2013).

22. *Ola Svensson:* Visibility and Tholos Tombs in the Messenian Landscape: A Comparative Case Study of the Pylian Hinterlands and the Soulima Valley (2013).

23. *Monika Ogden:* Land use impact on water quality in two river systems in South Africa (2013).

24. *Stefan Rova:* A GIS based approach assessing phosphorus load impact on Lake Flaten in Salem, Sweden (2013).

25. *Yann Buhot:* Analysis of the history of landscape changes over a period of 200 years. How can we predict past landscape pattern scenario and the impact on habitat diversity? (2013).

26. *Christina Fotiou:* Evaluating habitat suitability and spectral heterogeneity models to predict weed species presence (2014).

27. *Inese Linuza:* Accuracy Assessment in Glacier Change Analysis (2014).

28. *Agnieszka Griffin:* Domestic energy consumption and social living standards: a GIS analysis within the Greater London Authority area (2014).

29. *Brynja Guðmundsdóttir:* Detection of potential arable land with remote sensing and GIS - A Case Study for Kjósarhreppur (2014).

30. *Oleksandr Nekrasov:* Processing of MODIS Vegetation Indices for analysis of agricultural droughts in the southern Ukraine between the years 2000-2012 (2014).

31. *Sarah Tressel:* Recommendations for a polar Earth science portal in the context of Arctic Spatial Data Infrastructure (2014).

32. *Caroline Gevaert:* Combining Hyperspectral UAV and Multispectral Formosat-2 Imagery for Precision Agriculture Applications (2014).

33. *Salem Jamal-Uddeen:* Using GeoTools to implement the multi-criteria evaluation analysis - weighted linear combination model (2014).

34. *Samanah Seyedi-Shandiz:* Schematic representation of geographical railway network at the Swedish Transport Administration (2014).

35. *Kazi Masel Ullah:* Urban Land-use planning using Geographical Information System and analytical hierarchy process: case study Dhaka City (2014).

36. *Alexia Chang-Wailing Spitteler:* Development of a web application based on MCDA and GIS for the decision support of river and floodplain rehabilitation projects (2014).

37. *Alessandro De Martino:* Geographic accessibility analysis and evaluation of potential changes to the public transportation system in the City of Milan (2014).

38. *Alireza Mollasalehi:* GIS Based Modelling for Fuel Reduction Using Controlled Burn in Australia. Case Study: Logan City, QLD (2015).

39. *Negin A. Sanati:* Chronic Kidney Disease Mortality in Costa Rica; Geographical Distribution, Spatial Analysis and Non-traditional Risk Factors (2015).

40. *Karen McIntyre:* Benthic mapping of the Bluefields Bay fish sanctuary, Jamaica (2015).

41. *Kees van Duijvendijk:* Feasibility of a low-cost weather sensor network for agricultural purposes: A preliminary assessment (2015).

42. *Sebastian Andersson Hylander:* Evaluation of cultural ecosystem services using GIS (2015).

43. *Deborah Bowyer:* Measuring Urban Growth, Urban Form and Accessibility as Indicators of Urban Sprawl in Hamilton, New Zealand (2015).

44. *Stefan Arvidsson:* Relationship between tree species composition and phenology extracted from satellite data in Swedish forests (2015).

45. *Damián Giménez Cruz*: GIS-based optimal localisation of beekeeping in rural Kenya (2016).

46. *Alejandra Narváez Vallejo:* Can the introduction of the topographic indices in LPJ-GUESS improve the spatial representation of environmental variables? (2016).

47. *Anna Lundgren:* Development of a method for mapping the highest coastline in Sweden using breaklines extracted from high resolution digital elevation models (2016).

48. *Oluwatomi Esther Adejoro:* Does location also matter? A spatial analysis of social achievements of young South Australians (2016).

49. *Hristo Dobrev Tomov:* Automated temporal NDVI analysis over the Middle East for the period 1982 - 2010 (2016).

50. *Vincent Muller:* Impact of Security Context on Mobile Clinic Activities A GIS Multi Criteria Evaluation based on an MSF Humanitarian Mission in Cameroon (2016).

51. *Gezahagn Negash Seboka:* Spatial Assessment of NDVI as an Indicator of Desertification in Ethiopia using Remote Sensing and GIS (2016).

52. *Holly Buhler:* Evaluation of Interfacility Medical Transport Journey Times in Southeastern British Columbia. (2016).

53. *Lars Ole Grottenberg*: Assessing the ability to share spatial data between emergency management organisations in the High North (2016).

54. *Sean Grant:* The Right Tree in the Right Place: Using GIS to Maximize the Net Benefits from Urban Forests (2016).

55. *Irshad Jamal:* Multi-Criteria GIS Analysis for School Site Selection in Gorno-Badakhshan Autonomous Oblast, Tajikistan (2016).

56. *Fulgencio Sanmartín:* Wisdom-volkano: A novel tool based on open GIS and time-series visualization to analyse and share volcanic data (2016).

57. *Nezha Acil:* Remote sensing-based monitoring of snow cover dynamics and its influence on vegetation growth in the Middle Atlas Mountains (2016).

58. *Julia Hjalmarsson:* A Weighty Issue: Estimation of Fire Size with Geographically Weighted Logistic Regression (2016).

59. *Mathewos Tamiru Amato:* Using multi-criteria evaluation and GIS for chronic food and nutrition insecurity indicators analysis in Ethiopia (2016).

60. *Karim Alaa El Din Mohamed Soliman El Attar:* Bicycling Suitability in Downtown, Cairo, Egypt (2016).

61. *Gilbert Akol Echelai:* Asset Management: Integrating GIS as a Decision Support Tool in Meter Management in National Water and Sewerage Corporation (2016).

62. *Terje Slinning:* Analytic comparison of multibeam echo soundings (2016).

63. *Gréta Hlín Sveinsdóttir:* GIS-based MCDA for decision support: A framework for wind farm siting in Iceland (2017).

64. *Jonas Sjögren:* Consequences of a flood in Kristianstad, Sweden: A GIS-based analysis of impacts on important societal functions (2017).

65. *Nadine Raska:* 3D geologic subsurface modelling within the Mackenzie Plain, Northwest Territories, Canada (2017).

66. *Panagiotis Symeonidis*: Study of spatial and temporal variation of atmospheric optical parameters and their relation with PM 2.5 concentration over Europe using GIS technologies (2017).

67. *Michaela Bobeck:* A GIS-based Multi-Criteria Decision Analysis of Wind Farm Site Suitability in New South Wales, Australia, from a Sustainable Development Perspective (2017).

68. *Raghdaa Eissa*: Developing a GIS Model for the Assessment of Outdoor Recreational Facilities in New Cities Case Study: Tenth of Ramadan City, Egypt (2017).

69. *Zahra Khais Shahid*: Biofuel plantations and isoprene emissions in Svea and Götaland (2017).

70. *Mirza Amir Liaquat Baig*: Using geographical information systems in epidemiology: Mapping and analyzing occurrence of diarrhea in urban - residential area of Islamabad, Pakistan (2017).

71. *Joakim Jörwall*: Quantitative model of Present and Future well-being in the EU-28: A spatial Multi-Criteria Evaluation of socioeconomic and climatic comfort factors (2017).

72. *Elin Haettner*: Energy Poverty in the Dublin Region: Modelling Geographies of Risk (2017).

73. *Harry Eriksson*: Geochemistry of stream plants and its statistical relations to soil- and bedrock geology, slope directions and till geochemistry. A GIS-analysis of small catchments in northern Sweden (2017).

74. *Daniel Gardevärn:* PPGIS and Public meetings – An evaluation of public participation methods for urban planning (2017).

75. *Kim Friberg:* Sensitivity Analysis and Calibration of Multi Energy Balance Land Surface Model Parameters (2017).

76. *Viktor Svanerud:* Taking the bus to the park? A study of accessibility to green areas in Gothenburg through different modes of transport (2017).

77. *Lisa-Gaye Greene*: Deadly Designs: The Impact of Road Design on Road Crash Patterns along Jamaica's North Coast Highway (2017).

78. *Katarina Jemec Parker*: Spatial and temporal analysis of fecal indicator bacteria concentrations in beach water in San Diego, California (2017).

79. *Angela Kabiru*: An Exploratory Study of Middle Stone Age and Later Stone Age Site Locations in Kenya's Central Rift Valley Using Landscape Analysis: A GIS Approach (2017).

80. *Kristean Björkmann*: Subjective Well-Being and Environment: A GIS-Based Analysis (2018).

81. *Williams Erhunmonmen Ojo*: Measuring spatial accessibility to healthcare for people living with HIV-AIDS in southern Nigeria (2018).

82. *Daniel Assefa*: Developing Data Extraction and Dynamic Data Visualization (Styling) Modules for Web GIS Risk Assessment System (WGRAS). (2018).

83. *Adela Nistora*: Inundation scenarios in a changing climate: assessing potential impacts of sea-level rise on the coast of South-East England (2018).

84. *Marc Seliger*: Thirsty landscapes - Investigating growing irrigation water consumption and potential conservation measures within Utah's largest master-planned community: Daybreak (2018).

85. *Luka Jovičić*: Spatial Data Harmonisation in Regional Context in Accordance with INSPIRE Implementing Rules (2018).

86. *Christina Kourdounouli*: Analysis of Urban Ecosystem Condition Indicators for the Large Urban Zones and City Cores in EU (2018).

87. *Jeremy Azzopardi*: Effect of distance measures and feature representations on distance-based accessibility measures (2018).

88. *Patrick Kabatha*: An open source web GIS tool for analysis and visualization of elephant GPS telemetry data, alongside environmental and anthropogenic variables (2018).

89. *Richard Alphonce Giliba*: Effects of Climate Change on Potential Geographical Distribution of Prunus africana (African cherry) in the Eastern Arc Mountain Forests of Tanzania (2018).

90. *Eiður Kristinn Eiðsson*: Transformation and linking of authoritative multi-scale geodata for the Semantic Web: A case study of Swedish national building data sets (2018).

91. *Niamh Harty*: HOP!: a PGIS and citizen science approach to monitoring the condition of upland paths (2018).

92. *José Estuardo Jara Alvear*: Solar photovoltaic potential to complement hydropower in Ecuador: A GIS-based framework of analysis (2018).

93. *Brendan O'Neill*: Multicriteria Site Suitability for Algal Biofuel Production Facilities (2018).

94. *Roman Spataru*: Spatial-temporal GIS analysis in public health – a case study of polio disease (2018).

95. *Alicja Miodońska*: Assessing evolution of ice caps in Suðurland, Iceland, in years 1986 - 2014, using multispectral satellite imagery (2019).

96. *Dennis Lindell Schettini*: A Spatial Analysis of Homicide Crime's Distribution and Association with Deprivation in Stockholm Between 2010-2017 (2019).

97. *Damiano Vesentini*: The Po Delta Biosphere Reserve: Management challenges and priorities deriving from anthropogenic pressure and sea level rise (2019).

98. *Emilie Arnesten*: Impacts of future sea level rise and high water on roads, railways and environmental objects: a GIS analysis of the potential effects of increasing sea levels and highest projected high water in Scania, Sweden (2019).

99. *Syed Muhammad Amir Raza*: Comparison of geospatial support in RDF stores: Evaluation for ICOS Carbon Portal metadata (2019).

100. *Hemin Tofiq*: Investigating the accuracy of Digital Elevation Models from UAV images in areas with low contrast: A sandy beach as a case study (2019).

101. *Evangelos Vafeiadis*: Exploring the distribution of accessibility by public transport using spatial analysis. A case study for retail concentrations and public hospitals in Athens (2019).

102. *Milan Sekulic*: Multi-Criteria GIS modelling for optimal alignment of roadway by-passes in the Tlokweng Planning Area, Botswana (2019).

103. *Ingrid Piirisaar*: A multi-criteria GIS analysis for siting of utility-scale photovoltaic solar plants in county Kilkenny, Ireland (2019).

104. *Nigel Fox*: Plant phenology and climate change: possible effect on the onset of various wild plant species' first flowering day in the UK (2019).

105. *Gunnar Hesch*: Linking conflict events and cropland development in Afghanistan, 2001 to 2011, using MODIS land cover data and Uppsala Conflict Data Programme (2019).

106. *Elijah Njoku*: Analysis of spatial-temporal pattern of Land Surface Temperature (LST) due to NDVI and elevation in Ilorin, Nigeria (2019).

107. *Katalin Bunyevácz*: Development of a GIS methodology to evaluate informal urban green areas for inclusion in a community governance program (2019).

108. *Paul dos Santos*: Automating synthetic trip data generation for an agent-based simulation of urban mobility (2019).

109. *Robert O' Dwyer*: Land cover changes in Southern Sweden from the mid-Holocene to present day: Insights for ecosystem service assessments (2019).

110. *Daniel Klingmyr*: Global scale patterns and trends in tropospheric NO2 concentrations (2019).

111. *Marwa Farouk Elkabbany*: Sea Level Rise Vulnerability Assessment for Abu Dhabi, United Arab Emirates (2019).

112. *Jip Jan van Zoonen*: Aspects of Error Quantification and Evaluation in Digital Elevation Models for Glacier Surfaces (2020).

113. *Georgios Efthymiou*: The use of bicycles in a mid-sized city – benefits and obstacles identified using a questionnaire and GIS (2020).

114. *Haruna Olayiwola Jimoh*: Assessment of Urban Sprawl in MOWE/IBAFO Axis of Ogun State using GIS Capabilities (2020).

115. *Nikolaos Barmpas Zachariadis*: Development of an iOS, Augmented Reality for disaster management (2020).

116. *Ida Storm*: ICOS Atmospheric Stations: Spatial Characterization of CO2 Footprint Areas and Evaluating the Uncertainties of Modelled CO2 Concentrations (2020).

117. *Alon Zuta*: Evaluation of water stress mapping methods in vineyards using airborne thermal imaging (2020).

118. *Marcus Eriksson*: Evaluating structural landscape development in the municipality Upplands-Bro, using landscape metrics indices (2020).

119. *Ane Rahbek Vierø*: Connectivity for Cyclists? A Network Analysis of Copenhagen's Bike Lanes (2020).

120. *Cecilia Baggini*: Changes in habitat suitability for three declining Anatidae species in saltmarshes on the Mersey estuary, North-West England (2020).

121. *Bakrad Balabanian*: Transportation and Its Effect on Student Performance (2020).

122. *Ali Al Farid*: Knowledge and Data Driven Approaches for Hydrocarbon Microseepage Characterizations: An Application of Satellite Remote Sensing (2020).

123. *Bartlomiej Kolodziejczyk*: Distribution Modelling of Gene Drive-Modified Mosquitoes and Their Effects on Wild Populations (2020).

124. *Alexis Cazorla*: Decreasing organic nitrogen concentrations in European water bodies - links to organic carbon trends and land cover (2020).

125. *Kharid Mwakoba*: Remote sensing analysis of land cover/use conditions of community-based wildlife conservation areas in Tanzania (2021).

126. *Chinatsu Endo*: Remote Sensing Based Pre-Season Yellow Rust Early Warning in Oromia, Ethiopia (2021).

127. *Berit Mohr*: Using remote sensing and land abandonment as a proxy for long-term human out-migration. A Case Study: Al-Hassakeh Governorate, Syria (2021).

128. *Kanchana Nirmali Bandaranayake*: Considering future precipitation in delineation locations for water storage systems - Case study Sri Lanka (2021).

129. *Emma Bylund*: Dynamics of net primary production and food availability in the aftermath of the 2004 and 2007 desert locust outbreaks in Niger and Yemen (2021).

130. *Shawn Pace*: Urban infrastructure inundation risk from permanent sea-level rise scenarios in London (UK), Bangkok (Thailand) and Mumbai (India): A comparative analysis (2021).

131. *Oskar Evert Johansson*: The hydrodynamic impacts of Estuarine Oyster reefs, and the application of drone technology to this study (2021).

132. *Pritam Kumarsingh*: A Case Study to develop and test GIS/SDSS methods to assess the production capacity of a Cocoa Site in Trinidad and Tobago (2021).

133. *Muhammad Imran Khan*: Property Tax Mapping and Assessment using GIS (2021).

134. *Domna Kanari*: Mining geosocial data from Flickr to explore tourism patterns: The case study of Athens (2021).

135. *Mona Tykesson Klubien*: Livestock-MRSA in Danish pig farms (2021).

136. *Ove Njøten*: Comparing radar satellites. Use of Sentinel-1 leads to an increase in oil spill alerts in Norwegian waters (2021).

137. *Panagiotis Patrinos*: Change of heating fuel consumption patterns produced by the economic crisis in Greece (2021).

138. *Lukasz Langowski*: Assessing the suitability of using Sentinel-1A SAR multi-temporal imagery to detect fallow periods between rice crops (2021).

139. *Jonas Tillman*: Perception accuracy and user acceptance of legend designs for opacity data mapping in GIS (2022).

140. *Gabriela Olekszyk*: ALS (Airborne LIDAR) accuracy: Can potential low data quality of ground points be modelled/detected? Case study of 2016 LIDAR capture over Auckland, New Zealand (2022).

141. *Luke Aspland*: Weights of Evidence Predictive Modelling in Archaeology (2022).

142. *Luís Fareleira Gomes*: The influence of climate, population density, tree species and land cover on fire pattern in mainland Portugal (2022).

143. *Andreas Eriksson*: Mapping Fire Salamander (Salamandra salamandra) Habitat Suitability in Baden-Württemberg with Multi-Temporal Sentinel-1 and Sentinel-2 Imagery (2022).

144. *Lisbet Hougaard Baklid*: Geographical expansion rate of a brown bear population in Fennoscandia and the factors explaining the directional variations (2022).

145. *Victoria Persson*: Mussels in deep water with climate change: Spatial distribution of mussel (Mytilus galloprovincialis) growth offshore in the French Mediterranean with respect to climate change scenario RCP 8.5 Long Term and Integrated Multi-Trophic Aquaculture (IMTA) using Dynamic Energy Budget (DEB) modelling (2022).

146. *Benjamin Bernard Fabien Gérard Borgeais*: Implementing a multi-criteria GIS analysis and predictive modelling to locate Upper Palaeolithic decorated caves in the Périgord noir, France (2022).

147. *Bernat Dorado-Guerrero*: Assessing the impact of post-fire restoration interventions using spectral vegetation indices: A case study in El Bruc, Spain (2022).

148. *Ignatius Gabriel Aloysius Maria Perera*: The Influence of Natural Radon Occurrence on the Severity of the COVID-19 Pandemic in Germany: A Spatial Analysis (2022).

149. *Mark Overton*: An Analysis of Spatially-enabled Mobile Decision Support Systems in a Collaborative Decision-Making Environment (2022).

150. *Viggo Lunde*: Analysing methods for visualizing time-series datasets in open-source web mapping (2022).

151. *Johan Viscarra Hansson*: Distribution Analysis of Impatiens glandulifera in Kronoberg County and a Pest Risk Map for Alvesta Municipality (2022).

152. *Vincenzo Poppiti*: GIS and Tourism: Developing strategies for new touristic flows after the Covid-19 pandemic (2022).

153. *Henrik Hagelin*: Wildfire growth modelling in Sweden - A suitability assessment of available data (2023).

154. *Gabriel Romeo Ferriols Pavico*: Where there is road, there is fire (influence): An exploratory study on the influence of roads in the spatial patterns of Swedish wildfires of 2018 (2023).

155. *Colin Robert Potter*: Using a GIS to enable an economic, land use and energy output comparison between small wind powered turbines and large-scale wind farms: the case of Oslo, Norway (2023).

156. *Krystyna Muszel*: Impact of Sea Surface Temperature and Salinity on Phytoplankton blooms phenology in the North Sea (2023).

157. *Tobias Rydlinge*: Urban tree canopy mapping - an open source deep learning approach (2023).

158. *Albert Wellendorf*: Multi-scale Bark Beetle Predictions Using Machine Learning (2023).

159. *Manolis Papadakis*: Use of Satellite Remote Sensing for Detecting Archaeological Features: An Example from Ancient Corinth, Greece (2023).

160. *Konstantinos Sourlamtas*: Developing a Geographical Information System for a water and sewer network, for monitoring, identification and leak repair - Case study: Municipal Water Company of Naoussa, Greece (2023).

161. *Xiaoming Wang*: Identification of restoration hotspots in landscape-scale green infrastructure planning based on model-predicted connectivity forest (2023).

162. *Sarah Sienaert*: Usability of Sentinel-1 C-band VV and VH SAR data for the detection of flooded oil palm (2023).

163. *Katarina Ekeroot*: Uncovering the spatial relationships between Covid-19 vaccine coverage and local politics in Sweden (2023).

164. *Nikolaos Kouskoulis*: Exploring patterns in risk factors for bark beetle attack during outbreaks triggered by drought stress with harvester data on attacked trees: A case study in Southeastern Sweden (2023).

165. *Jonas Almén*: Geographic polarization and clustering of partisan voting: A local-level analysis of Stockholm Municipality (2023).

166. *Sara Sharon Jones*: Tree species impact on Forest Fire Spread Susceptibility in Sweden (2023).

167. *Takura Matswetu*: Towards a Geographic Information Systems and Data-Driven Integration Management. Studying holistic integration through spatial accessibility of services in Tampere, Finland. (2023).

168. *Duncan Jones*: Investigating the influence of the tidal regime on harbour porpoise *Phocoena phocoena* distribution in Mount's Bay, Cornwall (2023).

169. *Jason Craig Joubert*: A comparison of remote sensed semi-arid grassland vegetation anomalies detected using MODIS and Sentinel-3, with anomalies in ground-based eddy covariance flux measurements (2023).

170. *Anastasia Sarelli*: Land cover classification using machine-learning techniques applied to fused multi-modal satellite imagery and time series data (2024).

171. *Athanasios Senteles*: Integrating Local Knowledge into the Spatial Analysis of Wind Power: The case study of Northern Tzoumerka, Greece (2024).

172. *Rebecca Borg:* Using GIS and satellite data to assess access of green area for children living in growing cities (2024).

173. *Panagiotis–Dimitrios Tsachageas*: Multicriteria Evaluation in Real Estate Land-use Suitability Analysis: The case of Volos, Greece (2024).

174. *Hugo Nilsson*: Inferring lane-level topology of signalised intersections from aerial imagery and OpenStreetMap using deep learning (2024).

175. *Pavlos Alexantonakis*: Estimating lake water volume fluctuations using Sentinel-2 and ICESat-2 remote sensing data (2024).

176. *Karl-Martin Wigen*: Physical barriers and where to find them (2024).

177. *Martin Storsnes*: Temporal RX-algorithm performance on Sentinel-2 images (2024).

178. *Saulė Gabrielė Petraitytė*: The Relation Between Covid-19 Vaccination and Voting Trends in Lithuania: A Spatial Analysis (2024).

179. *Pedro Martinez Duran*: Olive yield forecasting from remote sensing and climate datasets in the Jaen province (Spain) (2024).

180. *Josefine Kynde Hämberg*: Proximity to Urban Green Spaces for Older Adults in Specific Housings - a Case Study of Malmö, Sweden (2024).

181. *Max Bengtsson*: A Site Selection of An Energy Island in the North Sea: Optimal Location in an Ecological and an Economic Scenario Using a Multicriteria Decision Analysis (MCDA) (2024).

182. *Anna Börmann*: Assessing Great Britain as a relocation site for the threatened Iberian Lynx in a changing climate (2024).

183. *Josephine Roosli*: Flood Risk Assessment for the Kävlinge River for Present and Future Climate Scenarios using HEC-RAS Rain-on-Grid (2024).